



RESEARCH ARTICLE

10.1029/2021MS002648

Key Points:

- Process-based tracers in iCAM6 allow for expanded hypothesis testing of water cycle change and more informed use of water isotope ratios
- The degree of parcel rainout is a primary control on both $\delta^{18}\text{O}$ and d-excess, consistent with Rayleigh theory
- Water vapor residence time does not strongly influence precipitation $\delta^{18}\text{O}$, but evaporative conditions influence precipitation d-excess

Supporting Information:

Supporting Information may be found in the online version of this article.

Correspondence to:

R. P. Fiorella,
rich.fiorella@utah.edu

Citation:

Fiorella, R. P., Siler, N., Nusbaumer, J., & Noone, D. C. (2021). Enhancing understanding of the hydrological cycle via pairing of process-oriented and isotope ratio tracers. *Journal of Advances in Modeling Earth Systems*, 13, e2021MS002648. <https://doi.org/10.1029/2021MS002648>

Received 2 JUN 2021

Accepted 9 SEP 2021

Enhancing Understanding of the Hydrological Cycle via Pairing of Process-Oriented and Isotope Ratio Tracers

Richard P. Fiorella^{1,2} , Nicholas Siler³ , Jesse Nusbaumer⁴ , and David C. Noone⁵ 

¹Department of Geology and Geophysics, University of Utah, Salt Lake City, UT, USA, ²Global Change and Sustainability Center, University of Utah, Salt Lake City, UT, USA, ³College of Earth, Ocean, and Atmospheric Sciences, Oregon State University, Corvallis, OR, USA, ⁴Climate and Global Dynamics Laboratory, National Center for Atmospheric Research, Boulder, CO, USA, ⁵Department of Physics, University of Auckland, Auckland, New Zealand

Abstract The hydrologic cycle couples the Earth's energy and carbon budgets through evaporation, moisture transport, and precipitation. Despite a wealth of observations and models, fundamental limitations remain in our capacity to deduce even the most basic properties of the hydrological cycle, including the spatial pattern of the residence time (RT) of water in the atmosphere and the mean distance traveled from evaporation sources to precipitation sinks. Meanwhile, geochemical tracers such as stable water isotope ratios provide a tool to probe hydrological processes, yet their interpretation remains equivocal despite several decades of use. As a result, there is a need for new mechanistic tools that link variations in water isotope ratios to underlying hydrological processes. Here we present a new suite of "process-oriented tags," which we use to explicitly trace hydrological processes within the isotopically enabled Community Atmosphere Model, version 6 (iCAM6). Using these tags, we test the hypotheses that precipitation isotope ratios respond to parcel rainout, variations in atmospheric RT, and preserve information regarding meteorological conditions during evaporation. We present results for a historical simulation from 1980 to 2004, forced with winds from the ERA5 reanalysis. We find strong evidence that precipitation isotope ratios record information about atmospheric rainout and meteorological conditions during evaporation, but little evidence that precipitation isotope ratios vary with water vapor RT. These new tracer methods will enable more robust linkages between observations of isotope ratios in the modern hydrologic cycle or proxies of past terrestrial environments and the environmental processes underlying these observations.

Plain Language Summary The heavy-to-light isotope ratio of atmospheric water, which records a wide array of water cycle processes, is readily observable and has therefore long been thought to hold much promise to help examine changes in water cycle processes. However, as multiple processes influence water isotope ratios, it is often difficult to tie observations to hydrological processes without using an atmospheric model. In this work, we develop a comprehensive set of numerical tracers to elucidate water cycle processes in the atmosphere from source to sink. In the context of water isotope ratios, these numerical tracers provide a method to explicitly test hypotheses of how variations in water isotope ratios map to underlying hydrological processes. The new tracers we outline here permit a fuller understanding of the hydrologic cycle and allow new ways to test model parameterizations and understand the processes governing hydrologic change.

1. Introduction

The hydrologic cycle couples Earth's energy and carbon budgets through evaporation, precipitation, and water resource availability for ecosystems (e.g., Humphrey et al., 2018). Globally, evaporation consumes up to ~50% of shortwave radiation reaching the Earth's surface (L'Ecuyer et al., 2015; Trenberth et al., 2009). In the atmosphere, water vapor plays a significant role in planetary energy balance by absorbing and reemitting longwave radiation (Held & Soden, 2000, 2006; Raval & Ramanathan, 1989), and transporting energy upward or poleward to regions of lower temperature (Hwang & Frierson, 2010; Kleidon & Renner, 2013; Konings et al., 2012; Pauluis, 2011; Siler et al., 2018). Yet, substantial uncertainties about how water moves through the atmosphere limit our ability to diagnose water cycle variations and their relationship to climate change (Aron et al., 2019; Bowen et al., 2019; Good et al., 2015; Martens et al., 2017; Wang-Erlandsson et al., 2014; Wei et al., 2017).

Stable water isotope ratios are widely invoked as geochemical tracers of the hydrologic cycle. Phase changes partition water isotopologues unequally: heavier isotopologues disproportionately enter or remain in the liquid or solid phases while lighter isotopologues preferentially enter or remain in the vapor phase due to differences in the saturation vapor pressure and molecular diffusivity of isotopologues (Bigeleisen, 1965; Bigeleisen & Wolfsberg, 1958; Dansgaard, 1964; Gat, 1996). As a result, water isotope ratios have been widely used to make inferences about the temperature and transport histories of the water vapor from which precipitation forms. Unfortunately, the integrative nature of these geochemical tracers also places limits on how well we can map observed isotope ratios to specific hydrological processes.

As observations of water isotope ratios have proliferated, so too have theories to explain their variation in space and time. Early interpretations relied on Rayleigh distillation, where variations in isotope ratios were explained primarily by changes in temperature or the fraction of moisture lost along a parcel's trajectory. While early studies in the paleoclimate context recognized the likely limitations of the Rayleigh distillation model in its simplest form (e.g., Dansgaard, 1964; Eriksson, 1965; Jouzel et al., 1997; Merlivat & Jouzel, 1979; Siegenthaler & Oeschger, 1980), more recent interpretations of precipitation isotope ratios have sought to understand the full range of processes influencing water isotope ratios. For example, recent studies have established relationships between isotope ratios and atmospheric residence time (RT) (Aggarwal et al., 2012), cloud type and/or microphysics (Aggarwal et al., 2016; Konecky et al., 2019; Zwart et al., 2018), upwind precipitation variations (Cai & Tian, 2016; Dayem et al., 2010; Fiorella, Poulsen, Pillco Zolá, Barnes, et al., 2015; Vimeux et al., 2011), zonal-mean patterns of precipitation, evaporation, and vapor transport (Bailey et al., 2018; Siler et al., 2021), variations in moisture sources (e.g., Jouzel et al., 1997; Putman et al., 2017; Sodemann et al., 2008; Tian et al., 2001; Vuille et al., 2003), and variations in the large-scale vertical velocity (Blossey et al., 2010; Moore et al., 2014). Moreover, the increased number of mechanisms invoked to explain isotopic variability contrasts with the comparatively simple physics responsible for isotopic fractionation. Rigorous testing of these hypotheses requires novel methods that can account for multiple processes simultaneously while revealing the integrated history of water parcels.

Most prior implementations of numerical water tracers or “tags” have focused on examining the relative importance of moisture sources to a particular location (e.g., Dominguez et al., 2016; Dyer et al., 2017; Gimeno et al., 2010; Knoche & Kunstmann, 2013; Koster et al., 1986; Nieto et al., 2006; Noone & Simmonds, 2002; Nusbaumer & Noone, 2018; Singh, Bitz, Donohoe, et al., 2016; Singh, Bitz, Nusbaumer, & Noone, 2016; Sodemann & Stohl, 2009; Wei et al., 2017; Winschall et al., 2014). While powerful, this technique is computationally expensive, and its results are highly dependent on how source regions are defined.

A complementary approach is to tag specific processes or quantities within the model rather than specific regions. For example, Risi et al. (2013) used such a process-tagging approach to identify contributions to water mass balance within convective regions. Here, we use the same approach to tag a much more comprehensive range of variables within the isotope-enabled version of the National Center for Atmospheric Research (NCAR) Community Atmosphere Model, version 6 (iCAM6). Process-oriented tags provide additional context and support for interpreting the water cycle and improving the linkage between hydrologic processes and modeled or observed water isotope ratios. Consequently, the expansion of water tagging capabilities offers a new frontier for testing hypotheses on controls on water isotope ratios. Utilizing these tags, we demonstrate that (a) spatial and temporal deviations in precipitation isotope ratios from values predicted by Rayleigh distillation (Dansgaard, 1964; Gat, 1996; Rozanski et al., 1993) are primarily related to variations in the initial isotope ratio of a parcel; (b) precipitation isotope ratios poorly reflect variations in the RT of atmospheric water vapor, in contrast to the hypothesis of Aggarwal et al. (2012); and (c) the deuterium excess of precipitation (d-excess or $d = \delta^2\text{H} - \delta^{18}\text{O}$) primarily varies in response to rainout effects and the relative humidity during evaporation, rather than evaporation temperature or wind speed (Johnsen et al., 1989; Jouzel et al., 1982; Jouzel, Lorius, et al., 1987; Pfahl & Sodemann, 2014; Vimeux et al., 1999).

2. Theory

We introduce general “process-oriented tags” designed to track properties associated with evaporation, transport, and condensation using numerical tracers. The mass of water vapor within a volume (such as a model grid cell) arises from the sum of the contributions from many air parcels:

$$q(t, p, \lambda, \phi) = \sum_{i=1}^{\infty} \gamma_i(t, p, \lambda, \phi) q_i(t, p, \lambda, \phi) \quad (1)$$

where t , p , λ , and ϕ refer to time, pressure, latitude, and longitude respectively, q_i refers to the specific humidity of parcel i , and γ_i is the fractional contribution of each parcel to the total humidity $q(t, p, \lambda, \phi)$. Across all contributing parcels, γ_i sums to 1. This summation over all contributing parcels facilitates a diagnostic approach that provides an alternate perspective to the integrated Eulerian mass balance equation for a grid cell at a particular location:

$$q(t, p, \lambda, \phi) = \int_0^\tau [e(t, p, \lambda, \phi) - c(t, p, \lambda, \phi) - (\bar{U} \cdot \nabla) q(t, p, \lambda, \phi)] d\tau \quad (2)$$

where e and c are the local evaporation and condensation rates within the grid cell, and $-(\bar{U} \cdot \nabla) q(t, p, \lambda, \phi)$ represents the moisture advection into the grid cell, t is the current time, and τ is the length of time that water vapor in the parcel has been in the atmosphere. Considering the summation over individual parcels provides a succinct representation of moisture sources and sinks along the (Lagrangian) transport path before their arrival to the grid cell. Within an Eulerian model, like CAM, the advective and subgrid-scale transport effectively produces the mixture of parcels captured by the operator γ , and its numerical value can be diagnosed with a tracer diagnostic approach (e.g., water fractions highlighted in tagging studies noted above). Along the transport path, sources and sinks may be local (within the grid cell) or occur upstream and transported to the grid cell under consideration. The integral of upstream sources and sinks is required to recover contributions from moisture sources and sinks outside of the current grid cell.

Each parcel i has a distinct history of moisture sources (e.g., evaporation) and sinks (e.g., condensation), such that:

$$\frac{dq_i(t, p, \lambda, \phi)}{dt} = e_i(t, p, \lambda, \phi) - c_i(t, p, \lambda, \phi) \quad (3)$$

where dq_i/dt is the rate of humidity change along a parcel, e_i is the evaporation rate into the parcel, and c_i is the condensation rate out of the parcel. In the CAM code, we specify that the traced quantity has zero mass in the atmosphere when the simulation is initiated. Integrating across the parcel trajectory yields an analytic expression for $q_i(t, p, \lambda, \phi)$:

$$q_i(t, p, \lambda, \phi) = \int_0^{\tau_i} (e_i(\tau) - c_i(\tau)) d\tau \quad (4)$$

(It is useful to note that the integration is parametric and could take place with respect to “length” along the trajectory instead of time). Assuming the parcel enters the atmosphere at time t_o , t and τ_i are related through the expression $\tau_i = t - t_o$.

Analogous equations can describe an arbitrary water tracer quantity identified with index j , q_j , that is comprised of the same i parcels:

$$q_j(t, p, \lambda, \phi) = \sum_{i=1}^{\infty} \gamma_i(t, p, \lambda, \phi) q_{ij}(t, p, \lambda, \phi) \quad (5)$$

where q_{ij} is represented by:

$$q_{ij}(t, p, \lambda, \phi) = \int_0^{\tau_i} (e_{ij}(\tau) - c_{ij}(\tau)) d\tau \quad (6)$$

We can formulate tracers tracking properties of geophysical interest—such as evaporation or condensation temperature, moisture source locations, or the RT of water in the atmosphere—over a parcel’s lifetime through careful selection of how e_{ij} and c_{ij} are defined (Table 1). Each tagged quantity represents another passive representation of the hydrological cycle with a modified version of the model’s “bulk” evaporation or condensation flux or a sum of a quantity of interest through time (Table 1). The tagged quantity is passive and does not influence model transport and physics (e.g., convection, radiation, etc.) of “bulk” water vapor in any way, but experience the same sources, sinks, and atmospheric transport as “bulk” water vapor proportionally. Proportionality is maintained through the tracer ratio, R :

$$R_j = \frac{q_j}{q} = \frac{\sum_{i=1}^{\infty} \gamma_i \int_0^{\tau_i} (e_{ij} - c_{ij}) d\tau}{\sum_{i=1}^{\infty} \gamma_i \int_0^{\tau_i} (e_i - c_i) d\tau} \quad (7)$$

Table 1

Specification of Tracer Evaporation or Condensation Rates Relative to Bulk Rates

Tracer type	Tracer representation of evaporation for each parcel, e_i	Tracer representation of condensation for each parcel, c_i
Evaporation (Section 2.1)	$e_{ij}(t, \lambda, \phi) = X_j(t_i, \lambda_i, \phi_i)e_i(t_i, \lambda_i, \phi_i)$	$c_{ij} = R_i(t, p, \lambda, \phi)c_i(t, p, \lambda, \phi)$
Integrated quantities (Section 2.2)	$e_{ij} = q_{ij}(t_i, \lambda_i, \phi_i)$ or $e_{ij} = X_j(t_i, \lambda_i, \phi_i)q_i(t_i, \lambda_i, \phi_i)$	$c_{ij} = R_i(t, p, \lambda, \phi)c_i(t, p, \lambda, \phi)$
Condensation (Section 2.3)	$e_{ij} = 0$	$c_{ij} = X_j(t, p, \lambda, \phi)c_i(t, p, \lambda, \phi)$
Water isotope ratios (Section 2.4)	$e_{ij}(t, \lambda, \phi) = [R_{Li}(t_i, \lambda_i, \phi_i) / \alpha_{evap}]e(t_i, \lambda_i, \phi_i)$	$c_{ij} = \alpha_{cond}R_i(t, p, \lambda, \phi)c_i(t, p, \lambda, \phi)$

Note. The subscript i indicates the conditions at the moisture origin, which may be outside the current grid cell and at different times.

The tracer ratio R in Equation 7 is calculated for vapor in the atmosphere ($R_j = q_j/q$), with similar ratios for the evaporative flux ($R_{j,e} = e_j/e$), or for condensate ($R_{j,c} = c_j/c$). For the tracer scheme, it is assumed that the conversion of condensate to precipitation within a grid cell conserves the tracer ratio, as the convection and cloud physics parameterizations in iCAM6 maintain R in the condensate and precipitation (P) by requiring that $R_{j,c} = c/c = P/P = R_{j,p}$. Likewise, it is assumed that R is preserved during subcloud evaporation of hydrometeors in the tracer code, with the exception of isotopic tracers (Section 2.4). Therefore, the quantity of interest can be recovered in atmospheric vapor or precipitation using the definition of the tracer ratio, R_j (Equation 7), both at any instant or as a time- and mass-weighted average (e.g., daily or monthly values). We briefly describe some important characteristics and details of each of the tracer classes implemented in iCAM6 below.

2.1. Evaporation Source Property Tracers

A tracer is developed such a property of the evaporation source, X , can be recovered from the model integration as:

$$X_j = \frac{q_{Ej}}{q} \quad (8)$$

The subscript E denotes an evaporation type tracer. This is accomplished by scaling the evaporation flux by the property of interest: $e_{ji} = Xe_i$, such that the tracer takes the integrated form:

$$q_{Ej}(t, p, \lambda, \phi) = \sum_{i=1}^{\infty} \gamma_i \int_0^{\tau_i} [X_j(t_i, p_i, \lambda_i, \phi_i)e_i(t_i, p_i, \lambda_i, \phi_i) - R(t, p, \lambda, \phi)c_i(t, p, \lambda, \phi)] d\tau \quad (9)$$

$X_j(t_p p_i \lambda_i \phi_i)$ represents the property being traced and acts to weight the evaporation flux. Condensation does not change the value of this source property, and therefore the tracer condensation rate is multiplied by R to maintain the tracer ratio in the condensate and the remaining vapor. The subscript i indicates that these properties are inherited from each parcel and may originate from other locations and at earlier times. In principle, e_i can reflect any source of humidity to the atmosphere (e.g., evaporation of condensate), though in this work, we assume e_i to represent evaporation from the land or ocean surface, which removes the pressure dimension of X_j and e_i . Several prior studies have used this general approach to determine the relative importance of moisture sources to a region (e.g., Hu & Dominguez, 2015; Kelley, 2003; Knoche & Kunstmann, 2013; Lewis et al., 2013; Nusbaumer et al., 2019; Nusbaumer & Noone, 2018; Singh, Bitz, Donohoe, et al., 2016; Singh, Bitz, Nusbaumer, & Noone, 2016). The weight $X_j(t_p \lambda_i \phi_i)$ might be defined as 1 if within the region of interest and 0 otherwise. This powerful technique differentiates between candidate moisture source regions, but the regions of interest must be pre-defined. More generally, $X_j(t_p \lambda_i \phi_i)$ can represent any quantity related to the evaporation flux. For instance, $X_j(t_p \lambda_i \phi_i)$ can represent the surface temperature, relative humidity, wind speed, or location (e.g., latitude, longitude, elevation) associated with evaporation. The use of location immediately produces a method to determine the mass-weighted mean origin of water for any location and avoids the need to have numerous tag regions.

2.2. Tracing Integrated or Mean Parcel Properties

One may wish to track the mean property of a parcel along the moisture transport path. For example, we may wish to know how long moisture spends in the atmosphere, how far it travels, or the mean wind speed encountered between source and sink. To recover these quantities, we define an additional tracer type that integrates grid-cell humidity over time:

$$Q(t, p, \lambda, \phi) = \sum_{i=1}^{\infty} \gamma_i \int_0^{\tau_i} [q_i(t, p, \lambda, \phi) - R_i(t, p, \lambda, \phi)c_i(t, p, \lambda, \phi)] d\tau \quad (10)$$

where q_i is defined by Equation 4. $Q(t, p, \lambda, \phi)$ can be used to determine how long vapor has been in a grid cell by dividing it by the mean value of q during the interval τ_i and using the mean value theorem of integrals:

$$R' = \frac{Q(p, \lambda, \phi)}{q(p, \lambda, \phi)} = \frac{\sum_{i=1}^{\infty} \gamma_i \int_0^{\tau_i} [q_i(t, p, \lambda, \phi) - R_i(t, p, \lambda, \phi)c_i(t, p, \lambda, \phi)] d\tau}{\sum_{i=1}^{\infty} \frac{\gamma_i}{\tau_i} \int_0^{\tau_i} [q_i(t, p, \lambda, \phi) - R_i(t, p, \lambda, \phi)c_i(t, p, \lambda, \phi)] d\tau} = \bar{\tau} \quad (11)$$

This formulation provides a simple method to deduce the age of water vapor in the atmosphere. While this expression itself appears simple, the integral along the parcel is completed as part of the model transport scheme, and therefore the numerator and denominator are only available in their integrated form (as in Equations 1 and 5). The power of this approach is seen by considering the extension in which one may utilize $Q(t, p, \lambda, \phi)$ to calculate a transport-path-integrated mean property for the parcel once paired with another integrated tracer $Q_j(t, p, \lambda, \phi)$:

$$Q_j(t, p, \lambda, \phi) = \sum_{i=1}^{\infty} \gamma_i \int_0^{\tau_i} q_{ij}(t, p, \lambda, \phi) d\tau = \sum_{i=1}^{\infty} \gamma_i \int_0^{\tau_i} [X_j(t, p, \lambda, \phi)q_i(t, p, \lambda, \phi) - R_i(t, p, \lambda, \phi)c_i(t, p, \lambda, \phi)] d\tau \quad (12)$$

The tracer ratio $R'' = Q_j/Q$ now allows recovery of the mass-weighted mean value of $X(t, p, \lambda, \phi)$ integrated across the parcel:

$$R'' = \frac{Q_j(t, p, \lambda, \phi)}{Q(t, p, \lambda, \phi)} = \frac{\sum_{i=1}^{\infty} \gamma_i \int_0^{\tau_i} [X_j(t, p, \lambda, \phi)q_i(t, p, \lambda, \phi) - R_i(t, p, \lambda, \phi)c_i(t, p, \lambda, \phi)] d\tau}{\sum_{i=1}^{\infty} \gamma_i \int_0^{\tau_i} [q_i(t, p, \lambda, \phi) - R_i(t, p, \lambda, \phi)c_i(t, p, \lambda, \phi)] d\tau} = \overline{X(t, p, \lambda, \phi)} \quad (13)$$

If $X(t, p, \lambda, \phi)$ happens to be a rate (e.g., such as a wind speed), the tracer ratio can be redefined to give the time-integrated value of $X(t, p, \lambda, \phi)$ (e.g., a distance):

$$R''' = \frac{Q_j(t, p, \lambda, \phi)}{q(t, p, \lambda, \phi)} = \frac{\sum_{i=1}^{\infty} \gamma_i \int_0^{\tau_i} [X_j(t, p, \lambda, \phi)q_i(t, p, \lambda, \phi) - R_i(t, p, \lambda, \phi)c_i(t, p, \lambda, \phi)] d\tau}{\sum_{i=1}^{\infty} \frac{\gamma_i}{\tau_i} \int_0^{\tau_i} [q_i(t, p, \lambda, \phi) - R_i(t, p, \lambda, \phi)c_i(t, p, \lambda, \phi)] d\tau} = \overline{X(t, p, \lambda, \phi)} \bar{\tau} \quad (14)$$

In all cases, the tracer ratio can be calculated using 2D precipitation fields in addition to the 3D humidity fields.

2.3. Local Condensation Diagnostics

Properties of condensate formation are recovered by weighting the condensation flux. A condensation tracer could be constructed where q_j is zero, but $c_j = X_j(t, p, \lambda, \phi)c(t, p, \lambda, \phi)$, where c refers to the bulk condensation flux, and X_j refers to the property we wish to trace (e.g., condensation temperature, pressure, or height). After the model has converted condensate to precipitation, the mass-weighted average value of X_j is recovered as $\overline{X}_j = R = P_j/P$.

Phase changes between vapor, cloud liquid, and cloud ice are complex in modern microphysical schemes, and it is often more straightforward to define q_j immediately before condensate formulation within a model's physics parameterizations. Moreover, this approach removes the possibility of missing one or more conversions between vapor and cloud liquid or ice. Therefore, to implement condensation property tracers in CAM, we define a tracer at each time step as:

$$q_{Cj}(t, p, \lambda, \phi) = X_j(t, p, \lambda, \phi)q_j(t, p, \lambda, \phi) \quad (15)$$

The subscript C denotes a condensation-type tag. As the tracer is re-defined at each step, there is no memory of prior times in the vapor tracer quantity, but the tracer accumulates in condensate and precipitation over time. As a result, the mass-weighted vertical average of X remains $\overline{X} = R = P_j/P$.

2.4. Tracing Water Isotope Ratios

Tracers of water isotope ratios differ from evaporation source tracers in that phase changes do not preserve the tracer ratio R but rather should unequally partition the tracer mass in response to isotopic fractionation effects. For example, fractionation during evaporation or condensation may be described by comparing the heavy-to-light isotope ratios in water between the phases:

$$\alpha = \frac{R_L}{R_v} = \frac{(q_j/q)_L}{(q_j/q)_v} \quad (16)$$

where α is the fractionation factor, R denotes the heavy-to-light isotope ratio, and subscripts L and v refer to the liquid and vapor phases, respectively. Within iCAM6, fractionation schemes include (a) treatment of evaporation from the land or ocean surface to the atmosphere; (b) accounting for the partial removal, entrainment, detrainment, and mixed-phase physics and resolved diffusion within the moist physics; and (c) evaporation and re-exchange of water in a falling raindrop through the sub-cloud environment. These processes can change water isotope ratios and, therefore, the “tracer” proportion. Net isotopic fractionations reflect a balance of equilibrium and kinetic isotope effects in each case. Implementation of fractionation within iCAM6 is discussed briefly below, while a more comprehensive description that focuses on iCAM5 is given in Nusbaumer et al. (2017).

3. Methods

3.1. Simulation Setup

We present results from a historical simulation using the CESM2 (Danabasoglu et al., 2020) spanning 1980–2004. We used the finite-volume dynamical core within the atmosphere with a grid that had a horizontal resolution of 0.9° latitude $\times 1.25^\circ$ longitude and 30 vertical hybrid layers from the surface to ~ 3 hPa. Sea-surface temperatures, sea-ice distributions, aerosol distributions, and atmospheric CO_2 concentrations were prescribed based on historical values. The fluxes to the atmosphere from land were calculated by CLM5 (Lawrence et al., 2019). The simulation was “nudged” toward ERA5 reanalysis horizontal winds and surface pressure (Hersbach et al., 2020) using the physics nudging scheme within the model. Model nudging adds a tendency, F_{nudge} , to the zonal and meridional wind and surface pressure fields during each physics timestep that “pulls” iCAM6 toward the atmospheric state in ERA5:

$$F_{\text{nudge}} = \frac{S_{\text{ERA5}} - S_{\text{iCAM6}}}{\Delta t_{\text{nudge}}} \quad (17)$$

where S is the U , V , or surface pressure state in ERA5 and iCAM6, respectively, and Δt_{nudge} is the difference in time between the next ERA5 target state and the current iCAM6 model time. Target ERA5 states are updated every 6 hr (at 00, 06, 12, and 18 UTC), and Δt_{nudge} decreases as the iCAM6 model time approaches the next ERA5 target state. When evaluating the performance of iCAM6 to simulate water isotope ratios, we also include results from an equivalent simulation without the nudging tendencies, allowing the atmospheric state to evolve more “freely.”

Each class of process tags described in Section 2 was implemented in the iCAM6 (Bogenschutz et al., 2018). This branch of iCAM6 includes code to simulate water isotope ratios throughout the atmosphere, and the implementation of isotope tracers is nearly identical to that in iCAM5 (Nusbaumer et al., 2017). The most significant updates are to implement water tracers in the Cloud Layers Unified by Binormals scheme, CLUBB (Bogenschutz et al., 2012), which replaces the boundary layer turbulence, shallow convection, and cloud macrophysics parameterizations used in iCAM5. The additional atmospheric tracers included in this simulation represent a substantial computational cost. For example, tracers for water isotopologues in iCAM6 increase the cost of running CAM6 by $\sim 60\%$ in our setup (~ 2750 core hours/model year compared to 1734 core hours/model year). Each additional traced quantity adds an additional ~ 400 core hours/model year. We have added 59 additional tracers to iCAM6, of which we show a subset in this study, which raises the computational cost of the model to $\sim 26,000$ core hours/model year, nearly 15x more expensive than CAM6 with no isotopic or process-based tracers. Therefore, the added insight available from process-oriented and isotopic tracers needs to be weighed against the added expense.

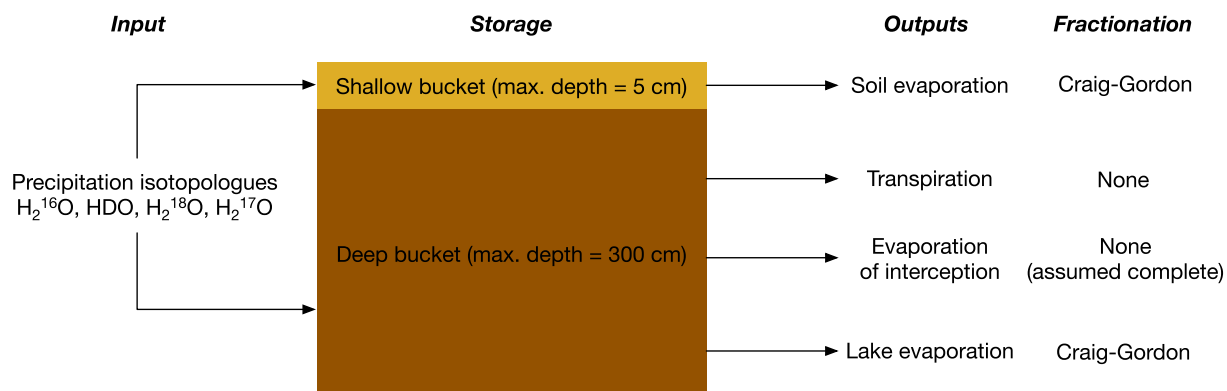


Figure 1. Schematic representation of the land surface bucket model added to iCAM6 to provide isotopic fluxes.

Not all CESM2 component models simulate water tracers, unlike iCESM1 (e.g., Brady et al., 2019). CESM2 currently has water isotope tracers in only the iCAM6 and iCICE5 sub-models. Therefore, we construct a simple bucket model within iCAM6 to simulate isotopic fluxes from the land surface to the atmosphere (Figure 1). The bucket has two layers: a shallow upper layer that captures the rapid changes following precipitation events and a thicker, deeper layer representing gradual changes due to seasonal shifts in precipitation isotope ratios, temperature, and the magnitude of the evaporative flux over land. Bucket models were used extensively in early general circulation models (e.g., Manabe et al., 1965) before the development of more definitive treatments of land surface processes (e.g., Sellers et al., 1997). Implementation of isotope tracers into GCMs have frequently used bucket models with success for simulation of large-scale processes to simplify the calculation of land-to-atmosphere evaporative fluxes (e.g., Hoffmann et al., 1998; Joussaume et al., 1984; Jouzel, Russell, et al., 1987; Lee et al., 2007; Noone & Simmonds, 2002; Risi et al., 2010; Schmidt et al., 2007; Yoshimura et al., 2008). Incorporation of isotope ratios into more complex land surface models permits more detailed study and evaluation of water transport through the land surface and its exchange with the atmosphere (e.g., Haese et al., 2013; Risi et al., 2016; Wong et al., 2017; Yoshimura et al., 2006). Further details of the bucket scheme are given in Appendix A.

3.2. Implementation of Selected Process-Based Tags

We demonstrate each class of process-based tags to test several hypotheses proffered to explain variations in precipitation isotope ratios. Process-oriented tags tracing evaporation properties (Section 2.1) or condensation properties (Section 2.3) are the most straightforward to implement. For condensation property tags, we show the condensation temperature of precipitation. For convective precipitation, we use the updraft temperature at each vertical level where condensation occurs, while we use the grid-layer midpoint temperature for large-scale precipitation. For evaporation property tags, we show tracers of the surface temperature, the relative humidity with respect to the skin temperature of the lowest model level, and the 10-m wind speed during evaporation. In demonstrating recovery of parcel integrated quantities (Section 2.2), we present tags that track the RT and transport distance of atmospheric moisture.

Finally, we track the effective fraction of moisture removed from an air parcel using an additional tracer where isotopic fractionation is constant. Specifically, the rainout is isolated by considering a Rayleigh distillation equation:

$$d \ln R = (\alpha - 1) d \ln q \quad (18)$$

An additional water isotope tracer species (Section 2.3) with constant α (e.g., $\alpha = 1.01$) allows integration of Equation 18 to yield:

$$R = R_0 \left(\frac{q}{q_0} \right)^{\alpha-1} = R_0 f^{\alpha-1} \quad (19)$$

where R is the heavy-to-light isotope ratio, q is the parcel humidity, and a subscript 0 indicates a parcel's initial condition (e.g., the parcel properties immediately after evaporation). The fraction of vapor remaining relative to the parcel's initial entry into the atmosphere can be calculated as $f = q/q_0$. Solving for $\ln(f)$ yields the following expression:

$$\ln f = \ln \frac{q}{q_0} = (\alpha - 1)^{-1} \ln \frac{R}{R_0} = (\alpha - 1)^{-1} \ln \frac{\delta + 1}{\delta_0 + 1} \quad (20)$$

where δ represents a deviation from a standard R ($\delta = R/R_{\text{std}} - 1$, where R_{std} is the heavy-to-light isotope ratio of a standard reference material). Variations in δ or R are small, and therefore, δ values are often expressed as permil (denoted by ‰) deviations from R_{std} . For the “constant α ” tracer described here, δ_0 values for vapor and precipitation are determined relative to fractionation from the land or ocean surface, where the evaporating liquid is set to have $\delta = 0\text{‰}$ for the “constant alpha” tag. With a fixed $\alpha = 1.01$, the initial vapor would have a $\delta = -9.9\text{‰}$, and the first condensate subsequently from this parcel would have a $\delta = 0\text{‰}$. Defined as a tracer in iCAM6, f or $\ln(f)$ reflects the contributions from many parcels with different origin locations and times, and therefore reflects the contributions of upwind atmospheric mixing (Equation 6).

The logarithmic quantities appearing in Equations 18 and 20 arise naturally in Rayleigh-type processes and have become increasingly common in the triple oxygen isotope literature as an alternate definition of δ , often noted as δ' (Aron et al., 2020; Li et al., 2015; Luz & Barkan, 2010; Miller, 2002). As δ can be considered mathematically as the first-order Taylor series expansion of $\ln(\delta + 1)$ (e.g., Noone, 2012), δ and δ' are nearly equivalent for small δ (e.g., Miller, 2002). We can assess how strongly modeled $\delta^{18}\text{O}$ values relate to the Rayleigh rainout effect by comparing $\delta^{18}\text{O}$ and $\ln(f)$: the former of these quantities calculated using the full isotopic physics in iCAM6, and the latter calculated from the constant-fractionation isotope tracer we have added. Deviations from this relationship in the full-physics $\delta^{18}\text{O}$ may arise from variations in $\delta^{18}\text{O}_0$ or the sensitivity of α to temperature and/or supersaturation. In the following analysis, we remove the deviations arising from variations in $\delta^{18}\text{O}_0$ by calculating $\delta^{18}\text{O}$ as an isotopic discrimination from $\delta^{18}\text{O}_0$, as is commonly done for plant waters (e.g., Barbour et al., 2004; Cernusak et al., 2016; Farquhar et al., 2007; Kannenberg et al., 2021):

$$\Delta^{18}\text{O} = \frac{R}{R_0} - 1 = \frac{\delta^{18}\text{O} - \delta^{18}\text{O}_0}{1 + \delta^{18}\text{O}_0} \quad (21)$$

$\delta^{18}\text{O}_0$ is constrained by using an additional tracer that preserves the $\delta^{18}\text{O}$ of the evaporative flux into the atmosphere.

3.3. Data Analyses

Global relationships between tagged quantities and isotope ratios are determined using weighted linear regression, where the weights are grid-cell areas. We compiled observations to compare with modeled values by augmenting the Global Network of Isotopes in Precipitation (GNIP, IAEA/WMO, 2021) with additional studies conducted in regions poorly represented within the GNIP database (Table 2). Non-GNIP data were obtained from original publications or the waterisotopesDB (Putman & Bowen, 2019) (Table 2). Sites were included if observations spanned at least one year. However, this approach may overestimate the “true” difference between observations and the model due to the short duration of some of the observational records (Putman et al., 2019). Moreover, since the model simulation presented here ends in 2004, the model simulation may not reflect potential decadal-scale trends in observed precipitation isotope ratios (Putman et al., 2021).

Data analyses were primarily performed in Python 3.7 using the xarray (Hoyer & Hamman, 2017), cartopy (Met Office, 2010), and matplotlib (Hunter, 2007) packages. Linear regressions between modeled and observed isotope ratios or isotope ratios and tagged quantities within iCAM6 were performed in R, version 4.0.4 (R Core Team, 2021). All regressions were significant at the $P = 0.001$ level. Tagged quantities also provide a way to assess the relative importance of underlying processes to variations in water isotope ratios. We demonstrate this by fitting a random forest model (Breiman, 2001) to precipitation $\delta^{18}\text{O}$ and d-excess using the “ranger” R package (Wright & Ziegler, 2017). Variable importance was extracted from the model using the permutation method (Breiman, 2001). Each model was grown with a forest of 500 trees.

Table 2

Summary of Precipitation Observational Datasets Used to Validate iCAM6

Data set	Number of sites, $\delta^{18}\text{O}$	Number of sites, d-excess	Citation	Notes
Global network of isotopes in precipitation	567	537	IAEA/WMO (2021)	Mass-weighted values where available
Kurita et al., 2004	13	13	Kurita et al. (2004)	Mass-weighted values
Tibetan network of isotopes in precipitation	17	0	Yao et al. (2013)	Mass-weighted values
US network of isotopes in precipitation	73	0	Dutton et al. (2005), Vachon et al. (2010)	Unweighted annual and seasonal means calculated from Vachon et al. (2010)
Mongolian precipitation	15	15	Yamanaka et al. (2007)	Data retrieved from waterisotopesDB (Putman & Bowen, 2019), project ID 00084
Munksgaard et al. tropical precipitation compilation	19	19	Munksgaard et al. (2019)	Mass-weighted values where available

4. Results and Discussion

All simulations generally reproduce global mean precipitation well (Figure 2; Table 3), though biases in the spatial pattern of precipitation can be substantial. iCAM5 overestimates global precipitation by ~14% and 7% relative to the Global Precipitation Climatology Project (GPCP, Adler et al., 2003) and ERA5 global averages, respectively (Table 3). In contrast, iCAM6 simulated precipitation rates that were within 7% of both GPCP and ERA5, with or without nudging to ERA5 winds (Table 3). The global mean precipitation bias and mean absolute error relative to both the GPCP and ERA5 decrease from iCAM5 to iCAM6, with a notable reduction in a positive bias over the tropical oceans at the cost of an increased precipitation bias in the Amazon (Figure 2; Table 3; Bogenschutz et al., 2018). Biases are further reduced but not to zero when iCAM6 is nudged to ERA5 wind fields (Figure 2), indicating that a portion of the biases likely arise from the physical parameterizations of precipitation in addition to transport biases. Across the free-running simulations, precipitation is lower over the tropical oceans in iCAM6 than in iCAM5 (Figure S1), while adding nudging tendencies to the wind fields in iCAM6 increases tropical precipitation rates (Figure S1).

4.1. Isotope Ratios in iCAM6

Simulated precipitation isotope ratios in the free-running iCAM6 (Figures 3d–3f) show some notable differences from iCAM5 (Figures 3a–3c), particularly in the annual average and during northern hemisphere winter (Figure 3). In the annual average, precipitation $\delta^{18}\text{O}$ values are ~1–4‰ lower in iCAM6 (free) than in iCAM5 over North America, Greenland, northern Eurasia, and northern Africa, but 1–2‰ greater over southern Asia, the Arabian Peninsula, Australia, and Antarctica (Figures 3d–3f, 3j–3l). Over the oceans, precipitation $\delta^{18}\text{O}$ values tend to be slightly lower in the high latitudes and slightly higher in the mid-latitudes in iCAM6 (Figure 3c). Nudging the iCAM6 simulation to ERA5 (Figures 3g–3i) has a limited effect on precipitation $\delta^{18}\text{O}$ values over the ocean but has important regional impacts on precipitation $\delta^{18}\text{O}$ values over land (Figures 3m–3o). For example, the nudged iCAM6 simulation has $\delta^{18}\text{O}$ values that are 2–3‰ higher over central Africa, southern Asia, and Australia (Figures 3m–3o). Differences between $\delta^{18}\text{O}$ in the free and nudged simulations in iCAM6 are due to the additional constraints placed on moisture transport. In contrast, differences between the free-running iCAM5 and iCAM6 simulations are more likely to be related to updates to the convective schemes by implementing CLUBB and tuning the Zhang and McFarlane (1995) deep convection and Morrison-Gettelman microphysics (Gettelman & Morrison, 2015) parameterization schemes.

Seasonal differences between iCAM5 and iCAM6 can be much more significant, particularly in Northern Hemisphere winter (Figure 3, middle column). Mean DJF precipitation $\delta^{18}\text{O}$ values were generally lower north of 30°N in iCAM6 relative to iCAM5, with the largest differences observed over Mongolia and the

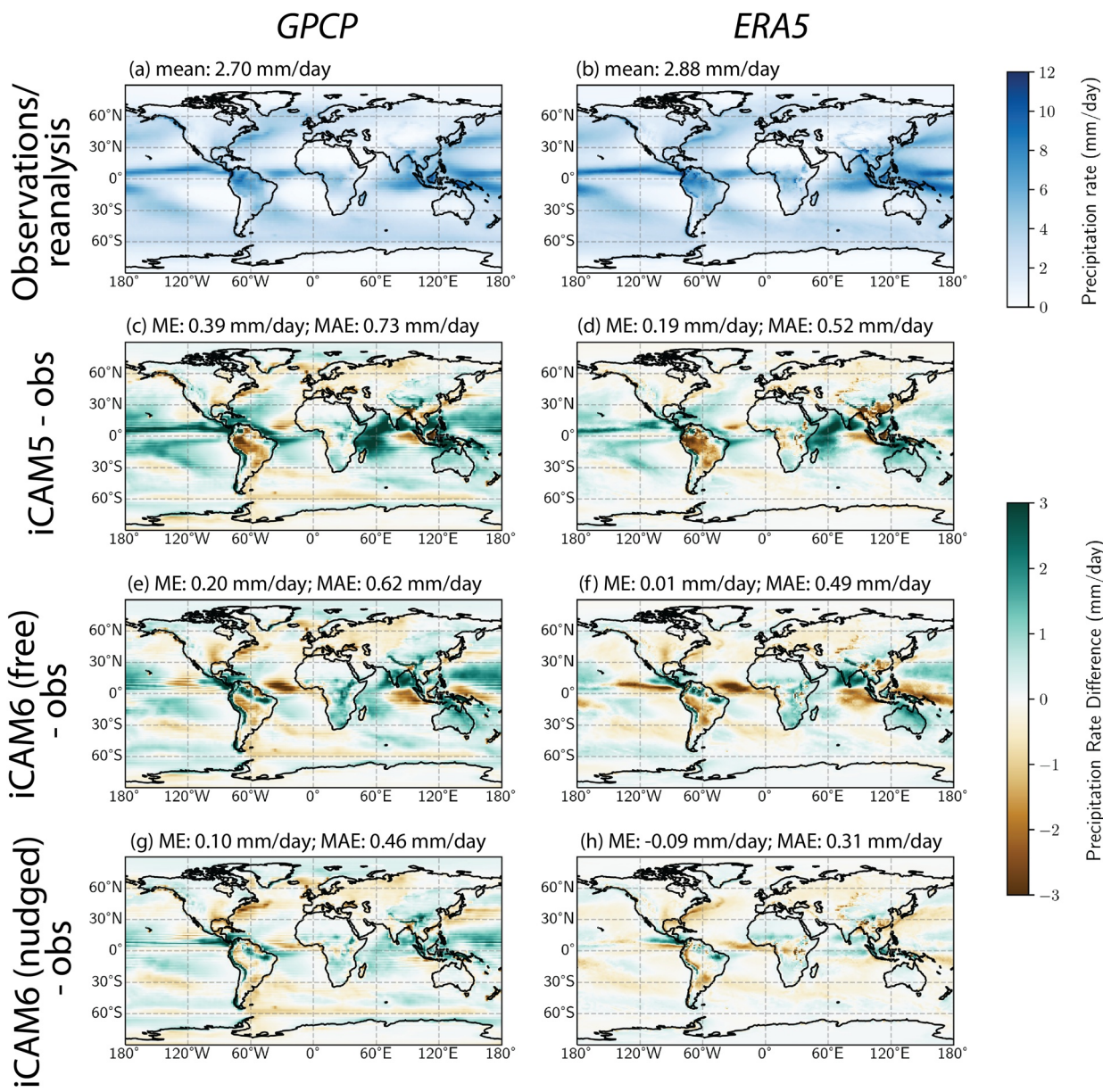


Figure 2. Mean annual precipitation rates from observations (panel a – Global Precipitation Climatology Program, GPCP) (Adler et al., 2003) and the ERA5 reanalysis (panel b) (Hersbach et al., 2020). The second, third, and fourth rows show the difference between modeled and observed precipitation rates for iCAM5, free-running iCAM6, and iCAM6 nudged to ERA5 winds, respectively. The global mean error (ME) and mean absolute error (MAE) for each difference is included for each figure panel, with MAE decreasing from iCAM5, to free-running iCAM6, to nudged iCAM6. GPCP and ERA5 precipitation rates were regressed to the iCAM6 model grid using a second-order conservative mapping scheme (Jones, 1999).

Tibetan plateau (Figure 3k). $\delta^{18}\text{O}$ values were also lower in iCAM6 across northern Africa and central South America when nudged to ERA5 but slightly higher in iCAM6 when forced only by SSTs. In the free-running iCAM6 simulation, $\delta^{18}\text{O}$ values were also higher in south and southeast Asia (particularly over India), Central America, Australia, and Antarctica (Figure 3k), and when nudged to ERA5, central Africa (Figure 3n). Over the ocean, DJF patterns were similar to annual means, with larger positive differences in the midlatitudes and larger negative differences in the Arctic Ocean (Figures 3k and 3n). In contrast, JJA differences between iCAM5 and iCAM6 (free) tended to be smaller. The largest positive $\delta^{18}\text{O}$ differences in JJA occur over Australia, with Antarctica and eastern North America also exhibiting higher $\delta^{18}\text{O}$ values in iCAM6 (free) relative to iCAM5 (Figure 3l). Positive JJA $\delta^{18}\text{O}$ differences extend to southern Asia and sub-Saharan Africa when iCAM6 is nudged to ERA5 (Figure 3o). Negative but small $\delta^{18}\text{O}$ differences in JJA were

Table 3
Comparison Between Modeled and Observed Mean Annual Precipitation Rates

Data source	Mean precipitation (mm/day)	Mean absolute error (relative to GPCP) (mm/day)	Mean absolute error (relative to ERA5) (mm/day)	Mean error (relative to GPCP) (mm/day)	Mean error (relative to ERA5) (mm/day)
GPCP	2.70	N/A	N/A	N/A	N/A
ERA5	2.88	N/A	N/A	N/A	N/A
iCAM5	3.08	0.73	0.52	0.39	0.19
iCAM6 (free)	2.89	0.62	0.49	0.20	0.01
iCAM6 (nudged)	2.79	0.46	0.31	0.10	-0.09

observed in western North America, northern Africa, northeastern Asia, Greenland, and western South America (Figures 3l and 3o). JJA differences in $\delta^{18}\text{O}$ values over the ocean were quite close to the annual mean (Figures 3l and 3o).

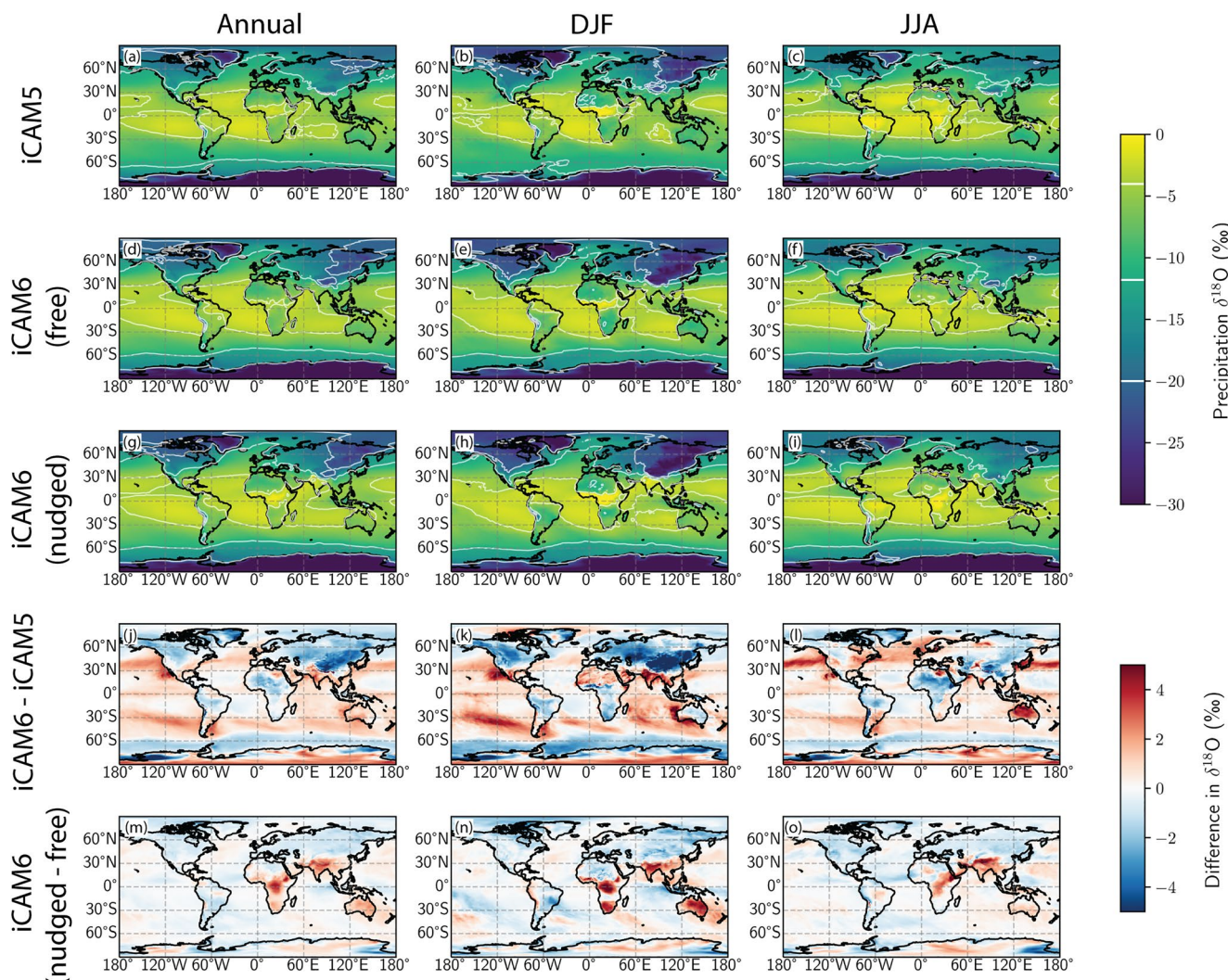


Figure 3. Comparison between annual (left column), DJF (middle column) and JJA (right column) mean precipitation $\delta^{18}\text{O}$ values in (a–c) iCAM5, (d–f) iCAM6 (free-running), (g–i) iCAM6 (nudged to ERA5), and (j–l) differences between iCAM6 (free) and iCAM5 and the (m–o) two iCAM6 simulations.

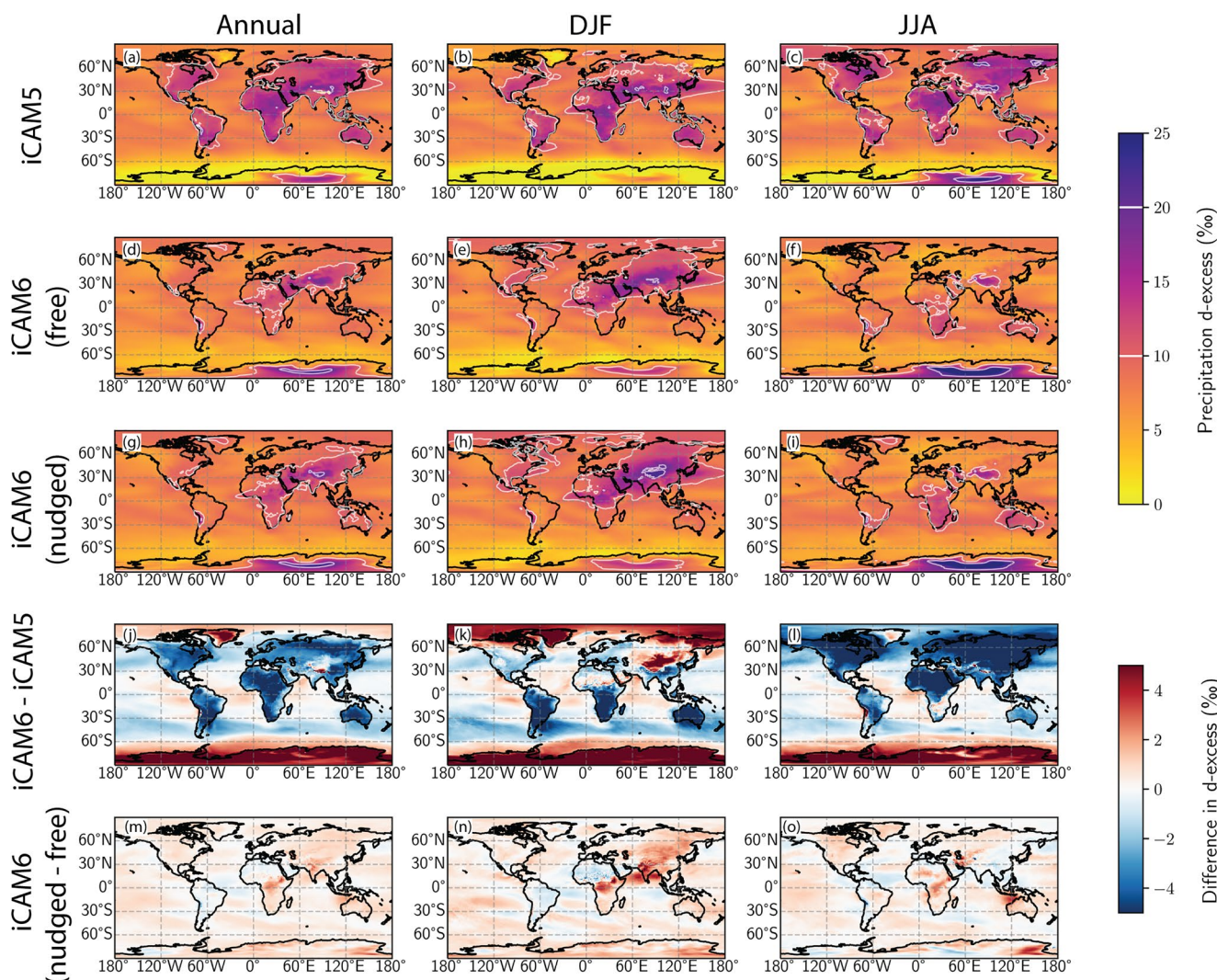


Figure 4. Comparison between annual (left column), DJF (middle column) and JJA (right column) mean precipitation d-excess values in (a–c) iCAM5, (d–f) iCAM6 (free-running), (g–i) iCAM6 (nudged to ERA5), and (j–l) differences between iCAM6 (free) and iCAM5 and the (m–o) two iCAM6 simulations.

Precipitation d-excess differences between iCAM5 (Figures 4a–4c) and iCAM6 (Figures 4d–4i) were more significant over land than over the ocean. Annual mean d-excess values decreased over land from iCAM5 to iCAM6 (free) by 5–10%, except in Antarctica and Greenland, where they increased by 5–10% (Figure 4j). Annual d-excess differences were generally smaller over the ocean but were positive in the tropics and high-latitudes and negative in the mid-latitudes (Figure 4j). The largest d-excess differences over the ocean occur in the Southern Ocean, where precipitation d-excess increased by ~5% (Figure 4j). In the nudged iCAM6 simulation, precipitation d-excess change from the free iCAM6 simulation was small in the annual average (Figure 4m), with increases of <1% observed in most regions. D-excess differences in DJF (Figure 4, middle column) and JJA (Figure 4, right column) were similar to the annual mean but with a few notable differences. First, DJF d-excess in iCAM6 was higher than in iCAM5 over south Asia, the Tibetan plateau, and the Arctic and Antarctica (Figure 4k). JJA differences in precipitation d-excess between iCAM6 and iCAM5 (Figures 4g–4i) were similar to the annual mean, but with larger negative differences over northern hemisphere land and smaller positive differences over Greenland (Figure 4i). We suspect the considerable differences in d-excess over land between iCAM6 and iCAM5 arise from two primary sources. First, in the iCAM5 simulation, the land model had a comprehensive treatment of isotope ratios throughout iCLM4.5 (Wong et al., 2017). In contrast, our iCAM6 simulations use land surface fluxes from CLM5 with a bucket hydrology model to determine flux isotope ratios (Appendix A). Second, several changes to

Table 4

Regression Summary Statistics Comparing iCAM6 and iCAM5 to Precipitation Observations

$\delta^{18}\text{O}$ Comparisons to observations		Slope (‰/‰)	Intercept (‰)	R^2	Mean absolute error (‰)
Annual	iCAM5 (free)	0.75 ± 0.02	-3.30 ± 0.17	0.712	1.39
	iCAM6 (free)	0.87 ± 0.02	-2.46 ± 0.19	0.727	1.54
	iCAM6 (nudged)	0.92 ± 0.02	-2.15 ± 0.19	0.741	1.63
DJF	iCAM5 (free)	0.57 ± 0.01	-4.80 ± 0.17	0.720	1.62
	iCAM6 (free)	0.71 ± 0.02	-4.27 ± 0.21	0.716	2.09
	iCAM6 (nudged)	0.77 ± 0.02	-3.68 ± 0.22	0.735	2.15
JJA	iCAM5 (free)	0.83 ± 0.02	-2.55 ± 0.15	0.740	1.38
	iCAM6 (free)	0.94 ± 0.02	-1.63 ± 0.16	0.753	1.42
	iCAM6 (nudged)	0.95 ± 0.02	-1.95 ± 0.15	0.784	1.42
JJA-DJF	iCAM5 (free)	0.44 ± 0.02	0.85 ± 0.10	0.487	1.63
	iCAM6 (free)	0.67 ± 0.02	1.20 ± 0.12	0.608	1.91
	iCAM6 (nudged)	0.71 ± 0.02	0.67 ± 0.12	0.654	1.88
d-excess Comparisons to observations		Slope (‰/‰)	Intercept (‰)	R^2	Mean absolute error (‰)
Annual	iCAM5 (free)	0.26 ± 0.04	8.17 ± 0.40	0.087	2.23
	iCAM6 (free)	0.20 ± 0.02	6.52 ± 0.20	0.169	1.27
	iCAM6 (nudged)	0.18 ± 0.02	6.89 ± 0.21	0.144	1.35
DJF	iCAM5 (free)	0.33 ± 0.03	7.11 ± 0.34	0.198	2.24
	iCAM6 (free)	0.23 ± 0.02	6.57 ± 0.23	0.194	1.55
	iCAM6 (nudged)	0.23 ± 0.02	7.03 ± 0.26	0.164	1.71
JJA	iCAM5 (free)	0.14 ± 0.03	9.44 ± 0.26	0.048	2.09
	iCAM6 (free)	0.24 ± 0.02	5.56 ± 0.20	0.192	1.33
	iCAM6 (nudged)	0.23 ± 0.02	5.65 ± 0.18	0.220	1.31
JJA-DJF	iCAM5 (free)	0.05 ± 0.02	0.02 ± 0.13	0.009	1.92
	iCAM6 (free)	0.21 ± 0.02	-0.99 ± 0.11	0.157	1.68
	iCAM6 (nudged)	0.23 ± 0.02	-1.39 ± 0.11	0.179	1.77

cloud parameterizations have been made from CAM5 to CAM6 (e.g., Bogenschutz et al., 2018), including a revision to the contact angle distributions (Wang et al., 2014) and how pre-existing ice crystals influence ice nucleation rates (Shi et al., 2015), and a new prognostic microphysics scheme (Gettelman et al., 2015). Together, these changes have allowed for higher supersaturation, reducing a bias that had been present in CAM5 (e.g., Kay et al., 2016). Higher supersaturation amounts and kinetic fractionation during ice nucleation has been linked to an increase in d-excess over Antarctica, and in wintertime isotope ratios in the high northern latitudes (e.g., Dütsch et al., 2019; Jouzel & Merlivat, 1984; Lowenthal et al., 2016).

Relative to site-level observations of precipitation $\delta^{18}\text{O}$ values (Table 4), the slope of the relationship between observed and modeled $\delta^{18}\text{O}$ values was closer to 1 for iCAM6 than iCAM5, suggesting an improved ability to capture the most negative precipitation $\delta^{18}\text{O}$ values (Figure 5a, Table 4). However, improvements in the modeled-vs-observed slope co-occur with an increase in $\delta^{18}\text{O}$ mean absolute error by ~0.4‰ on an annual basis from iCAM5 to iCAM6 (Table 4). iCAM6 also better captures the seasonality of observed precipitation $\delta^{18}\text{O}$ values relative to iCAM5 (Figure 5b and Table 4). Overall, both model versions capture the observed mean precipitation d-excess well (Table 4) but underestimate its variability (Figure 5d). As a result, the regression slopes between modeled and observed d-excess values are much smaller than unity. Nonetheless, the mean absolute error in precipitation improves by >0.5‰ from iCAM5 to iCAM6 (Table 4). Moreover, as with precipitation $\delta^{18}\text{O}$, iCAM6 exhibits an improved representation of the seasonal variations in precipitation d-excess (Figure 5d) relative to iCAM5, though both models strongly underestimate

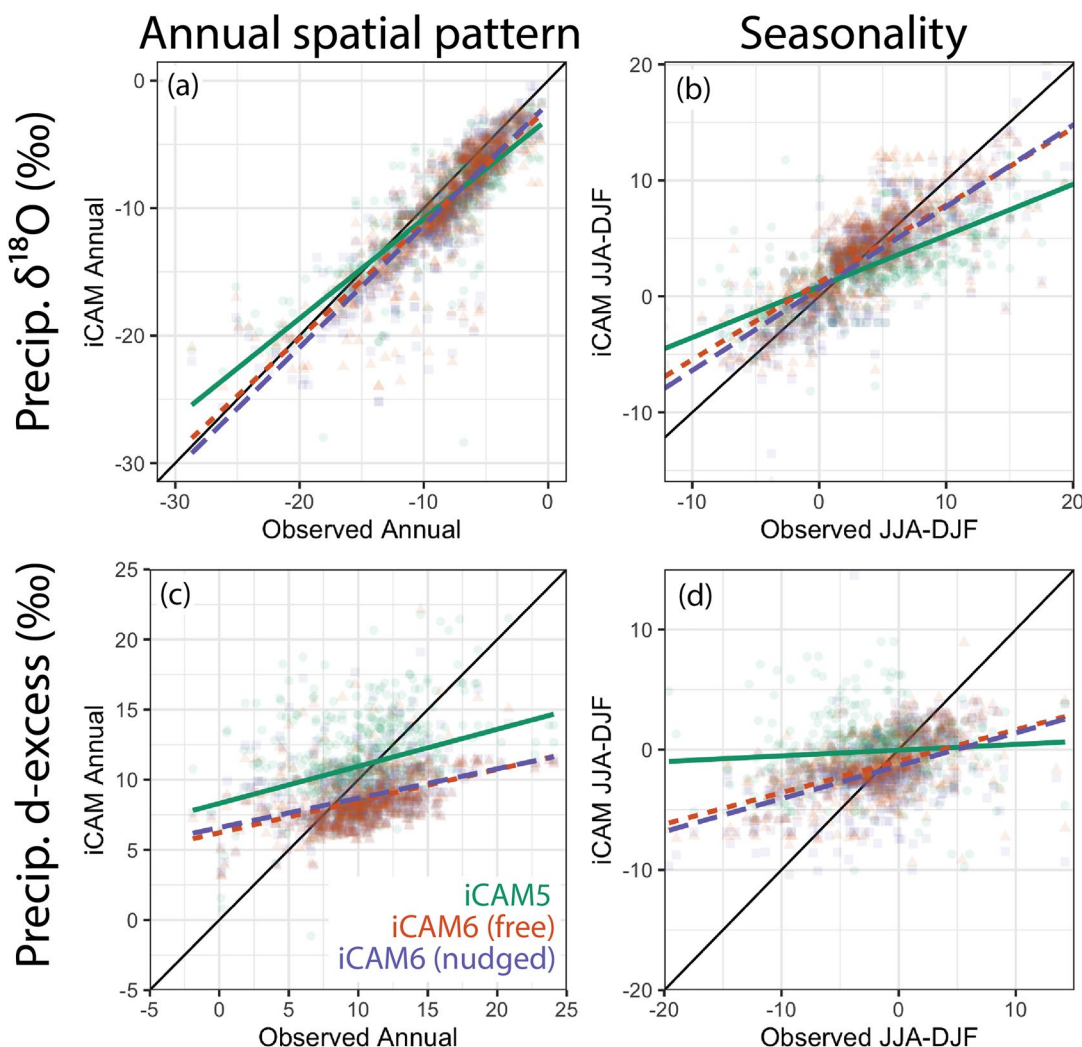


Figure 5. Comparison between iCAM5 (teal) and iCAM6 simulations (free – orange; nudged to ERA5 - purple) and precipitation isotope ratio observations ($\delta^{18}\text{O}$, a and b; d-excess, c and d). The left column captures the relationship between modeled and observed annual average isotope ratios across space, while the right column examines the ability of the model to capture the observed seasonality in isotope ratios (JJA mean – DJF mean).

the observed annual cycle in d-excess. Future model development could improve on this relationship by considering different parameterizations of the isotopic effects of evaporation (e.g., Craig & Gordon, 1965; Luz et al., 2009; Quade et al., 2018), supersaturation effects during condensation (e.g., Ciais & Jouzel, 1994; Dütsch et al., 2019; Jouzel & Merlivat, 1984), or sub-cloud hydrometeor evaporation and re-equilibration (e.g., Lee & Fung, 2008). We focus on the iCAM6 simulation nudged to the ERA5 reanalysis for the remainder of our analysis.

4.2. Relationships Between $\ln(f)$, $\delta^{18}\text{O}$, and Condensation Temperature

4.2.1. Evaluation of the Rayleigh Model Relationship Between $\ln(f)$ and $\delta^{18}\text{O}$

The traditional Rayleigh model involves water vapor evaporating at a single location and gradually raining out as it moves to colder latitudes. For a single vapor stream, this implies a roughly linear relationship between δ and $\ln(f)$ (Equation 20). However, this is a simplification for two reasons. First, water vapor that precipitates at a particular location originates from many different locations and may have mixed with other air masses containing different isotope ratios along the way. Second, fractionation depends on temperature and is not constant. Recently, simple models have been developed that apply the Rayleigh equations to a broad distribution of evaporation sources, and these have been shown to capture much of the observed meridional

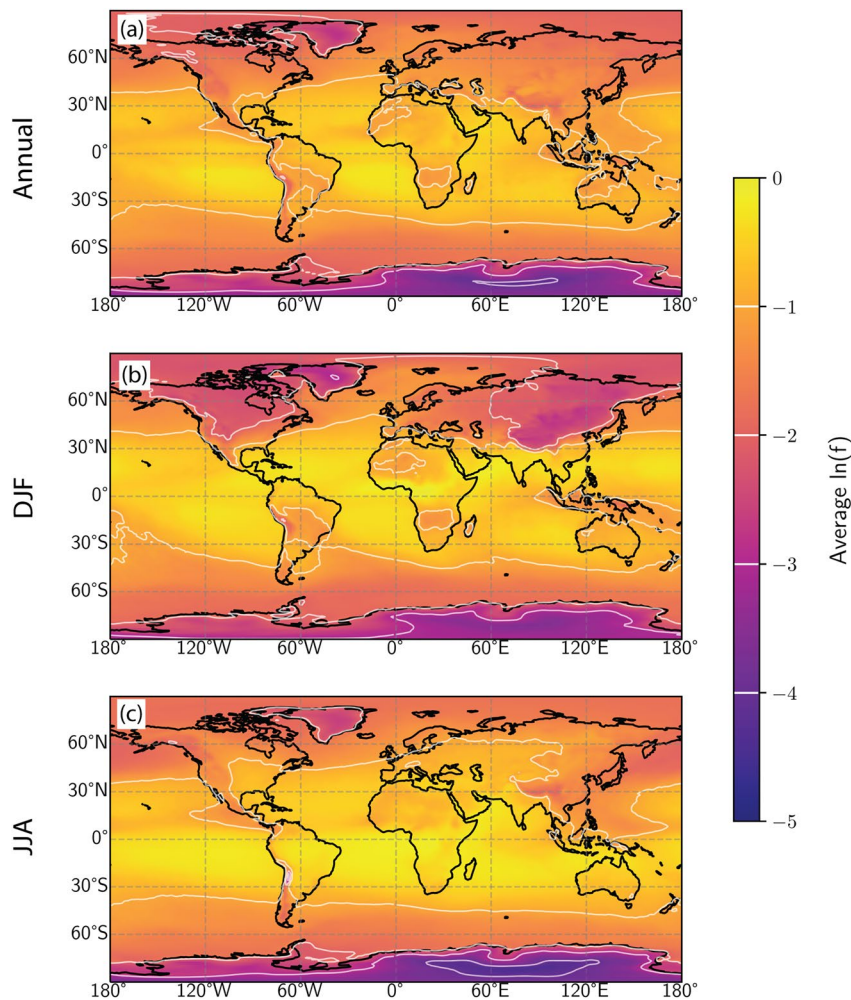


Figure 6. (a) Annual, (b) DJF, and (c) JJA precipitation-weighted mean $\ln(f)$ values. $\ln(f)$ decreases from the subtropics to the poles. In the mid- and high-latitudes, $\ln(f)$ is lower in the winter season, consistent with colder temperatures and a lower saturation vapor pressure.

pattern of precipitation isotopes, as well as its seasonal variability (Bailey et al., 2018; Siler et al., 2021). Furthermore, Siler et al. (2021) showed that variability in $\ln(f)$ drives the large majority of precipitation isotope variability in their model (what they call “hydrologic attenuation”), with the temperature dependence of α playing a far more minor role. However, both the Bailey and Siler models are 1-dimensional and thus do not fully represent a wide range of processes that could be important, including mixing of air parcels, entrainment and recycling of vapor along a parcel trajectory, and isotopic exchange between a rain droplet and its surroundings through evaporation or equilibration as it falls (Bailey et al., 2013; Blossey et al., 2010; Fiorella et al., 2018; Galewsky et al., 2016; Lee & Fung, 2008; Noone et al., 2011; Risi et al., 2008, 2021; Samuels-Crow et al., 2014; Stewart, 1975). Here we perform a more thorough test of the relative importance of these factors by introducing a numerical tag in which α and δ_0 are held constant, leaving only $\ln(f)$ as a free parameter.

Annual and seasonal $\ln(f)$ values generally decrease from equator to pole and with increasing elevation (Figure 6). Values of $\ln(f)$ tend to be between -1 and 0 in the tropics, suggesting values of f between 0.37 (i.e., 63% of the initial water vapor has been removed by precipitation) and 1 , while at higher latitudes and altitudes, values of $\ln(f)$ often range between -2 and -4 , corresponding to values of f between 0.02 and 0.14 (Figure 6). Lower values of $\ln(f)$ are generally observed in the winter hemisphere and are consistent with a larger fractional change in water abundance along a transport path from temperate mid-latitudes to polar environments with very low saturation vapor pressures.

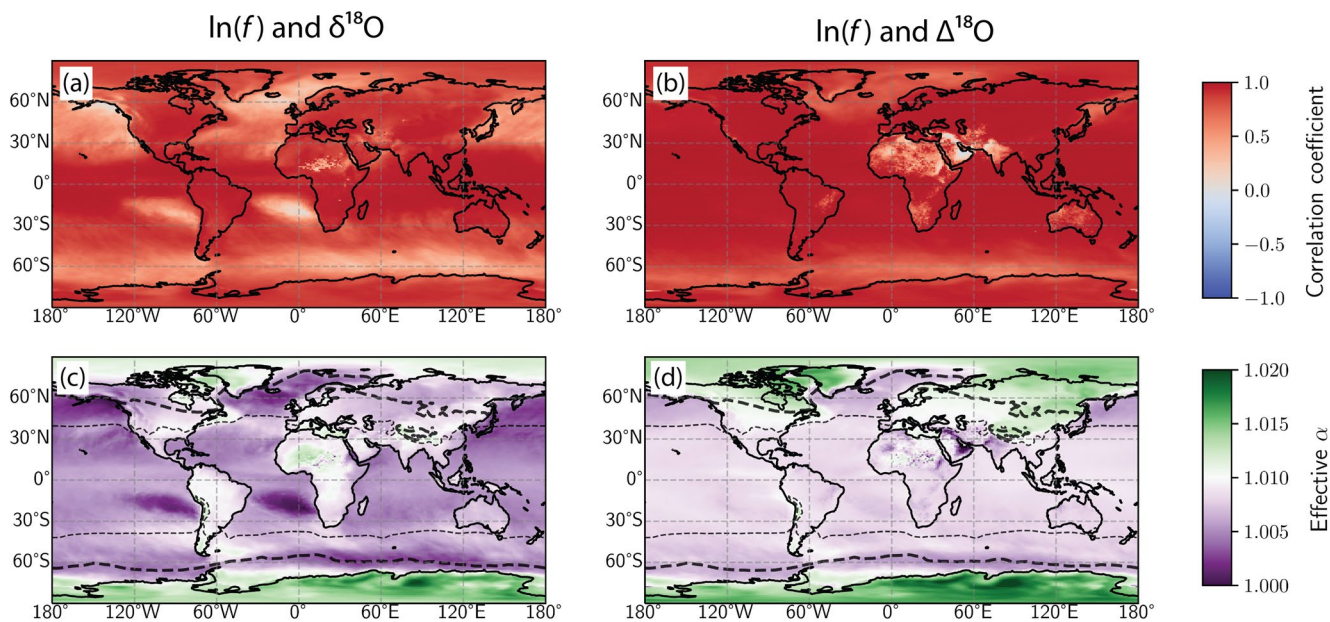


Figure 7. Correlation coefficients (a and b) and effective fractionation factors (c and d) between monthly $\ln(f)$ and $\delta^{18}\text{O}$ (a and c) or $\Delta^{18}\text{O}$ (b and d). Effective fractionation factors are determined by adding 1 to the linear regression slope between $\ln(f)$ and $\delta^{18}\text{O}$ or $\Delta^{18}\text{O}$ (Equation 20). Mean annual isotherms of 0°C and 15°C are shown in (c) and (d) as thick and thin dashed black lines, respectively.

Consistent with Siler et al. (2021), we find a strong spatial correlation between long-term monthly mean $\delta^{18}\text{O}$ value and $\ln(f)$ (Figures 7 and 8). This pattern indicates that water isotope ratios generally follow the Rayleigh distillation relationship in iCAM6 and are not primarily controlled by the temperature dependence of α . Correlation coefficients are >0.8 over land and the tropical ocean, while correlation coefficients are much lower over the oceans at $\sim 60^\circ$ latitude and the subtropical gyres (Figure 7a). If variations in the initial isotope ratio $\delta^{18}\text{O}_0$ are removed by comparing $\ln(f)$ to $\Delta^{18}\text{O}$, the correlation coefficient increases to >0.8 over land, except over the Sahara, the Arabian Peninsula, and portions of south-central Asia (Figure 7b), where correlations decrease. In contrast, correlation coefficients between $\ln(f)$ to $\Delta^{18}\text{O}$ over the ocean are high everywhere (Figure 7b). This pattern indicates that variations in $\delta^{18}\text{O}$ in regions where $\Delta^{18}\text{O}$ correlates more strongly with $\ln(f)$ are more strongly related to variations in $\delta^{18}\text{O}_0$ than variations in $\ln(f)$.

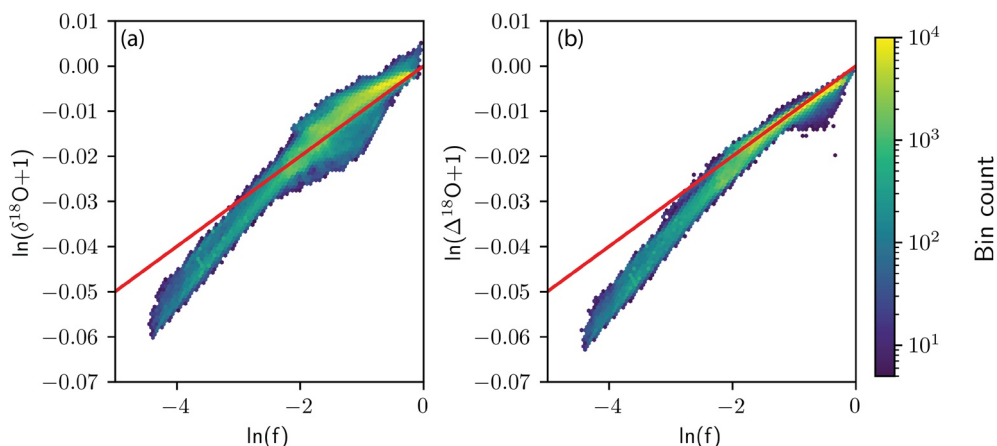


Figure 8. Relationships between $\delta^{18}\text{O}$ and $\ln(f)$ in long-term monthly averages. Panel (a) shows $\delta^{18}\text{O}$ that is uncorrected for variations in the isotope ratio of the initial vapor, $\delta^{18}\text{O}_0$. In panel (b), we correct for variations in $\delta^{18}\text{O}_0$ using $\Delta^{18}\text{O}$, which reduces most of the variability in precipitation isotope ratios with respect to the rainout fraction, $\ln(f)$, particularly above values of $\ln(f) = -1.6$. The red line corresponds to the expected relationship at constant $\alpha = 1.01$.

The slope of the relationship between long-term monthly $\ln(f)$ and $\delta^{18}\text{O}$ yields the effective fractionation factor α (= slope + 1) for that location (Figures 7c and 7d). Effective α values ranged from 1.0 (where correlation coefficients were low) to ~ 1.020 at high latitudes. In general, effective α values should increase with decreasing temperature (e.g., at high latitudes and elevations), but variations in $\delta^{18}\text{O}_0$ obscure the expected pattern (Figure 7c). However, the anticipated pattern emerges when variations in $\delta^{18}\text{O}_0$ are accounted for (Figure 7d).

The global regression fails to explain two significant features of the relationship between $\ln(f)$ and $\delta^{18}\text{O}$: (a) a change in the relationship around $\ln(f) = -1.6$, with a steeper slope for $\ln(f) < -1.6$ and a shallower slope for $\ln(f) > -1.6$, and (b) substantial scatter around the regression line for $\ln(f) > -1.6$. As a result, we consider the relationship between $\delta^{18}\text{O}$ value and $\ln(f)$ as two separate regressions for $\ln(f) \geq -1.6$ (corresponding to higher $\delta^{18}\text{O}$ values) and $\ln(f) < -1.6$ (corresponding to lower $\delta^{18}\text{O}$ values). Early studies of precipitation samples also noted this distinction (e.g., Dansgaard, 1964; Jouzel, Russell, et al., 1987; Noone & Simmonds, 2002). For $\ln(f) \geq -1.6$, the slope of the best-fit line suggests a lower $\alpha = 1.009$ ($R^2 = 0.77$), while the relationship for $\ln(f) < -1.6$ suggests a higher $\alpha = 1.015$ ($R^2 = 0.91$) (Figure 8a). Removing variations in $\delta^{18}\text{O}_0$ yields a better fit for both segments, with a particularly pronounced impact for high values of $\Delta^{18}\text{O}$ (Figure 8b). Therefore, variations in $\delta^{18}\text{O}_0$, perhaps arising from variations in the spatial pattern of evaporation (e.g., Siler et al., 2018, 2019) or the isotope ratio of the evaporative flux (e.g., Fiorella, West, & Bowen, 2019; Lee et al., 2008; Siler et al., 2021), explain much of the scatter in the relationship between $\delta^{18}\text{O}$ and $\ln(f)$. For $\ln(f) \geq -1.6$, the slope of the best-fit line between $\ln(f)$ and $\Delta^{18}\text{O}$ still suggests an $\alpha = 1.009$, but the relationship with $\ln(f)$ now explains 96% of the variance rather than 77% ($R^2 = 0.96$). For $\ln(f) < -1.6$, $\ln(f)$ now explains 96% ($R^2 = 0.96$) of the variance (instead of 91%) while the inferred mean α remains 1.015. The curvature observed in the relationship between $\ln(f)$ and $\delta^{18}\text{O}$ is not unexpected since α increases with decreasing temperature, which will generally decrease along with $\ln(f)$. As a result, the slope between $\ln(f)$ and $\delta^{18}\text{O}$ should increase as $\ln(f)$ decreases.

4.2.2. Relationships With Controlling Conditions

Several prior studies have also sought to link variations in precipitation isotope ratios to air or condensation temperatures (Dansgaard, 1964; Kohn & Welker, 2005; Rindsberger et al., 1983; Rozanski et al., 1993), as these factors should influence both the fractionation factor α and the saturation vapor pressure (and therefore, f). The process-oriented tagging framework allows direct comparison of isotope ratios and mean condensation temperatures. Mean annual condensation temperatures ranged from 295 to ~ 230 K and decrease with increasing latitude and elevation (Figure 9). The range of mean condensation temperatures observed during Northern Hemisphere winter was smaller (231–296K) than during Southern Hemisphere winter (210–306K) (Figures 9b and 9c). Condensation temperature positively correlates with precipitation $\delta^{18}\text{O}$ over the mid- and high latitudes, with stronger correlations generally observed over land than over the ocean on monthly (Figure 10a) and interannual (Figure 10b) timescales. The sensitivity of precipitation $\delta^{18}\text{O}$ to changes in condensation temperature ranges from 0.2–0.6‰/K in the mid-latitude to $>1.0\text{‰}/\text{K}$ in Greenland, Antarctica, and the Andean mountain ranges (Figures 10c and 10d). In contrast, negative correlations between condensation temperature and precipitation $\delta^{18}\text{O}$ occur for all land areas equatorward of 30°, the ITCZ, and the Indian and western Pacific oceans (Figures 10a and 10b). Variations driven by the annual cycle (Figures 10a and 10c) and by interannual variability (Figures 10b and 10d) exhibit similar patterns.

Sensitivity of precipitation $\delta^{18}\text{O}$ to changes in condensation temperature is often $<-1.0\text{‰}/\text{K}$ over the western Amazon, central America, central Africa, and the Maritime continent, while in the western Pacific and Southeast Asia, it is often between -0.5 and $-1.0\text{‰}/\text{K}$ (Figures 10c and 10d). The positive relationship between precipitation $\delta^{18}\text{O}$ and condensation underpins the “temperature effect” (Dansgaard, 1964; Kohn & Welker, 2005; Rozanski et al., 1993) and suggests rainout in these regions is primarily temperature controlled. In contrast, tropical precipitation $\delta^{18}\text{O}$ is negatively correlated with changes in condensation temperature but positively correlated with $\ln(f)$ and is likely related to the “amount effect.” The amount effect, first described by Dansgaard (1964), refers to an apparent anticorrelation between precipitation amounts and $\delta^{18}\text{O}$ values one some relevant time scale (Dansgaard, 1964; Rozanski et al., 1993), though considerable variation in this relationship and the underlying mechanism exists (Bowen et al., 2019; Cai & Tian, 2016; Conroy et al., 2016; Fiorella, Poulsen, Pillco Zolá, Barnes, et al., 2015; Vimeux et al., 2005).

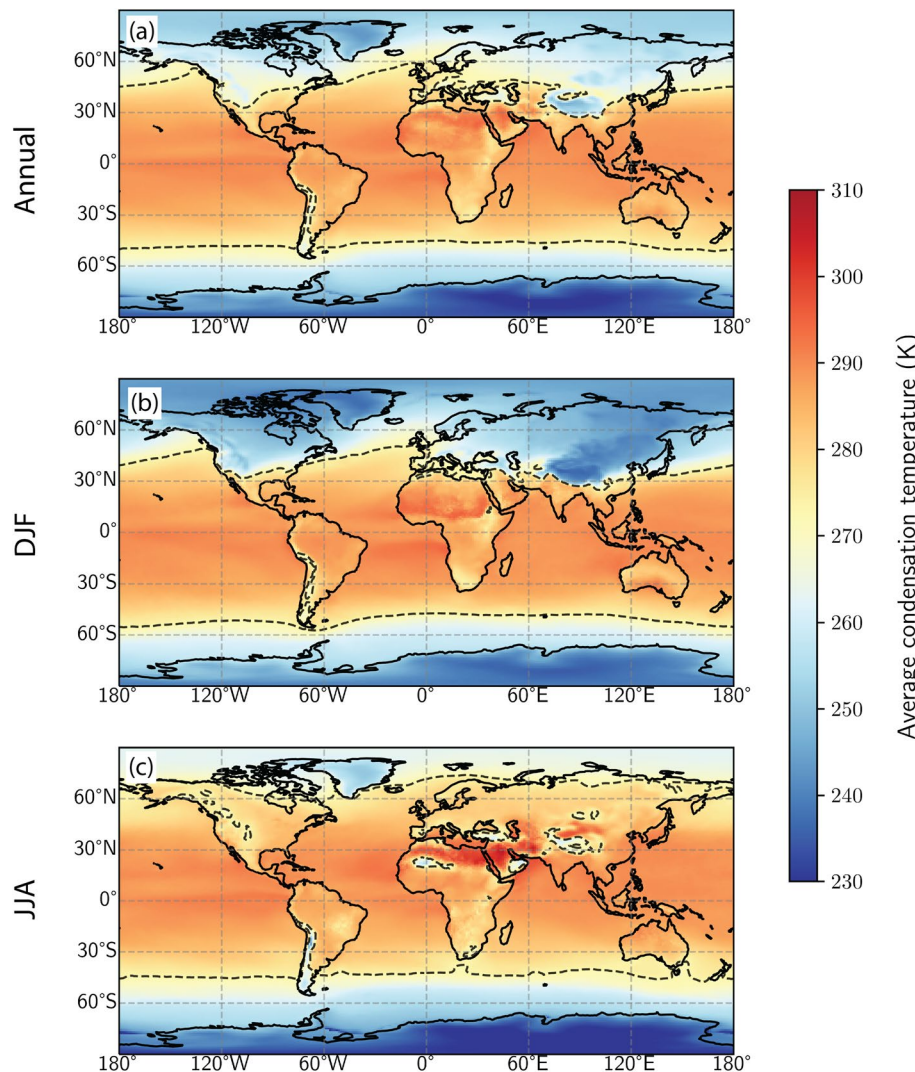


Figure 9. Mean condensation temperature (K) annual (a) or seasonal (b – DJF; c-JJA) means. Mean condensation temperatures generally decrease with increasing elevation and latitude and are lower in the winter hemisphere. A dashed black line indicates the 273K isotherm.

4.3. Precipitation $\delta^{18}\text{O}$, Atmospheric Residence Time, and Transport Distance

4.3.1. Precipitation $\delta^{18}\text{O}$ and Residence Time

The residence time (RT) of tropospheric water vapor is a fundamental characteristic of the hydrological cycle relating the mass of water in the atmosphere to the water fluxes into and out of the atmosphere. On a global scale, the RT of atmospheric water is the mass of water in the atmosphere, Q , divided by the evaporation or precipitation rate, assuming a hydrological cycle that is approximately in steady state. Most estimates of the atmospheric water RT are around 8–10 days (Bosilovich, 2002; Trenberth, 1998; van der Ent & Savenije, 2011; van der Ent & Tuinenburg, 2017). A few estimates of the global atmospheric water RT have diverged from this consensus—for example, Läderach and Sodemann (2016) suggested that the global RT is closer to 4–5 days, while other authors have suggested that the implied evaporation rates in this study are too large (van der Ent & Tuinenburg, 2017).

Due to atmospheric warming, the water vapor RT is likely changing. A consistent feature across climate models is that specific humidity increases with temperature close to Clausius-Clapeyron scaling, but precipitation increases less rapidly (Held & Soden, 2006). As a result, the mean water vapor atmospheric RT must increase. Aggarwal et al. (2012) proposed that variations in site-level precipitation isotope ratios were

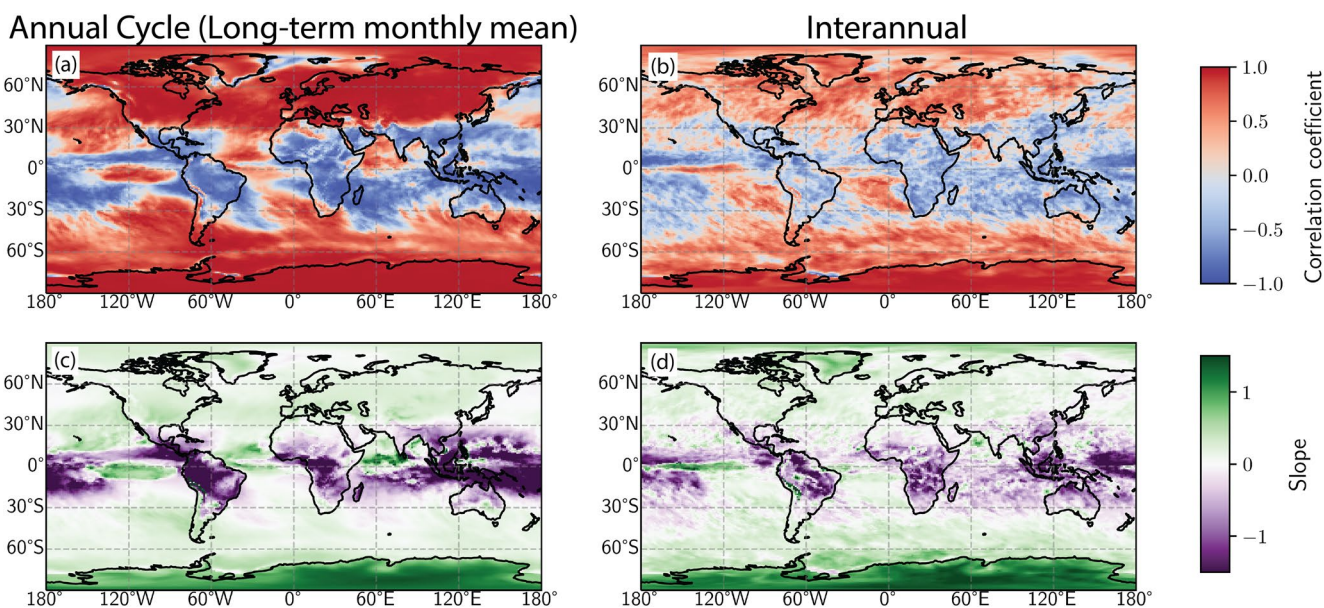


Figure 10. (a and c) Long-term monthly and (b and d) interannual correlation coefficients (a and b) and regression slopes (c and d) between mean precipitation $\delta^{18}\text{O}$ and mean condensation temperature (K). Condensation temperature and precipitation $\delta^{18}\text{O}$ correlate strongly and positively in the mid and high-latitudes but negatively in the low-latitudes.

correlated with the atmospheric RT of the moisture comprising the precipitation. However, the definition of atmospheric RT used for individual locations in Aggarwal et al. (2012) was the global definition of the RT, Q/P . However, this definition is unlikely to hold at sub-global scales as it neglects the importance of moisture transport, particularly in the mid-latitudes and over land where $P > E$ on an annual basis. Instead, Q/P for a particular location is better thought of as a “depletion” time (DT) (Trenberth, 1998). With a detailed accounting of the water cycle enabled by the integrative tags that explicitly capture the airborne time (Sections 2.3; 3.2), we reexamine relationships between RT, the local ratio of column humidity to precipitation (Q/P), and precipitation $\delta^{18}\text{O}$.

Clear differences between the moisture DT and RT are observed (Figure 11). Moisture RT simulated by tags in iCAM6 tends to be higher over land than over the ocean, with annual average residence times of 8–20 days over land and 4–12 days over the ocean (Figure 11a). Residence times over the ocean are highest in the ITCZ and at high latitudes and lowest in the subtropics (Figure 11a). Over land, the longest residence times are in the high latitudes and the subtropics and the lowest in the deep tropics and midlatitudes (Figure 11a). Seasonally, moisture residence times are longer in the summer hemisphere and shorter in the winter hemisphere (Figures 11c and 11e), with summer hemisphere residence times often exceeding 10 days and winter residence times usually below 10 days. A notable exception to this trend is central Asia, which exhibits long (>15 days) residence times in winter, presumably due to the long transport distances and lower land ET fluxes over Eurasia (Figure 11c).

Depletion times, by contrast, exhibit a distinctly different pattern. Depletion times are always high in the subtropics due to meager precipitation rates (>20 days), where they are usually at least a week longer than modeled residence times and decrease from the subtropics to the poles (Figures 11b, 11d and 11f). Seasonally, depletion times are longer in the winter hemisphere in the mid- and high-latitudes, though this effect is stronger in the northern hemisphere (Figure 11d) than in the southern hemisphere (Figure 11f).

Considered globally, the relationship between monthly mean residence time and depletion times is surprisingly weak ($DT = -0.92RT + 29.8$, $R^2 = 0.006$; Figure 12a). Precipitation $\delta^{18}\text{O}$ exhibits stronger relationships with depletion and residence times than these metrics exhibit with each other (Figure 12). Precipitation $\delta^{18}\text{O}$ is positively correlated with $\log(DT)$ ($\delta^{18}\text{O} = 7.69\log_{10}(DT) - 16.45$, $R^2 = 0.284$, Figure 12b), which mirrors a result Aggarwal et al. (2012) where depletion and residence times were assumed to be equivalent. In contrast, precipitation $\delta^{18}\text{O}$ was negatively correlated with residence time in iCAM6

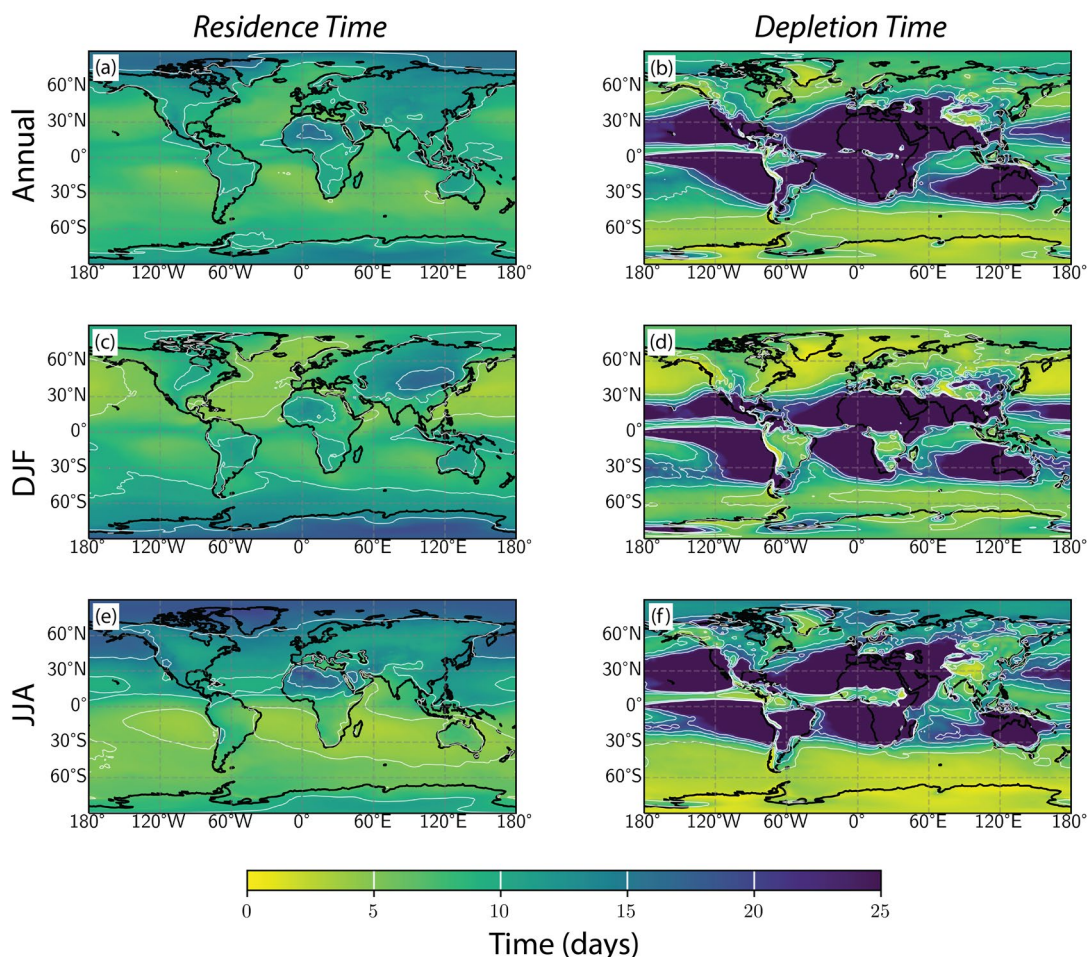


Figure 11. (a and b) Annual average, (c and d) DJF, and (e and f) JJA moisture residence times (a, c, and e), calculated by process-oriented tags (left column), and moisture depletion times (b, d, and f) in iCAM6, calculated as total column humidity divided by the precipitation rate (right column).

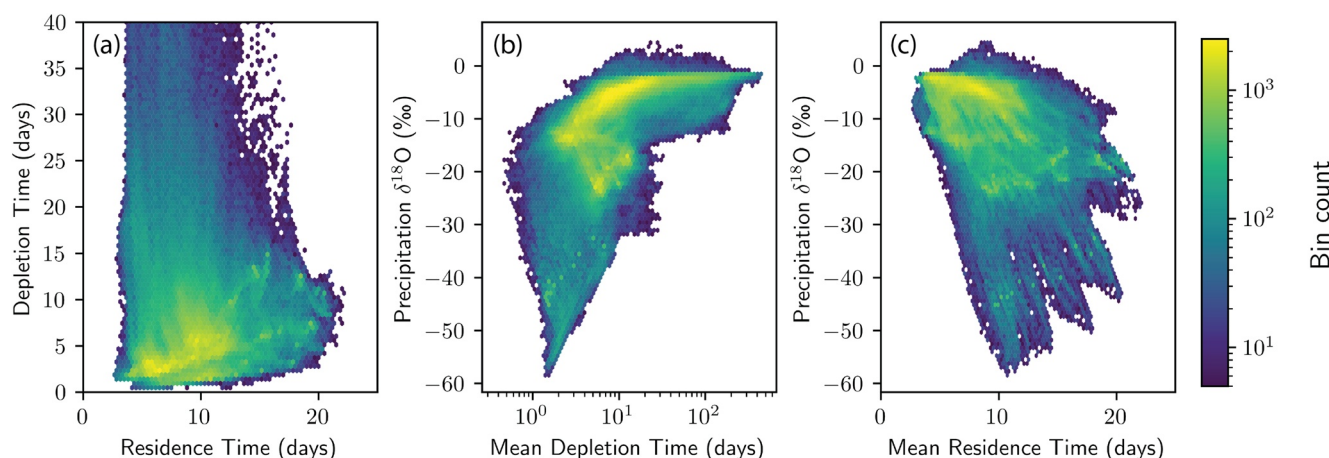


Figure 12. Relationship between long-term average monthly (a) depletion and residence times, and precipitation $\delta^{18}\text{O}$ and (b) mean depletion times and (c) residence times in iCAM6. Depletion times in panel (b) are log-scaled for consistency with Aggarwal et al. (2012).

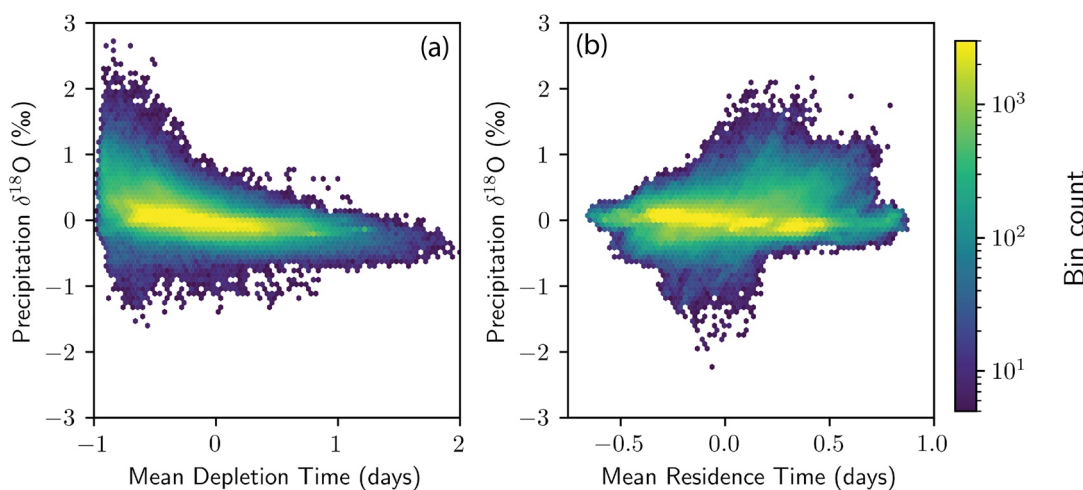


Figure 13. Relationships between anomalies from the long-term monthly mean precipitation $\delta^{18}\text{O}$ and anomalies from the (a) mean depletion time and (b) residence time.

($\delta^{18}\text{O} = -0.97\text{RT} - 0.09$, $R^2 = 0.193$; Figure 12c). The relationship between DT and $\delta^{18}\text{O}$ matches the result from Aggarwal et al. (2012), but the opposite relationship is observed between RT and $\delta^{18}\text{O}$.

Much of the spread in the relationships between precipitation $\delta^{18}\text{O}$, RT, and DT may arise from spatial variations in $\delta^{18}\text{O}$ and its response to $\ln(f)$ and temperature (Figures 3, 5, 6, 8, and 9). In their study that sought to establish a relationship between DT and precipitation $\delta^{18}\text{O}$, Aggarwal et al. (2012) accounted for these variations by considering normalized anomalies of DT and precipitation $\delta^{18}\text{O}$:

$$\Delta DT = \frac{DT - \overline{DT}}{\overline{DT}} \text{ or } \Delta \delta^{18}\text{O} = \frac{\delta^{18}\text{O} - \overline{\delta^{18}\text{O}}}{\overline{\delta^{18}\text{O}}} \quad (22)$$

where the overbar refers to longer-term average values (e.g., seasonal or annual). Positive values of ΔDT indicate anomalously long DT, while positive values of $\Delta \delta^{18}\text{O}$ indicate anomalously low $\delta^{18}\text{O}$ values. Based on observations from the GNIP archive, Aggarwal et al. (2012) determine a best-fit line of $\Delta \delta^{18}\text{O} = -0.4\Delta DT$. We find a similar relationship in iCAM6 between $\Delta \delta^{18}\text{O}$ and ΔDT ($\Delta \delta^{18}\text{O} = -0.38\Delta DT - 0.01$; $R^2 = 0.169$; Figure 13a). However, the relationship between $\Delta \delta^{18}\text{O}$ and ΔRT is more nuanced. Globally, $\Delta \delta^{18}\text{O}$ and ΔRT are positively correlated but with considerable scatter around this relationship ($\Delta \delta^{18}\text{O} = 0.26\Delta RT + 0.07$; $R^2 = 0.03$; Figure 13b). Overall, the patterns between $\delta^{18}\text{O}$ and DT (or $\Delta \delta^{18}\text{O}$ and ΔDT) observed in Aggarwal et al. (2012) are also observed in iCAM6, but the opposing trend is observed between $\delta^{18}\text{O}$ and RT and the relationship between $\Delta \delta^{18}\text{O}$ and ΔRT is weak. The spatial correlation pattern between monthly and interannual $\delta^{18}\text{O}$ and RT suggests two distinct modes of variation that are not apparent from the global relationships alone (Figures 14a and 14b). On monthly timescales, $\delta^{18}\text{O}$ and RT are negatively correlated throughout most of the tropics, portions of central North America, and eastern and northern Asia (Figure 14a), with the slope of this relationship falling below $-2\text{‰}/\text{day}$ over the Andean and Tibetan plateaus (Figure 14c). In contrast, $\delta^{18}\text{O}$ and RT are positively correlated elsewhere (Figure 14a), with regression slopes exceeding $2\text{‰}/\text{day}$ in Antarctica (Figures 14b and 14c). On interannual timescales, the mode where RT and $\delta^{18}\text{O}$ are negatively correlated expands to include most of North America, Europe, and the Southern Ocean (Figures 14b and 14d). Taken together, these relationships indicate that: (a) precipitation $\delta^{18}\text{O}$ tends to be lower when comprised of vapor that has spent more time in the atmosphere, (b) precipitation $\delta^{18}\text{O}$ tends to be higher in regions where column Q/P is large, perhaps due to the rarity of conditions favoring precipitation in these regions, and (c) anomalously low precipitation $\delta^{18}\text{O}$ values are associated with anomalously short DT. Therefore, the conclusions of Aggarwal et al. (2012) are robust with respect to DT, but not RT as had been claimed.

4.3.2. Precipitation $\delta^{18}\text{O}$ and Moisture Transport Distance

The mean distance traveled by water between evaporation and precipitation (Figure 15) is low in the subtropics during all seasons, suggesting that precipitation in these regions forms from locally derived

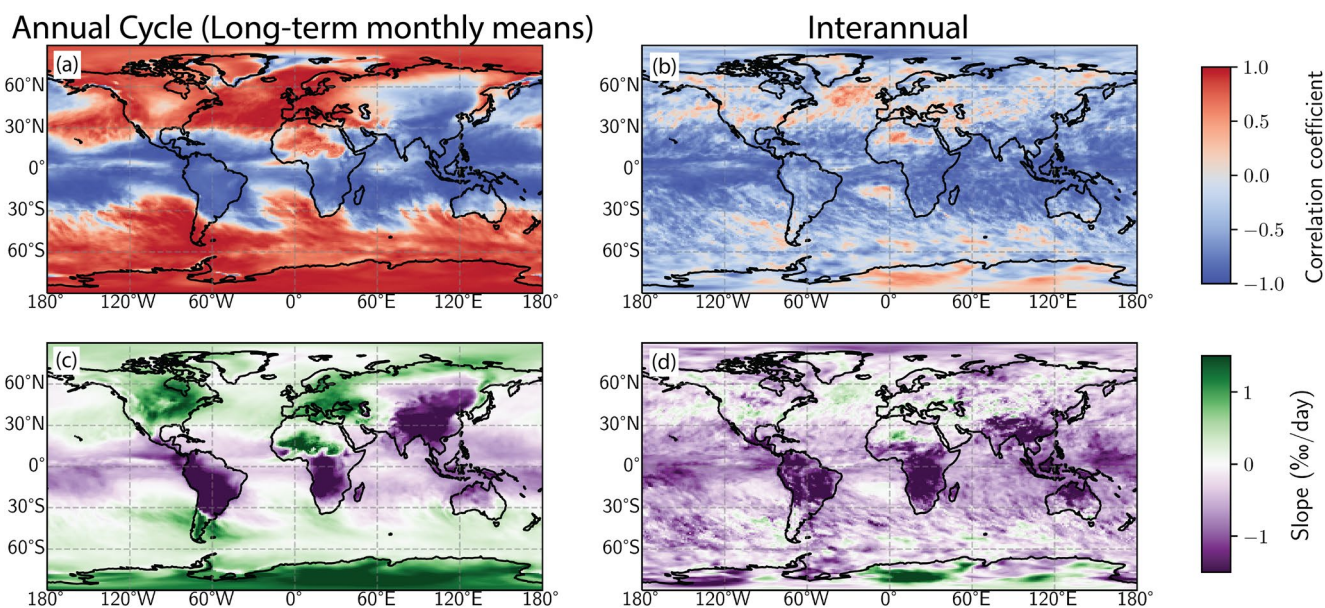


Figure 14. (a and c) Long-term monthly and (b and d) interannual correlation coefficients (a and b) and regression slopes (c and d) precipitation $\delta^{18}\text{O}$ and moisture RT.

moisture. Transport distances from the subtropics increase both poleward and equatorward. In the northern hemisphere, mean transport distances are longer in the winter than in the summer over most of northern Asia, Europe, and North America (Figure 15b). In contrast, mean transport distances are longer in the summer than in the winter in south and east Asia (Figure 15c). In the southern hemisphere, mean transport distances are longer in winter than in summer over the ocean but longer in summer than winter over land, particularly in the monsoon regions of South America, sub-Saharan Africa, Indonesia, and Australia (Figures 15b and 15c). Transport distances over Antarctica are always large, particularly in austral summer, consistent with the idea that the dominant moisture sources to Antarctica are the subtropics or the mid-latitudes (Bailey et al., 2019; Masson-Delmotte et al., 2008; Noone & Simmonds, 2002; Sodemann & Stohl, 2009).

Transport distance and precipitation $\delta^{18}\text{O}$ values are generally negatively correlated over land (Figure 16a), reminiscent of the “continental effect” documented in early spatial analyses of precipitation isotope ratios (Dansgaard, 1964; Rozanski et al., 1993). The continental effect refers to the tendency of precipitation isotope ratios to decrease over continents in the direction of the prevailing winds as water leaves the parcel through precipitation. Over the mean annual cycle, transport distance and precipitation $\delta^{18}\text{O}$ values are negatively correlated throughout Australia, the Maritime Continent, Africa, Asia, and all but the southernmost portion of South America and the westernmost portion of North America (Figure 16a). In contrast, mean transport distance and precipitation $\delta^{18}\text{O}$ values are positively correlated in Europe, Antarctica, Greenland, the southern tip of South America, and westernmost North America (Figure 16a). On an interannual basis, transport distance remains negatively correlated with precipitation $\delta^{18}\text{O}$ in the low latitudes but is often positively correlated over northern Hemisphere continents (Figure 16b). The slope of the relationship between monthly transport distance and precipitation $\delta^{18}\text{O}$ is generally between -0.5 and $-1.0\text{ \%}/1000\text{ km}$ over land, except for Europe, western North America, southern South America, Greenland, and Antarctica, where the slope is often between 0.5 and $1.0\text{ \%}/1000\text{ km}$ (Figure 16c). The slope of the relationship on an interannual basis is generally smaller in magnitude and ranges from -0.5 to $0.5\text{ \%}/1000\text{ km}$ except for the Andean and Himalayan fronts and central Antarctica (Figure 16d). We suspect that the relationships between monthly mean transport distance and precipitation $\delta^{18}\text{O}$ values reflect both the continental effect and the seasonal cycles in both variables in the mid-latitudes (Figures 3 and 15).

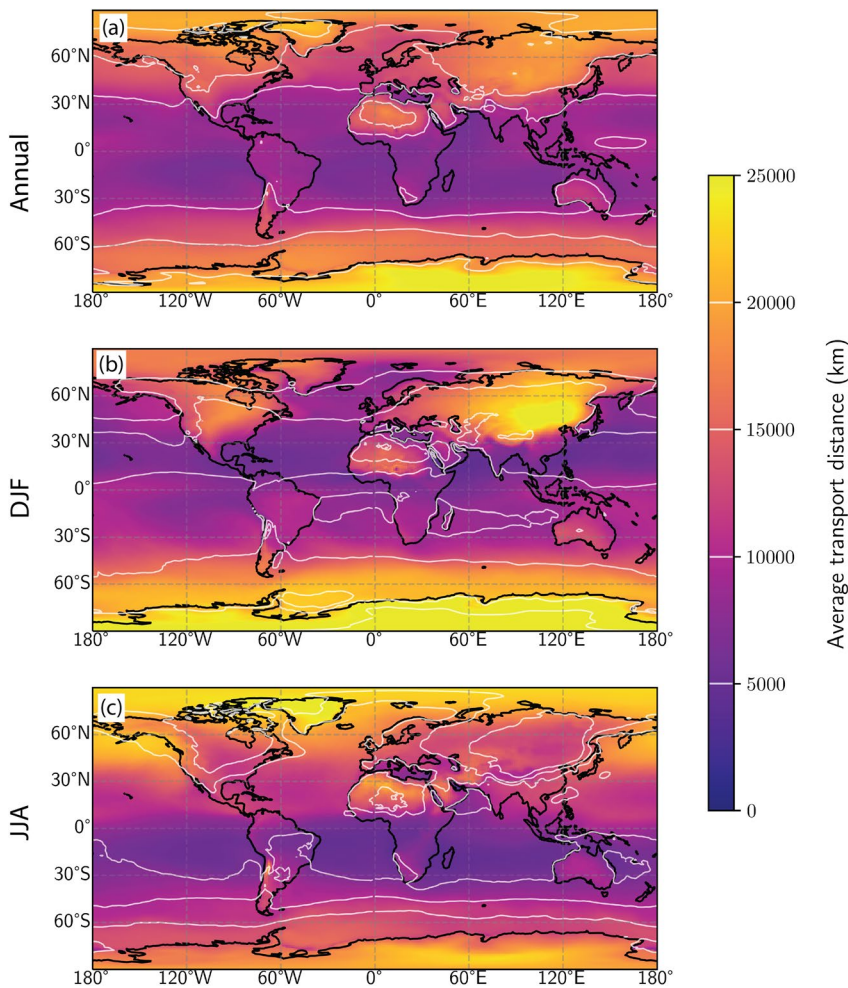


Figure 15. (a) Annual, (b) DJF, and (c) JJA precipitation-weighted mean transport distances (km).

4.4. Relationships Between d-excess and Evaporative Conditions

Precipitation d-excess is often thought to reflect variations in the mean evaporative conditions experienced by an air parcel. In this framework, water vapor obtains its d-excess during evaporation and is not substantially affected by condensational loss, at least until f is very low and most of the parcel water has been removed (Bony et al., 2008; Fiorella, Bares, et al., 2019). As a result of this (approximate) conservation property, d-excess has been used in several contexts to examine variations in evaporative conditions or moisture sources. First, the d-excess of precipitation (Bowen et al., 2012; Froehlich et al., 2008; Salati et al., 1979) and water vapor (Aemisegger et al., 2014; Fiorella et al., 2018; Lai & Ehleringer, 2011; Parkes et al., 2017; Welp et al., 2012) has been used to investigate the role of moisture “recycling” in the continental water cycle. Second, due to substantial variations in evaporation d-excess associated with meteorological factors such as temperature, relative humidity, and wind speed (Benetti et al., 2014; Merlivat & Jouzel, 1979; Pfahl & Wernli, 2008; Uemura et al., 2008), d-excess has also been used to investigate variations in moisture source regions or conditions. For example, ice-core d-excess has been widely used in paleoclimatic reconstructions, but even after half a century of work, there remains debate over its interpretation (Jouzel et al., 1982; Masson-Delmotte, 2005; Pfahl & Sodemann, 2014; Vimeux et al., 1999).

Modeled d-excess values in iCAM6 generally support the expectation that d-excess is nearly conserved between evaporation and condensation (Figure 17), except in regions where $\ln(f)$ is lower than -3 (Figure 6). The change in d-excess between evaporation and condensation was generally $<2\%$ in magnitude on an annual scale, except at high elevations (e.g., the Tibetan and Andean plateaus) or high latitudes (Figure 17a),

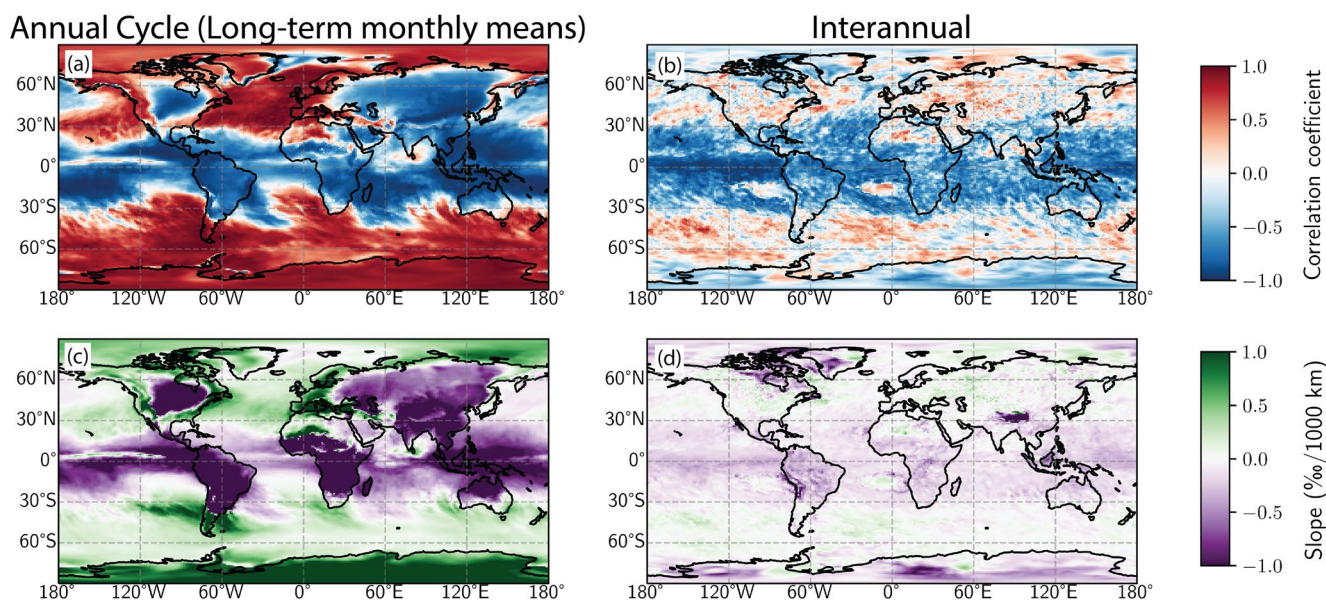


Figure 16. (a and c) Long-term monthly and (b and d) interannual correlation coefficients (a and b) and regression slopes (c and d) between precipitation $\delta^{18}\text{O}$ and moisture transport distance.

where precipitation d-excess has increased above evaporation values by $>4\%$. High elevation and high latitude areas also exhibit high differences between evaporation and precipitation d-excess throughout the annual cycle (Figures 17b and 17c). In contrast, in low elevation areas in the mid- and low-latitudes, precipitation d-excess values are lower than their evaporation values during summer but higher than their evaporation values in the winter (Figures 17b and 17c). In the summer, a difference between evaporation and precipitation d-excess $<0\%$ is consistent with sub-cloud evaporation of falling rain droplets, which would lower the d-excess of precipitation reaching the surface (Lee & Fung, 2008; Stewart, 1975). In contrast, winter changes in d-excess between evaporation and condensation $>0\%$ likely arise from the lower $\ln(f)$ values during the winter, where d-excess begins to increase rapidly as $\ln(f)$ decreases. However, these variations are relatively small, and the assertion that d-excess values are roughly conserved between evaporation and condensation is valid except when $\ln(f)$ is low (Figure 17).

Based on these trends, and excluding Antarctica, we consider the relationships between d-excess in precipitation and the mean conditions during evaporation, determined by tagging evaporation relative humidity, temperature, and wind speed (Figure 18). Precipitation d-excess is negatively correlated with evaporation relative humidity ($d [\%] = -0.17\text{RH}[\%] + 18.09, R^2 = 0.194$; Figure 18a) and wind speed ($d [\%] = -0.61u [\text{m/s}] + 12.27, R^2 = 0.168$; Figure 18c) but positively correlated with evaporation temperature ($d [\%] = 0.13 T [\text{K}] - 29.41, R^2 = 0.061$; Figure 18b). High d-excess values from evaporation are consistent with more diffusive transport of water molecules between the evaporating surface and the atmosphere. Our results that low RH and evaporation wind speed tend to produce higher d-excess values in precipitation are consistent with this theory, as lower wind speeds indicate reduced turbulent surface-atmosphere exchange. In contrast, low relative humidities amplify the gradient across which diffusion occurs. The similar magnitude, but opposite signs, of the d-excess sensitivity to changes in evaporation RH and temperature are consistent in direction, but only $\sim 35\%$ of the magnitude, of prior estimates (e.g., Pfahl & Sodemann, 2014). The lower sensitivity of d-excess to evaporative conditions in iCAM6 is a likely cause of the lower observed variance in precipitation d-excess relative to observations (Figures 5d–5f).

Spatial trends in the correlation between monthly precipitation d-excess and inferred conditions during evaporation suggest two distinct modes of variation. First, high precipitation d-excess is associated with low wind speeds in the tropics but high RH and temperature (Figure 19). In contrast, throughout much of the mid-latitudes, high precipitation d-excess is associated with high wind speeds but low RH (Figure 19). Modeled d-excess values are most sensitive to changes in wind speed (Figure 19f), but the range of variation in evaporation wind speeds ($\sim 4\text{--}12 \text{ m/s}$, or 8 m/s) is nearly an order of magnitude lower than the range in

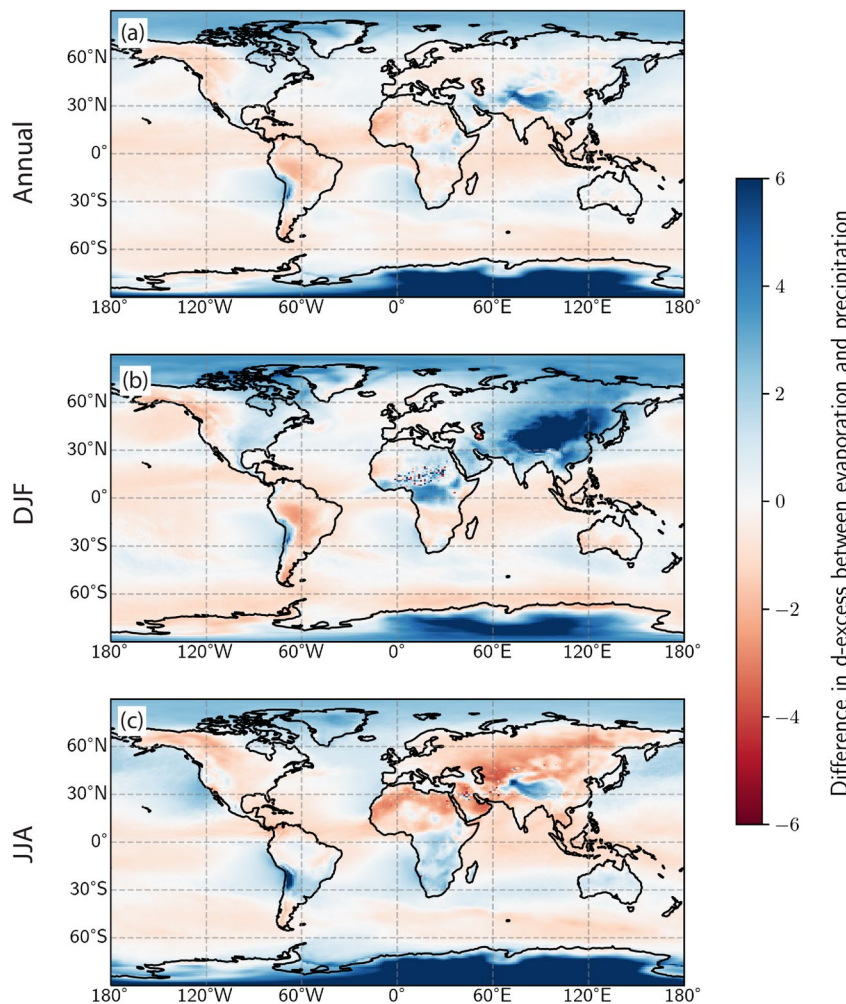


Figure 17. Differences in precipitation d-excess from the initial mean d-excess value of vapor (e.g., $d\text{-excess} - d\text{-excess}_0$). D-excess increases substantially between remote evaporation and condensation over high latitudes and high elevations, but changes are comparatively minor elsewhere.

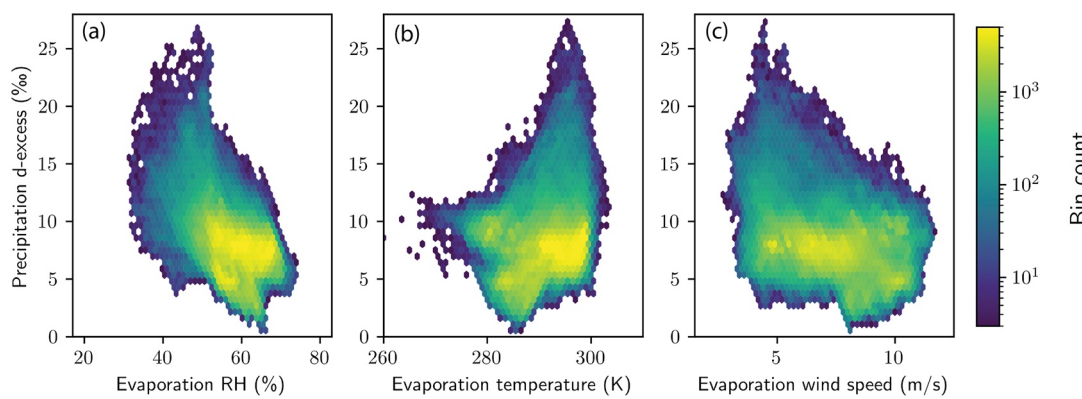


Figure 18. Relationships between precipitation d-excess and mean evaporation relative humidity (a, relative to skin temperature), evaporation temperature (b), or 10-m wind speed during evaporation (c).

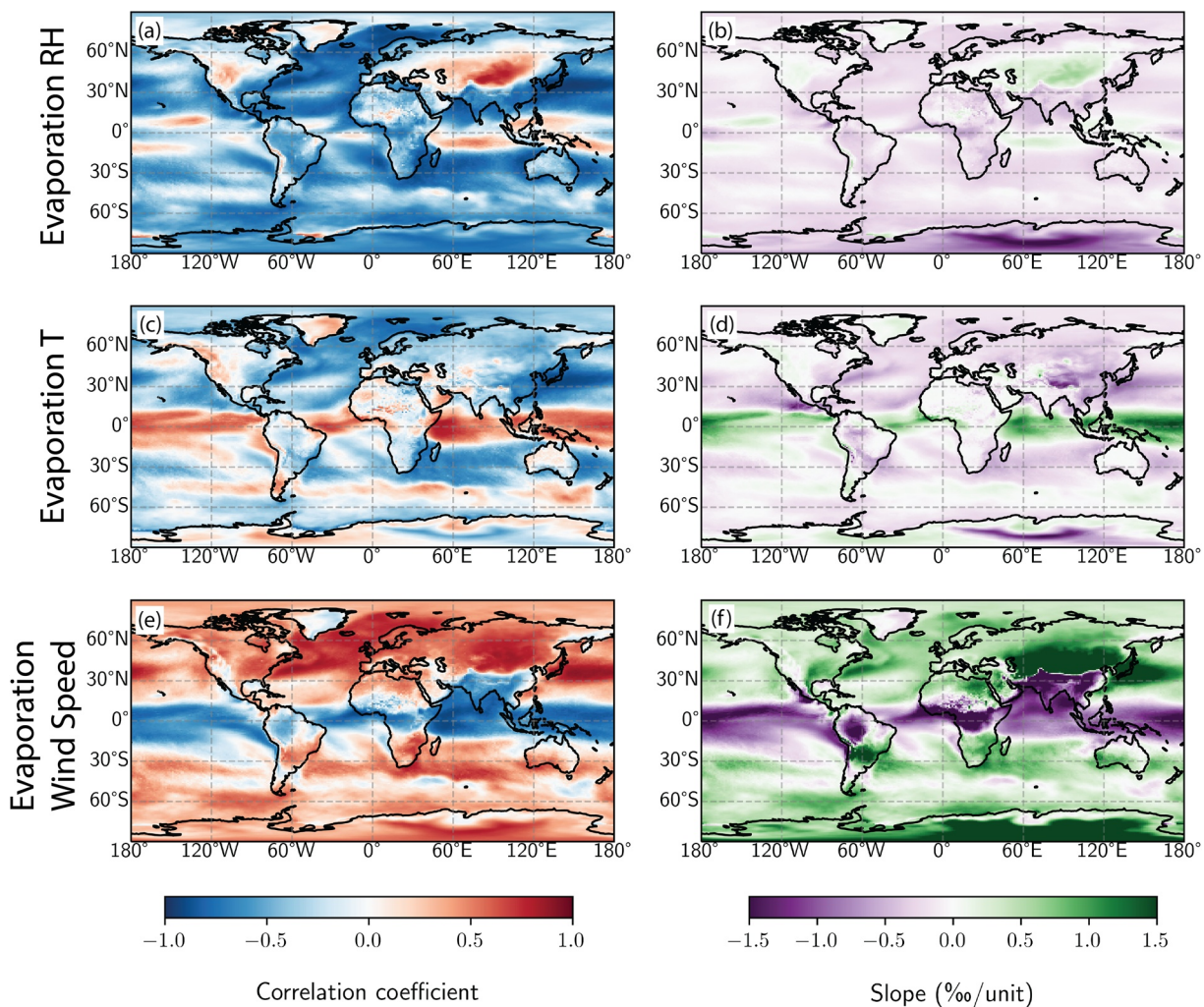


Figure 19. Correlation coefficients (left column; a, c, e) and regression slopes (right column; b, d, f) between monthly mean precipitation d-excess and (a and b) evaporation relative humidity, (c and d) evaporation temperature, and (e and f) 10-m wind speed during evaporation. Two distinct modes of variation are observed: in the tropics, high precipitation d-excess is associated with high temperature but low wind speed, whereas in the mid-latitudes, high d-excess occurs with low evaporation RH and temperature but high wind speed.

variation in evaporation RH (30%–70%, or 40%). Similar spatial patterns are observed when relationships between d-excess and evaporative conditions are considered on an inter-annual basis (Figure S2). As a result, we suspect that variations in precipitation d-excess strongly reflect variations in evaporation site RH, consistent with the conclusions of Pfahl and Sodemann (2014).

4.5. What Information Do Precipitation Isotope Ratios Contain?

In the preceding sections, we have demonstrated the utility of process-oriented tags to test hypotheses of what processes are responsible for variations in water isotope ratios. The relative importance of the multiple proposed drivers of isotope ratios can be compared using tagged quantities in random forest regression (Breiman, 2001). In this section, we examine the importance of several covariations to driving changes in monthly mean precipitation $\delta^{18}\text{O}$ and d-excess over land and the ocean globally and in the tropics, mid-latitudes, and high latitudes (Figures 20–23). Across all domains, $\ln(f)$ is the most important variable to explaining variations in precipitation $\delta^{18}\text{O}$ (Figures 20, 6–8). However, the importance of other variables such as condensation temperature, $\delta^{18}\text{O}_{\text{o}}$, precipitation amount, transport distance, and residence time varies across space, with different controls observed over land and the ocean. For example, condensation temperature is the second most important control on precipitation $\delta^{18}\text{O}$ globally (Figure 20a), at high latitudes

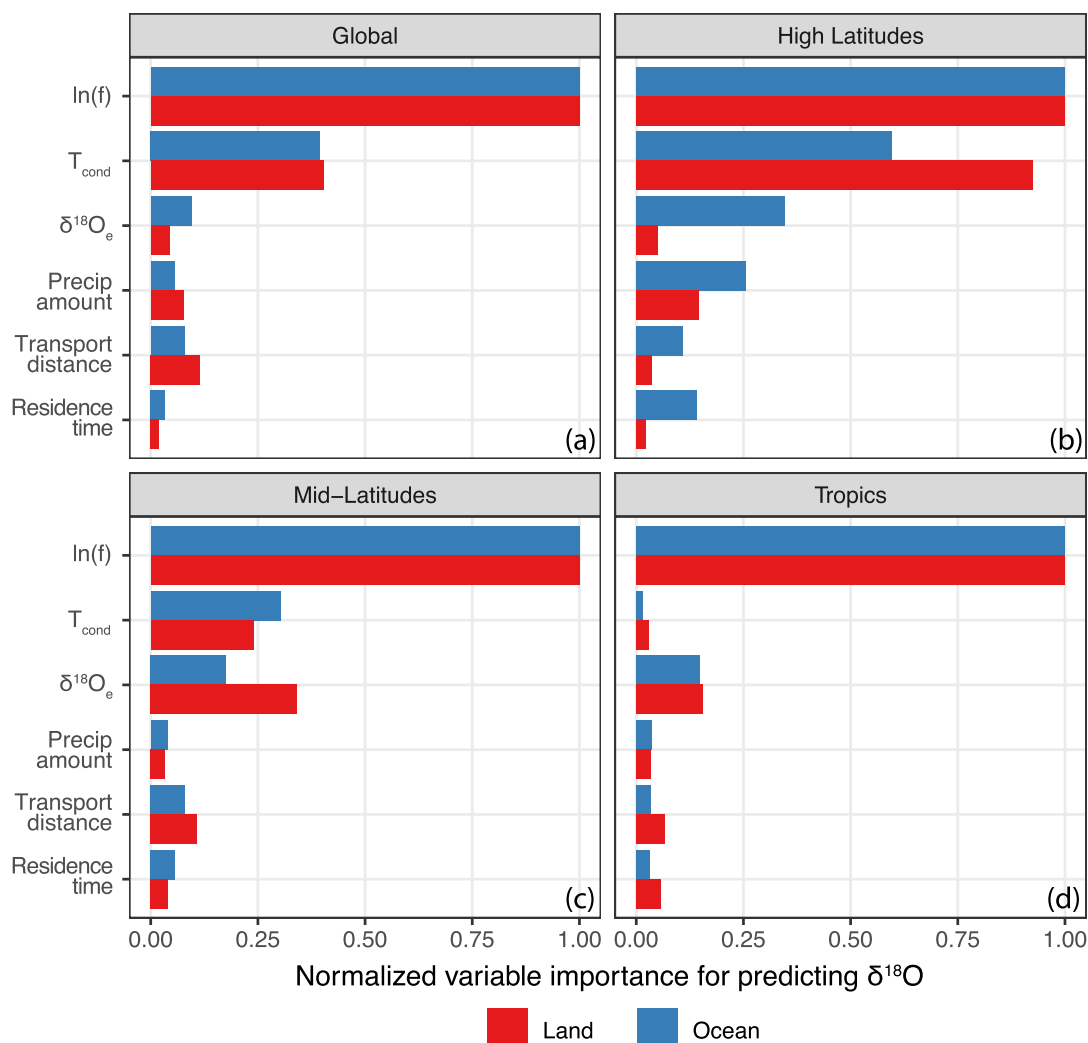


Figure 20. Normalized variable importance of candidate drivers of monthly mean precipitation $\delta^{18}\text{O}$ determined by random forest regression (a) globally, (b) for the high latitudes ($>60^\circ$ latitude), (c) for the mid-latitudes (between 30° and 60°), and for the tropics ($<30^\circ$ latitude). Models over land are shown as red bars, while models for the ocean are shown as blue bars.

(Figure 20b), and over mid-latitude oceans (Figure 20c), while $\delta^{18}\text{O}_0$ is the second strongest control over precipitation $\delta^{18}\text{O}$ in the tropics (Figure 20d) and over mid-latitude land (Figure 20c). Residence time and transport distance had <15% the normalized importance of $\ln(f)$ in all eight models (Figure 20). Land and ocean monthly mean precipitation $\delta^{18}\text{O}$ exhibited similar sensitivity to changes in $\ln(f)$ across all domains (Figures 21a–21d), as demonstrated by the similar slopes of the partial dependence curves. Precipitation $\delta^{18}\text{O}$ is most sensitive to changes in condensation temperature at low temperatures globally and at high-latitudes (Figures 21e and 21f), particularly over land. In contrast, precipitation $\delta^{18}\text{O}$ shows only a modest sensitivity to changes in condensation temperature in the mid-latitudes (Figure 21g) and is insensitive to changes in condensation temperature in the tropics (Figures 21h and 20d). Precipitation $\delta^{18}\text{O}$ is only mildly sensitive to changes in $\delta^{18}\text{O}_0$ globally (Figure 21i) but exhibits higher sensitivities to changes in $\delta^{18}\text{O}_0$ over high-latitude oceans (Figure 21j), and over land in the mid-latitudes and the ocean (Figures 21k and 21l). Interestingly, no model showed a strong partial dependence between precipitation rate and $\delta^{18}\text{O}$ (Figures 21m–21p), which affirms the suggestion of several studies that the “amount effect” (Dansgaard, 1964) is better understood as an integration of upwind hydrological processes rather than variations in local rainout (Cai & Tian, 2016; Dayem et al., 2010; Fiorella, Poulsen, Pillco Zolá, Barnes, et al., 2015).

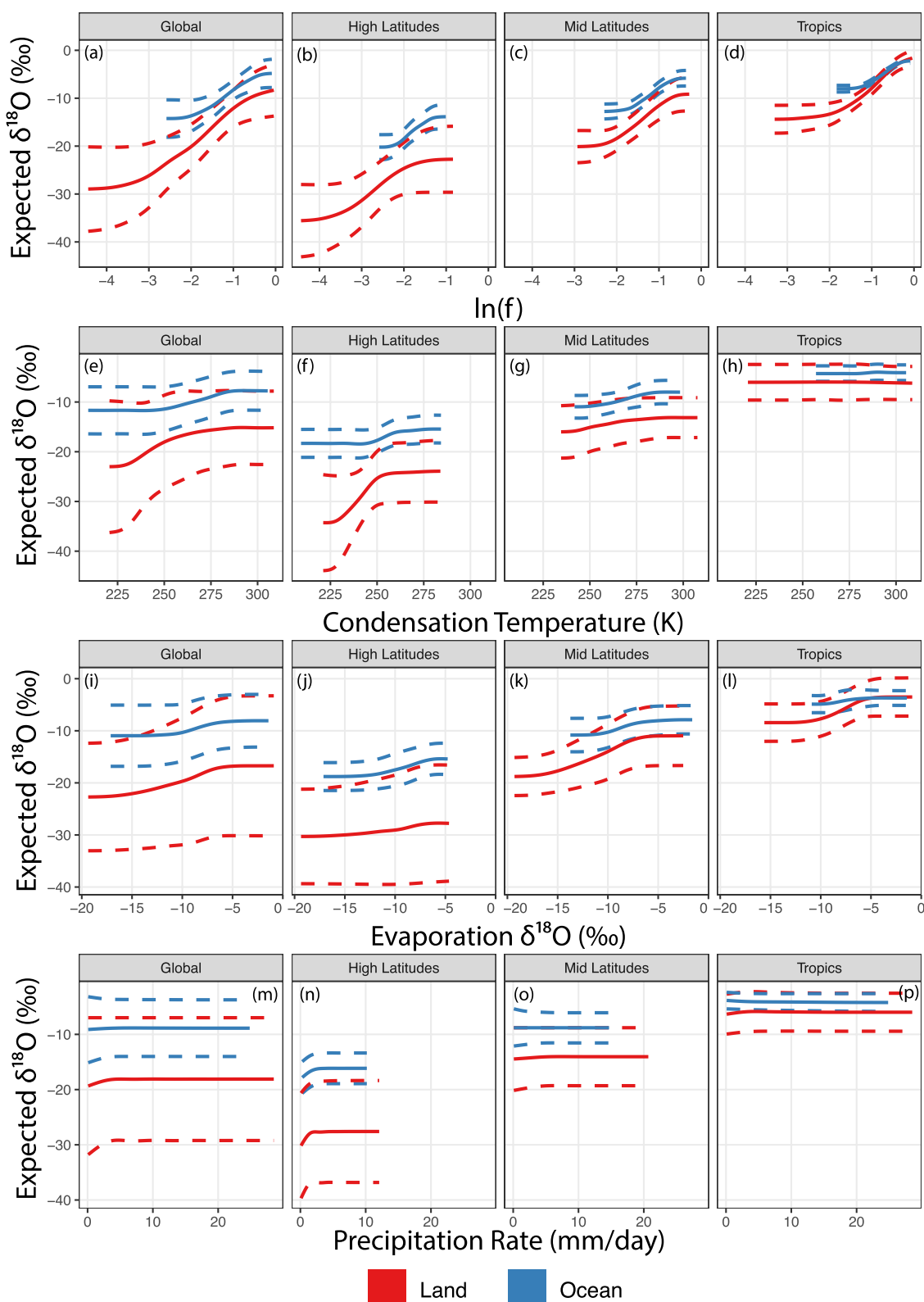


Figure 21. Partial dependence plots of monthly mean precipitation $\delta^{18}\text{O}$ with respect to (top row, a–d) $\ln(f)$, (second row, e–h) condensation temperature (K), (third row, i–l) $\delta^{18}\text{O}_o$, and (bottom row, m–p) precipitation rate (mm/day). Values over land are shown in red, while values over the ocean are shown in blue. Dashed lines indicate the 1-sigma range of individual conditional expectations (Goldstein et al., 2015) for each variable.

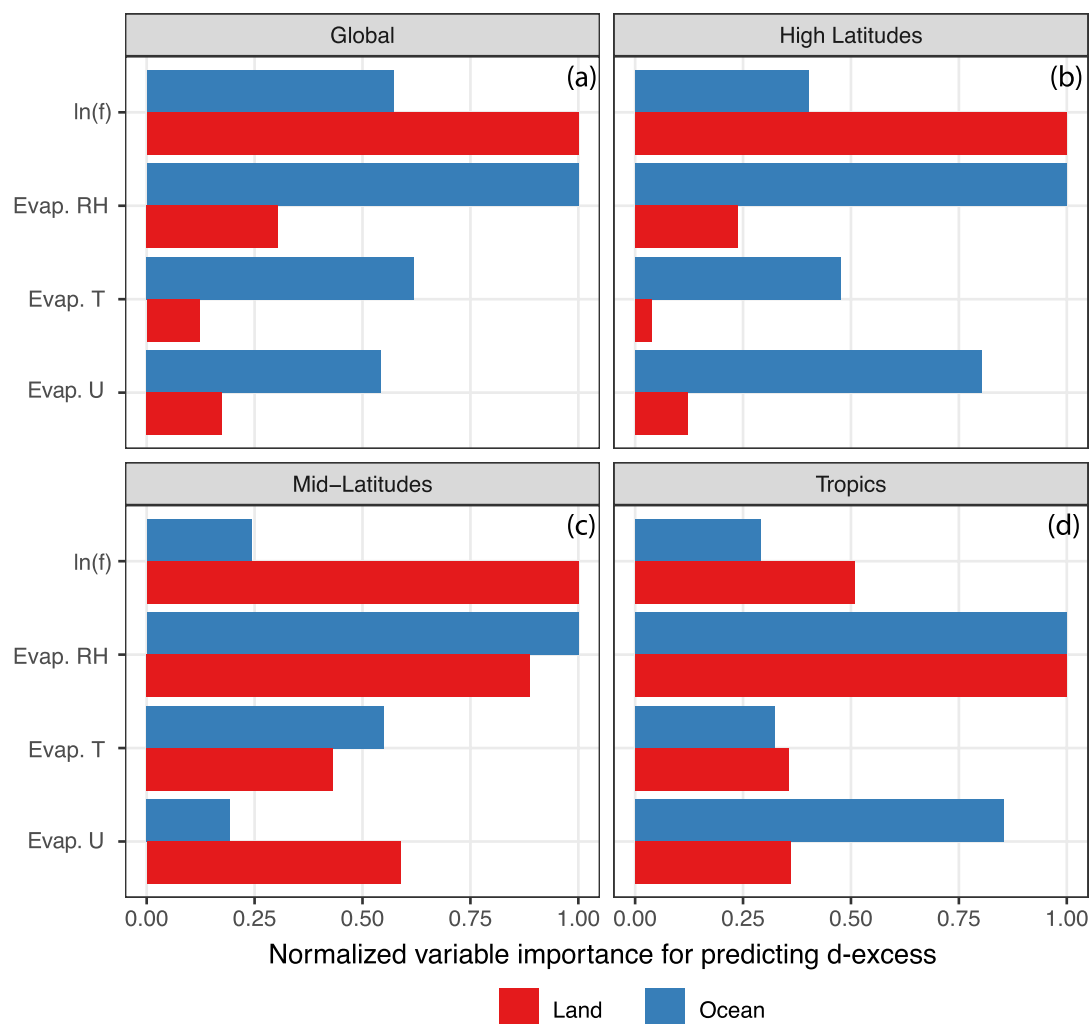


Figure 22. Normalized variable importance of candidate drivers of monthly mean precipitation d-excess determined by random forest regression (a) globally, (b) for the high latitudes ($>60^\circ$ latitude), (c) for the mid-latitudes (between 30° and 60°), and for the tropics ($<30^\circ$ latitude). Models over land are shown as red bars, while models for the ocean are shown as blue bars.

Globally, $\ln(f)$ remains the strongest predictor of monthly mean d-excess over land, but the relative humidity during evaporation expresses a stronger control on precipitation d-excess over the ocean (Figure 22a). Moreover, evaporation RH is the strongest control on monthly mean precipitation d-excess over the ocean at high, mid, and low-latitudes (Figures 22b–22d). Over land, $\ln(f)$ exerts the strongest control on monthly mean precipitation d-excess at high and mid-latitudes (Figures 22b and 22c) but is less important than evaporation RH in the tropics (Figure 22d). The rainout fraction ($\ln(f)$) and evaporation RH are the two most important variables in all cases over land, while the second most important control on precipitation d-excess over the ocean varies spatially. In the tropics and high-latitudes, evaporation wind speed is the second most important variable in determining precipitation d-excess (Figures 22b and 22d), while evaporation temperature is more important than wind speed in the mid-latitudes (Figure 22c). As discussed in Section 4.4 and Pfahl and Sodemann (2014), a likely explanation for this relationship is that spatiotemporal variations in evaporation RH are larger than spatiotemporal variations in wind speed. Monthly precipitation d-excess is most sensitive to changes in $\ln(f)$ at low values of $\ln(f)$ (Figures 23a–23d), which is consistent with the strong deviation from evaporation d-excess in precipitation at high-latitudes (Figure 17). Consistent with the variable importance analysis, sensitivities of d-excess to changes in $\ln(f)$ are higher over land than over the ocean (Figures 23a–23d). In contrast, sensitivity of precipitation d-excess to changes in evaporation RH are highest in the middle of the RH range (e.g., 45%–60%) in all domains, with similar

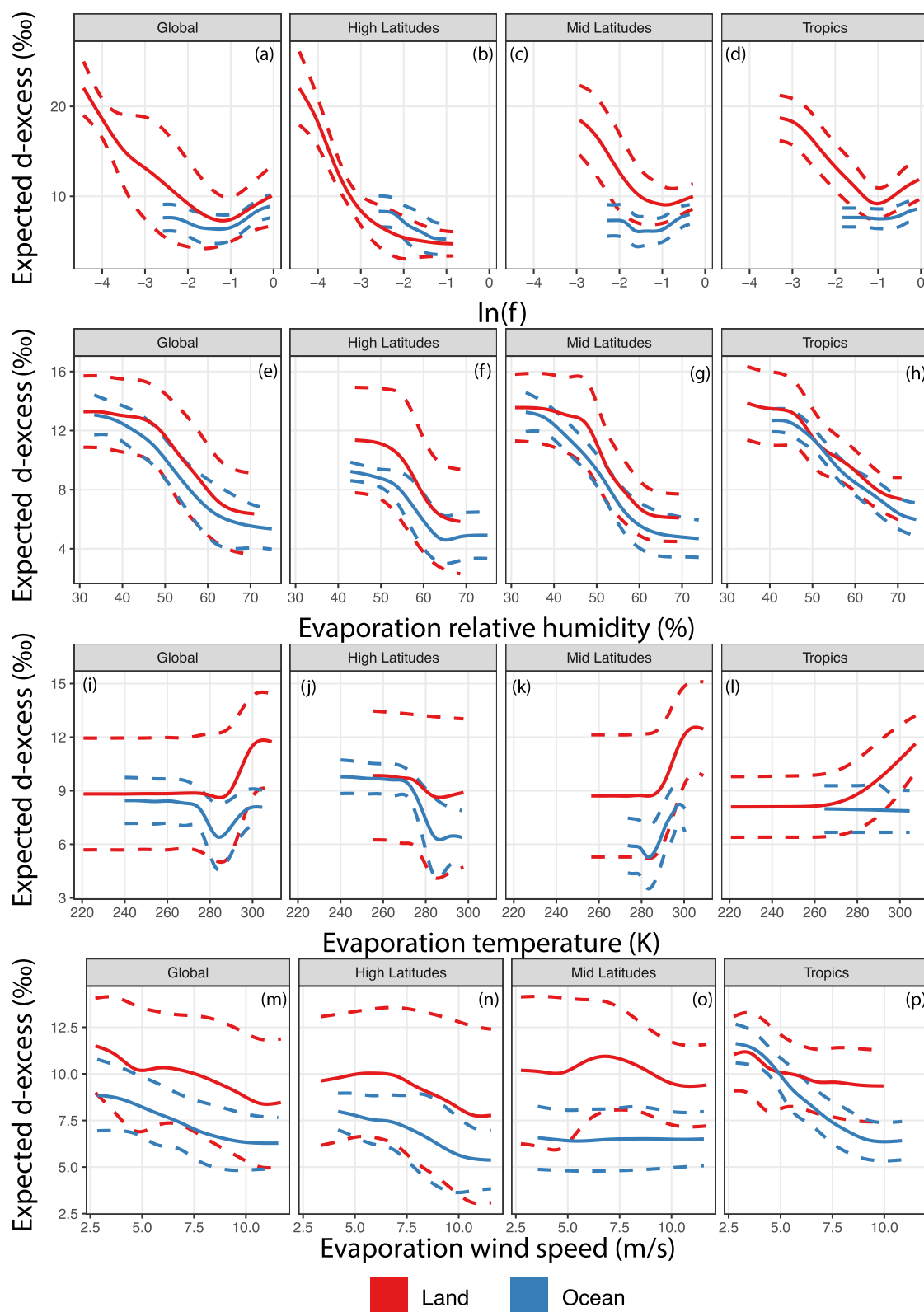


Figure 23. Partial dependence plots of monthly mean precipitation d-excess with respect to (top row, a–d) $\ln(f)$, (second row, e–h) evaporation relative humidity (%), (third row, i–l) evaporation temperature (K), and (bottom row, m–p) evaporation wind speed (m/s). Values over land are shown in red, while values over the ocean are shown in blue. Dashed lines indicate the 1-sigma range of individual conditional expectations (Goldstein et al., 2015) for each variable.

responses between land and ocean (Figures 23e–23h). Evaporation temperature has the largest influence on precipitation d-excess over land at high temperatures (Figure 23i), with expected d-excess values increasing with temperature. This effect is most evident in the mid- and low latitudes (Figures 23k and 23l). In contrast, precipitation d-excess over the ocean is largely insensitive to changes in evaporation temperature in the tropics (Figure 23l), increases with temperature in the mid-latitudes (Figure 23k), and decreases with temperature in the high latitudes (Figure 23j). Precipitation d-excess decreases with increasing evaporation wind speed, though with a lot of scatter over land (Figures 23m–23p). Sensitivity of precipitation d-excess to changes in wind speed are strongest over the high and low latitude oceans (Figures 23n and 23p), consistent with the variable importance analysis. Finally, in both cases, the isotopic impact of rain evaporation and re-equilibration below the cloud base cannot be captured with the tagged quantities in this study in our random forest model.

5. Conclusions

We have demonstrated the extensibility of the water-isotope-enabled branch of the Community Atmospheric Model to track a wide array of variables throughout the moist parameterizations of the model. We expand on prior work using water tracers in atmospheric models, which were often concerned with the relative importance of various evaporation regions, to cover a wide array of atmospheric variables and processes spanning the lifetime of atmospheric moisture from evaporation to precipitation. We demonstrate new tracer types designed to track properties during water evaporation and condensation or track integrated quantities, which show the mass-weighted mean temperature, relative humidity, and wind speed during evaporation, the mean temperature of condensation, and the integrated residence time and transport distance of atmospheric moisture. Additionally, we define a tracer approach to efficiently calculate the fraction of water removed from an air parcel (the Rayleigh “*f*”). Within the modeling context, these tags have resolved three common hypotheses in the water isotope literature: 1) that the fraction of vapor removed from an air parcel is the first-order control on precipitation isotope ratios, 2) that variations in precipitation isotope ratios can be related to variations in the residence time of atmospheric moisture, and 3) that precipitation d-excess reflects variations in meteorological or climatic conditions at the evaporative source. We find strong evidence supporting hypotheses 1 and 3 but little evidence supporting hypothesis 2. In the case of Hypothesis 2, it is worth recalling that the Raleigh model itself is agnostic to time, and the isotope changes are predicted based on a proportional change in the water abundance without concern for how long (or how far) a parcel has taken for that change to occur. Therefore, the resolution of hypothesis 2 indicates that the atmospheric hydrological cycle exhibits the property that the age of water in the atmosphere is not strongly coupled to the proportional change in water abundance along a transport path. Overall, iCAM6 exhibits an improved simulation of precipitation isotope ratios relative to iCAM5, particularly for low $\delta^{18}\text{O}$ values and a decrease in the error of d-excess relative to observations. However, iCAM6 still underestimates the observed variance in precipitation d-excess by a factor of 3, which points to potential limitations in the current treatment of kinetic processes in the hydrological cycle such as mixed-cloud microphysics, isotopic exchange between a falling raindrop and its environment, and evaporation from the land surface.

While we used process-oriented tags in this work to test theories explaining variations in modern water isotope ratios, these methods permit examination of a much broader range of hydrological cycle problems past, present, and future. For example, tracing evaporation and condensation temperatures allow for a detailed evaluation of energy transport and dissipation by the hydrological cycle and the extent to which moisture transport is isentropic (Bailey et al., 2019; Konings et al., 2012; Noone, 2008; Pauluis et al., 2008). Moreover, observations of isotope ratios are quite often proxies for another variable. In a paleoenvironmental context, isotope ratios of water and proxy materials forming from or in equilibrium with water provide constraints on past climate (Bird et al., 2020; Dayem et al., 2010; Jouzel, Lorius, et al., 1987; Libby et al., 1976; Vimeux et al., 2009), ecosystem dynamics (e.g., Fox et al., 2012; Gessler et al., 2014; Treydte et al., 2006), and/or elevation (e.g., Fiorella, Poulsen, Pillco Zolá, Jeffery, & Ehlers, 2015; Lechler & Galewsky, 2013; Poulsen & Jeffery, 2011; Rowley & Garzjone, 2007; Wheeler et al., 2016). Process-oriented tracers are a natural complement to proxy-system models that describe the incorporation of isotope signals into proxy archives (Bowen et al., 2020; Dee et al., 2015; Fischer-Femal & Bowen, 2021; McCarroll & Loader, 2004) by providing additional context about upwind processes driving variations in precipitation isotope ratios. Process-based

insights gleaned from these numerical tracers will enable more robust analyses of paleoproxy materials and a better understanding of the modern and future hydrological cycle.

Appendix A: Bucket Model Formulation

Precipitation is the only input to each bucket, and we make the simplifying assumption that the total precipitation amount from CAM adds water to both buckets at each time step since the distribution of soil moisture with depth is not passed from the land model to CAM. As a result, the two buckets do not strictly conserve mass but could instead act as capacitors with different time constants. If precipitation brings the water depth in each bucket above a maximum value (5 cm for the shallow upper bucket, 30 cm for the deep bucket), the excess water is removed from the bucket. The evaporative loss terms in each bucket are distinct and are calculated by breaking the net water flux passed CLM to CAM into constituent fluxes of transpiration, soil and lake evaporation, and the evaporation of canopy-intercepted water. Soil evaporation removes water from the shallow upper bucket, while fluxes due to transpiration, evaporation of canopy-intercepted water, and lake evaporation remove water from the deeper lower bucket. The transpiration and canopy interception evaporation fluxes are assumed to be isotopically non-fractionating. Plants generally do not strongly fractionate soil water during root water uptake (e.g., Ehleringer & Dawson, 1992; Zimmermann et al., 1967), and therefore we assume the transpiration flux does not fractionate water isotopologues. We assume that evaporation of canopy-intercepted water is complete, and therefore does not introduce an isotopic fractionation between the land surface and the atmosphere. Soil and lake evaporation fluxes are assumed to introduce an isotopic fractionation between the atmosphere and the land surface. The evaporative flux isotope ratio is calculated using the Craig and Gordon (1965) model when the lowest-model layer relative humidity was less than 98%:

$$R_E = \frac{\alpha_k \left(\frac{R_L}{\alpha_{eq}} - h R_A \right)}{1 - h} \quad (\text{A1})$$

where α_{eq} is the temperature-dependent equilibrium fractionation factor (Horita & Wesolowski, 1994), α_k is the kinetic fractionation factor, h is the relative humidity of the lowest model layer with respect to the model skin temperature, and R_E , R_A , and R_L are the heavy-to-light isotope ratios of the evaporative flux, the lowest-model level vapor, and the water in the bucket, respectively.

The kinetic fractionation parameter, α_k , was parameterized following Merlivat and Jouzel (1979) and as implemented in CAM by Nusbaumer et al. (2017). Briefly, the magnitude of kinetic fractionation is determined by the ratio of diffusivities between the heavy and light isotopologues, modified by boundary layer conditions to adjust for transitions between turbulent and diffusive transport:

$$\alpha_k = 1 - \frac{\left(\left(\frac{D}{D_i} \right)^n - 1 \right)}{\left(\left(\frac{D}{D_i} \right)^n + M \right)} \quad (\text{A2})$$

where D and D_i are the diffusivities of the dominant (e.g., $H_2^{16}O$) light isotopologue of water vapor and the rare heavy isotopologue (e.g., $^1H^2H^{16}O$, $H_2^{18}O$) respectively (Merlivat, 1978), n is a scaling constant, and M accounts for variations in the importance of turbulent and diffusive transport. Both the values of n and the formula for M depend on the Reynolds number Re :

$$Re = \frac{u_* z_0}{\mu} \quad (\text{A3})$$

where u_* is the friction velocity, z_0 is the roughness length, and μ is the kinematic viscosity of air. Both u_* and z_0 are calculated by the CLM and passed through the coupler to CAM. Where the Reynolds number is < 1 , n and M are parameterized to be consistent with diffusive transport:

$$n = \frac{2}{3}; M = \frac{\ln\left(\frac{u_* z_b}{30v}\right)}{13.6k \left(\frac{2}{Sc^{\frac{2}{3}}}\right)} \quad (A4)$$

where z_b is the height of the lowest model level, k is the von Kármán constant (0.4 in CESM), Sc is the Schmidt number ($Sc = \mu/D$), and v is a scaling factor accounting for variations in air density ($v = (1.7 \times 10^{-5})/\rho_a$). When the Reynolds number is ≥ 1 , different values of n and M are used to account for more turbulent transport:

$$n = \frac{1}{2}; M = \frac{\ln\left(\frac{z_b}{z_0} - 5\right)}{7.3k \left(Re^{0.25} (Sc)^{0.5}\right)} \quad (A5)$$

When the lowest model layer relative humidity was greater than 98%, the evaporative flux was assumed to be in isotopic equilibrium with the bucket water ($\alpha_k = 1$).

We also implemented a simple bucket model for water fluxes from sea ice to the atmosphere. Sea ice fluxes were assumed to be non-fractionating (e.g., Jouzel, Russell, et al., 1987; Lee et al., 2007). Isotope ratios were assumed to be equal to the isotope ratio of precipitation if the bucket is not empty (corresponding to snow on sea ice) and set to 0‰ (corresponding to seawater) if the bucket is empty.

Data Availability Statement

Computing and data storage resources, including the Cheyenne supercomputer (<https://doi.org/10.5065/D6RX99HX>), were provided by the Computational and Information Systems Laboratory (CISL) at NCAR. iCAM6 output used in this study is available from Dryad (<https://doi.org/10.5061/dryad.8w9ghx3mr>).

Acknowledgments

R. P. Fiorella received support from NSF Climate and Large-Scale Dynamics award 1954660. N. Siler received support from NSF Climate and Large-Scale Dynamics award 1954663. The CESM project is supported primarily by the National Science Foundation. This material is based upon work supported by the National Center for Atmospheric Research, a major facility sponsored by the National Science Foundation under Cooperative Agreement No. 1852977. NCAR is sponsored by the National Science Foundation. We thank all the scientists, software engineers, and administrators who contributed to the development of CESM2.

References

- Adler, R. F., Huffman, G. J., Chang, A., Ferraro, R., Xie, P.-P., Janowiak, J., et al. (2003). The Version-2 Global Precipitation Climatology Project (GPCP) monthly precipitation analysis (1979–present). *Journal of Hydrometeorology*, 4, 1147–1167. [https://doi.org/10.1175/1525-7541\(2003\)004<1147:tvgpcp>2.0.co;2](https://doi.org/10.1175/1525-7541(2003)004<1147:tvgpcp>2.0.co;2)
- Aemisegger, F., Pfahl, S., Sodemann, H., Lehner, I., Seneviratne, S. I., & Wernli, H. (2014). Deuterium excess as a proxy for continental moisture recycling and plant transpiration. *Atmospheric Chemistry and Physics*, 14(8), 4029–4054. <https://doi.org/10.5194/acp-14-4029-2014>
- Aggarwal, P. K., Alduchov, O. A., Froehlich, K. O., Araguas-Araguas, L. J., Sturchio, N. C., & Kurita, N. (2012). Stable isotopes in global precipitation: A unified interpretation based on atmospheric moisture residence time. *Geophysical Research Letters*, 39(11), L11705. <https://doi.org/10.1029/2012GL051937>
- Aggarwal, P. K., Romatschke, U., Araguas-Araguas, L., Belachew, D., Longstaffe, F. J., Berg, P., et al. (2016). Proportions of convective and stratiform precipitation revealed in water isotope ratios. *Nature Geoscience*, 9(8), 624–629. <https://doi.org/10.1038/ngeo2739>
- Aron, P. G., Levin, N. E., Beverly, E. J., Huth, T. E., Passey, B. H., Pelletier, E. M., et al. (2020). Triple oxygen isotopes in the water cycle. *Chemical Geology*, 565, 120026. <https://doi.org/10.1016/j.chemgeo.2020.120026>
- Aron, P. G., Poulsen, C. J., Fiorella, R. P., & Matheny, A. M. (2019). Stable water isotopes reveal effects of intermediate disturbance and canopy structure on forest water cycling. *Journal of Geophysical Research: Biogeosciences*, 124(10), 2958–2975. <https://doi.org/10.1029/2019JG005118>
- Bailey, A., Posmentier, E., & Feng, X. (2018). Patterns of evaporation and precipitation drive global isotopic changes in atmospheric moisture. *Geophysical Research Letters*, 45(14), 7093–7101. <https://doi.org/10.1029/2018GL078254>
- Bailey, A., Singh, H. K. A., & Nusbaumer, J. (2019). Evaluating a moist isentropic framework for poleward moisture transport: Implications for water isotopes over Antarctica. *Geophysical Research Letters*, 46(13), 7819–7827. <https://doi.org/10.1029/2019GL082965>
- Bailey, A., Toohey, D., & Noone, D. (2013). Characterizing moisture exchange between the Hawaiian convective boundary layer and free troposphere using stable isotopes in water. *Journal of Geophysical Research: Atmospheres*, 118(15), 8208–8221. <https://doi.org/10.1002/jgrd.50639>
- Barbour, M. M., Roden, J. S., Farquhar, G. D., & Ehleringer, J. R. (2004). Expressing leaf water and cellulose oxygen isotope ratios as enrichment above source water reveals evidence of a Pécelt effect. *Oecologia*, 138(3), 426–435. <https://doi.org/10.1007/s00442-003-1449-3>
- Benetti, M., Reverdin, G., Pierre, C., Merlivat, L., Risi, C., Steen-Larsen, H. C., & Vimeux, F. (2014). Deuterium excess in marine water vapor: Dependency on relative humidity and surface wind speed during evaporation. *Journal of Geophysical Research: Atmospheres*, 119(2), 584–593. <https://doi.org/10.1002/2013JD020535>
- Bigeleisen, J. (1965). Chemistry of isotopes. *Science*, 147(3657), 463–471. <https://doi.org/10.1126/science.147.3657.463>
- Bigeleisen, J., & Wolfsberg, M. (1958). Theoretical and experimental aspects of isotope effects in chemical kinetics. In I. Prigogine, & P. Debye (Eds.), *Advances in chemical physics* (pp. 15–76). Hoboken, NJ, USA: John Wiley & Sons, Inc. <https://doi.org/10.1002/9780470143476.ch2>
- Bird, M. I., Haig, J., Hadeen, X., Rivera-Araya, M., Wurster, C. M., & Zwart, C. (2020). Stable isotope proxy records in tropical terrestrial environments. *Palaeogeography, Palaeoclimatology, Palaeoecology*, 538, 109445. <https://doi.org/10.1016/j.palaeo.2019.109445>

- Blossey, P. N., Kuang, Z., & Romps, D. M. (2010). Isotopic composition of water in the tropical tropopause layer in cloud-resolving simulations of an idealized tropical circulation. *Journal of Geophysical Research*, 115(D24), D24309. <https://doi.org/10.1029/2010JD014554>
- Bogenshutz, P. A., Gettelman, A., Hannay, C., Larson, V. E., Neale, R. B., Craig, C., & Chen, C.-C. (2018). The path to CAM6: Coupled simulations with CAM5.4 and CAM5.5. *Geoscientific Model Development*, 11(1), 235–255. <https://doi.org/10.5194/gmd-11-235-2018>
- Bogenshutz, P. A., Gettelman, A., Morrison, H., Larson, V. E., Schanen, D. P., Meyer, N. R., & Craig, C. (2012). Unified parameterization of the planetary boundary layer and shallow convection with a higher-order turbulence closure in the Community Atmosphere Model: Single-column experiments. *Geoscientific Model Development*, 5(6), 1407–1423. <https://doi.org/10.5194/gmd-5-1407-2012>
- Bony, S., Risi, C., & Vimeux, F. (2008). Influence of convective processes on the isotopic composition ($\delta^{18}\text{O}$ and δD) of precipitation and water vapor in the tropics: 1. Radiative-convective equilibrium and Tropical Ocean–Global Atmosphere–Coupled Ocean–Atmosphere Response Experiment (TOGA-COARE) simulations. *Journal of Geophysical Research*, 113(D19), D19305. <https://doi.org/10.1029/2008JD009942>
- Bosilovich, M. G. (2002). On the vertical distribution of local and remote sources of water for precipitation. *Meteorology and Atmospheric Physics*, 80(1–4), 31–41. <https://doi.org/10.1007/s007030200012>
- Bowen, G. J., Cai, Z., Fiorella, R. P., & Putman, A. L. (2019). Isotopes in the water cycle: Regional- to global-scale patterns and applications. *Annual Review of Earth and Planetary Sciences*, 47, 453–479. <https://doi.org/10.1146/annurev-earth-053018-060220>
- Bowen, G. J., Fischer-Femal, B., Reichart, G.-J., Sluijs, A., & Lear, C. H. (2020). Joint inversion of proxy system models to reconstruct paleoenvironmental time series from heterogeneous data. *Climate of the Past*, 16(1), 65–78. <https://doi.org/10.5194/cp-16-65-2020>
- Bowen, G. J., Kennedy, C. D., Henne, P. D., & Zhang, T. (2012). Footprint of recycled water subsidies downwind of Lake Michigan. *Ecosphere*, 3(6), 53. <https://doi.org/10.1890/ES12-0062.1>
- Brady, E., Stevenson, S., Bailey, D., Liu, Z., Noone, D., Nusbaumer, J., et al. (2019). The connected isotopic water cycle in the community earth system model version 1. *Journal of Advances in Modeling Earth Systems*, 11(8), 2547–2566. <https://doi.org/10.1029/2019MS001663>
- Breiman, L. (2001). Random forests. *Machine Learning*, 45, 5–32. <https://doi.org/10.1023/a:1010933404324>
- Cai, Z., & Tian, L. (2016). Atmospheric controls on seasonal and interannual variations in the precipitation isotope in the East Asian monsoon region. *Journal of Climate*, 29(4), 1339–1352. <https://doi.org/10.1175/JCLI-D-15-0363.1>
- Cernusak, L. A., Barbour, M. M., Arndt, S. K., Cheesman, A. W., English, N. B., Feild, T. S., et al. (2016). Stable isotopes in leaf water of terrestrial plants. *Plant, Cell & Environment*, 39(5), 1087–1102. <https://doi.org/10.1111/pce.12703>
- Ciais, P., & Jouzel, J. (1994). Deuterium and oxygen 18 in precipitation: Isotopic model, including mixed cloud processes. *Journal of Geophysical Research*, 99(D8), 16793. <https://doi.org/10.1029/94JD00412>
- Conroy, J. L., Noone, D., Cobb, K. M., Moerman, J. W., & Konecky, B. L. (2016). Paired stable isotopologues in precipitation and vapor: A case study of the amount effect within western tropical Pacific storms: Isotopes in Western Pacific Storms. *Journal of Geophysical Research: Atmospheres*, 121(7), 3290–3303. <https://doi.org/10.1002/2015JD023844>
- Craig, H., & Gordon, L. I. (1965). Deuterium and oxygen-18 variations in the ocean and the marine atmosphere. In *Stable isotopes in oceanographic studies and paleotemperatures*.
- Danabasoglu, G., Lamarque, J.-F., Bacmeister, J., Bailey, D. A., DuVivier, A. K., Edwards, J., et al. (2020). The Community Earth System Model Version 2 (CESM2). *Journal of Advances in Modeling Earth Systems*, 12(2), e2019MS001916. <https://doi.org/10.1029/2019MS001916>
- Dansgaard, W. (1964). Stable isotopes in precipitation. *Tellus*, 16(4), 436–468. <https://doi.org/10.1111/j.2153-3490.1964.tb00181.x>
- Dayem, K. E., Molnar, P., Battisti, D. S., & Roe, G. H. (2010). Lessons learned from oxygen isotopes in modern precipitation applied to interpretation of speleothem records of paleoclimate from eastern Asia. *Earth and Planetary Science Letters*, 295(1–2), 219–230. <https://doi.org/10.1016/j.epsl.2010.04.003>
- Dee, S., Emile-Geay, J., Evans, M. N., Allam, A., Steig, E. J., & Thompson, D. M. (2015). PRYSM: An open-source framework for PRoxy System Modeling, with applications to oxygen-isotope systems. *Journal of Advances in Modeling Earth Systems*, 7(3), 1220–1247. <https://doi.org/10.1002/2015MS000447>
- Dominguez, F., Miguez-Macho, G., & Hu, H. (2016). WRF with water vapor tracers: A study of moisture sources for the North American Monsoon. *Journal of Hydrometeorology*, 17(7), 1915–1927. <https://doi.org/10.1175/JHM-D-15-0221.1>
- Dütsch, M., Blossey, P. N., Steig, E. J., & Nusbaumer, J. M. (2019). Nonequilibrium fractionation during ice cloud formation in iCAM5: Evaluating the common parameterization of supersaturation as a linear function of temperature. *Journal of Advances in Modeling Earth Systems*, 11(11), 3777–3793. <https://doi.org/10.1029/2019MS001764>
- Dutton, A., Wilkinson, B. H., Welker, J. M., Bowen, G. J., & Lohmann, K. C. (2005). Spatial distribution and seasonal variation in $^{18}\text{O}/^{16}\text{O}$ of modern precipitation and river water across the conterminous USA. *Hydrological Processes*, 19(20), 4121–4146. <https://doi.org/10.1002/hyp.5876>
- Dyer, E. L. E., Jones, D. B. A., Nusbaumer, J., Li, H., Collins, O., Vettoretti, G., & Noone, D. (2017). Congo Basin precipitation: Assessing seasonality, regional interactions, and sources of moisture. *Journal of Geophysical Research: Atmospheres*, 122(13), 6882–6898. <https://doi.org/10.1002/2016JD026240>
- Ehlneringer, J. R., & Dawson, T. E. (1992). Water uptake by plants: Perspectives from stable isotope composition. *Plant, Cell and Environment*, 15(9), 1073–1082. <https://doi.org/10.1111/j.1365-3040.1992.tb01657.x>
- Eriksson, E. (1965). Deuterium and oxygen-18 in precipitation and other natural waters Some theoretical considerations. *Tellus*, 17(4), 498–512. <https://doi.org/10.1111/j.2153-3490.1965.tb00212.x>
- Farquhar, G. D., Cernusak, L. A., & Barnes, B. (2007). Heavy water fractionation during transpiration. *Plant Physiology*, 143(1), 11–18. <https://doi.org/10.1104/pp.106.093278>
- Fiorella, R. P., Barres, R., Lin, J. C., & Bowen, G. J. (2019). Wintertime decoupling of urban valley and rural ridge hydrological processes revealed through stable water isotopes. *Atmospheric Environment*, 213, 337–348. <https://doi.org/10.1016/j.atmosenv.2019.06.022>
- Fiorella, R. P., Poulsen, C. J., & Matheny, A. M. (2018). Seasonal patterns of water cycling in a deep, continental mountain valley inferred from stable water vapor isotopes. *Journal of Geophysical Research: Atmospheres*, 123, 7271–7291. <https://doi.org/10.1029/2017JD028093>
- Fiorella, R. P., Poulsen, C. J., Pillco Zolá, R. S., Barnes, J. B., Tabor, C. R., & Ehlers, T. A. (2015). Spatiotemporal variability of modern precipitation $\delta^{18}\text{O}$ in the central Andes and implications for paleoclimate and paleoaltimetry estimates. *Journal of Geophysical Research: Atmospheres*, 120(10), 4630–4656. <https://doi.org/10.1002/2014JD022893>
- Fiorella, R. P., Poulsen, C. J., Pillco Zolá, R. S., Jeffery, M. L., & Ehlers, T. A. (2015). Modern and long-term evaporation of central Andes surface waters suggests paleo archives underestimate Neogene elevations. *Earth and Planetary Science Letters*, 432, 59–72. <https://doi.org/10.1016/j.epsl.2015.09.045>
- Fiorella, R. P., West, J. B., & Bowen, G. J. (2019). Biased estimates of the isotope ratios of steady-state evaporation from the assumption of equilibrium between vapour and precipitation. *Hydrological Processes*, 33(19), 2576–2590. <https://doi.org/10.1002/hyp.13531>

- Fischer-Femal, B. J., & Bowen, G. J. (2021). Coupled carbon and oxygen isotope model for pedogenic carbonates. *Geochimica et Cosmochimica Acta*, 294, 126–144. <https://doi.org/10.1016/j.gca.2020.10.022>
- Fox, D. L., Honey, J. G., Martin, R. A., & Pelaez-Campomanes, P. (2012). Pedogenic carbonate stable isotope record of environmental change during the Neogene in the southern Great Plains, southwest Kansas, USA: Oxygen isotopes and paleoclimate during the evolution of C4-dominated grasslands. *Geological Society of America Bulletin*, 124(3–4), 431–443. <https://doi.org/10.1130/B30402.1>
- Froehlich, K., Kralik, M., Papesch, W., Rank, D., Scheifinger, H., & Stichler, W. (2008). Deuterium excess in precipitation of Alpine regions – Moisture recycling. *Isotopes in Environmental and Health Studies*, 44(1), 61–70. <https://doi.org/10.1080/10256010801887208>
- Galewsky, J., Steen-Larsen, H. C., Field, R. D., Worden, J., Risi, C., & Schneider, M. (2016). Stable isotopes in atmospheric water vapor and applications to the hydrologic cycle. *Reviews of Geophysics*, 54(4), 809–865. <https://doi.org/10.1002/2015RG000512>
- Gat, J. R. (1996). Oxygen and hydrogen isotopes in the hydrologic cycle. *Annual Review of Earth and Planetary Sciences*, 24, 225–262. <https://doi.org/10.1146/annurev.earth.24.1.225>
- Gessler, A., Ferrio, J. P., Hommel, R., Treydte, K., Werner, R. A., & Monson, R. K. (2014). Stable isotopes in tree rings: Towards a mechanistic understanding of isotope fractionation and mixing processes from the leaves to the wood. *Tree Physiology*, 34(8), 796–818. <https://doi.org/10.1093/treephys/tpu040>
- Gettelman, A., & Morrison, H. (2015). Advanced two-moment bulk microphysics for global models. Part I: Off-line tests and comparison with other schemes. *Journal of Climate*, 28(3), 1268–1287. <https://doi.org/10.1175/JCLI-D-14-00102.1>
- Gettelman, A., Morrison, H., Santos, S., Bogenschutz, P., & Caldwell, P. M. (2015). Advanced two-moment bulk microphysics for global models. Part II: Global model solutions and aerosol–cloud interactions. *Journal of Climate*, 28(3), 1288–1307. <https://doi.org/10.1175/JCLI-D-14-00103.1>
- Gimeno, L., Nieto, R., Trigo, R. M., Vicente-Serrano, S. M., & López-Moreno, J. I. (2010). Where does the Iberian Peninsula moisture come from? An answer based on a lagrangian approach. *Journal of Hydrometeorology*, 11(2), 421–436. <https://doi.org/10.1175/2009JHM1182.1>
- Goldstein, A., Kapelner, A., Bleich, J., & Pitkin, E. (2015). Peeking Inside the black box: Visualizing statistical learning with plots of individual conditional expectation. *Journal of Computational and Graphical Statistics*, 24(1), 44–65. <https://doi.org/10.1080/10618600.2014.907095>
- Good, S. P., Noone, D., & Bowen, G. (2015). Hydrologic connectivity constrains partitioning of global terrestrial water fluxes. *Science*, 349(6244), 175–177. <https://doi.org/10.1126/science.aaa5931>
- Haese, B., Werner, M., & Lohmann, G. (2013). Stable water isotopes in the coupled atmosphere–land surface model ECHAM5-JSBACH. *Geoscientific Model Development*, 6(5), 1463–1480. <https://doi.org/10.5194/gmd-6-1463-2013>
- Held, I. M., & Soden, B. J. (2000). Water vapor feedback and global warming. *Annual Review of Energy and the Environment*, 25, 441–475. <https://doi.org/10.1146/annurev.energy.25.1.441>
- Held, I. M., & Soden, B. J. (2006). Robust responses of the hydrological cycle to global warming. *Journal of Climate*, 19(21), 5686–5699. <https://doi.org/10.1175/JCLI3990.1>
- Hersbach, H., Bell, B., Berrisford, P., Hirahara, S., Horányi, A., Muñoz-Sabater, J., et al. (2020). The ERA5 global reanalysis. *Quarterly Journal of the Royal Meteorological Society*, 146(730), 1999–2049. <https://doi.org/10.1002/qj.3803>
- Hoffmann, G., Werner, M., & Heimann, M. (1998). Water isotope module of the ECHAM atmospheric general circulation model: A study on timescales from days to several years. *Journal of Geophysical Research*, 103(D14), 16871–16896. <https://doi.org/10.1029/98JD00423>
- Horita, J., & Wesolowski, D. J. (1994). Liquid-vapor fractionation of oxygen and hydrogen isotopes of water from the freezing to the critical temperature. *Geochimica et Cosmochimica Acta*, 58(16), 3425–3437. [https://doi.org/10.1016/0016-7037\(94\)90096-5](https://doi.org/10.1016/0016-7037(94)90096-5)
- Hoyer, S., & Hamman, J. J. (2017). xarray: N-D labeled Arrays and Datasets in Python. *Journal of Open Research Software*, 5, 10. <https://doi.org/10.5334/jors.148>
- Hu, H., & Dominguez, F. (2015). Evaluation of oceanic and terrestrial sources of moisture for the North American Monsoon using numerical models and precipitation stable isotopes. *Journal of Hydrometeorology*, 16(1), 19–35. <https://doi.org/10.1175/JHM-D-14-0073.1>
- Humphrey, V., Zscheischler, J., Ciais, P., Gudmundsson, L., Sitch, S., & Seneviratne, S. I. (2018). Sensitivity of atmospheric CO₂ growth rate to observed changes in terrestrial water storage. *Nature*, 560(7720), 628–631. <https://doi.org/10.1038/s41586-018-0424-4>
- Hunter, J. D. (2007). Matplotlib: A 2d graphics environment. *Computing in Science & Engineering*, 9(3), 90–95. <https://doi.org/10.1109/mcse.2007.55>
- Hwang, Y.-T., & Frierson, D. M. W. (2010). Increasing atmospheric poleward energy transport with global warming. *Geophysical Research Letters*, 37(24), L24807. <https://doi.org/10.1029/2010GL045440>
- IAEA/WMO (2021). Global network of isotopes in precipitation. The GNIP Database. Retrieved from <https://nucleus.iaea.org/wiser>
- Johnsen, S. J., Dansgaard, W., & White, J. W. C. (1989). The origin of Arctic precipitation under present and glacial conditions. *Tellus B: Chemical and Physical Meteorology*, 41B(4), 452–468. <https://doi.org/10.1111/j.1600-0889.1989.tb00321.x>
- Jones, P. W. (1999). First- and second-order conservative remapping schemes for grids in spherical coordinates. *Monthly Weather Review*, 127(9), 2204–2210. [https://doi.org/10.1175/1520-0493\(1999\)127<2204:FASOCR>2.0.CO;2](https://doi.org/10.1175/1520-0493(1999)127<2204:FASOCR>2.0.CO;2)
- Joussaume, S., Sadourny, R., & Jouzel, J. (1984). A general circulation model of water isotope cycles in the atmosphere. *Nature*, 311(5981), 24–29. <https://doi.org/10.1038/311024a0>
- Jouzel, J., Alley, R. B., Cuffey, K. M., Dansgaard, W., Grootes, P., Hoffmann, G., et al. (1997). Validity of the temperature reconstruction from water isotopes in ice cores. *Journal of Geophysical Research*, 102(C12), 26471–26487. <https://doi.org/10.1029/97JC01283>
- Jouzel, J., Lorius, C., Petit, J. R., Genthon, C., Barkov, N. I., Kotlyakov, V. M., & Petrov, V. M. (1987). Vostok ice core: A continuous isotope temperature record over the last climatic cycle (160,000 years). *Nature*, 329(6138), 403–408. <https://doi.org/10.1038/329403a0>
- Jouzel, J., & Merlivat, L. (1984). Deuterium and oxygen 18 in precipitation: Modeling of the isotopic effects during snow formation. *Journal of Geophysical Research*, 89(D7), 11749. <https://doi.org/10.1029/JD089iD07p11749>
- Jouzel, J., Merlivat, L., & Lorius, C. (1982). Deuterium excess in an East Antarctic ice core suggests higher relative humidity at the oceanic surface during the last glacial maximum. *Nature*, 299(5885), 688–691. <https://doi.org/10.1038/299688a0>
- Jouzel, J., Russell, G. L., Suozzo, R. J., Koster, R. D., White, J. W. C., & Broecker, W. S. (1987). Simulations of the HDO and H₂O atmospheric cycles using the NASA GISS general circulation model: The seasonal cycle for present-day conditions. *Journal of Geophysical Research*, 92(D12), 14739–14760. <https://doi.org/10.1029/JD092iD12p14739>
- Kannenberg, S. A., Fiorella, R. P., Anderegg, W. R. L., Monson, R. K., & Ehleringer, J. R. (2021). Seasonal and diurnal trends in progressive isotope enrichment along needles in two pine species. *Plant, Cell & Environment*, 44, 143–155. <https://doi.org/10.1111/pce.13915>
- Kay, J. E., Wall, C., Yettella, V., Medeiros, B., Hannay, C., Caldwell, P., & Bitz, C. (2016). Global climate impacts of fixing the Southern Ocean shortwave radiation bias in the Community Earth System Model (CESM). *Journal of Climate*, 29(12), 4617–4636. <https://doi.org/10.1175/JCLI-D-15-0358.1>
- Kelley, M. J. (2003). *Water tracers and the hydrologic cycle in a GCM*. New York, N. Y: Columbia University.

- Kleidon, A., & Renner, M. (2013). Thermodynamic limits of hydrologic cycling within the Earth system: Concepts, estimates and implications. *Hydrology and Earth System Sciences*, 17(7), 2873–2892. <https://doi.org/10.5194/hess-17-2873-2013>
- Knoche, H. R., & Kunstmann, H. (2013). Tracking atmospheric water pathways by direct evaporation tagging: A case study for West Africa. *Journal of Geophysical Research: Atmospheres*, 118(22), 12345–12358. <https://doi.org/10.1002/2013JD019976>
- Kohn, M. J., & Welker, J. M. (2005). On the temperature correlation of $\delta^{18}\text{O}$ in modern precipitation. *Earth and Planetary Science Letters*, 231(1–2), 87–96. <https://doi.org/10.1016/j.epsl.2004.12.004>
- Konecky, B. L., Noone, D. C., & Cobb, K. M. (2019). The influence of competing hydroclimate processes on stable isotope ratios in tropical rainfall. *Geophysical Research Letters*, 46(3), 1622–1633. <https://doi.org/10.1029/2018GL080188>
- Konings, A. G., Feng, X., Molini, A., Manzoni, S., Vico, G., & Porporato, A. (2012). Thermodynamics of an idealized hydrologic cycle. *Water Resources Research*, 48(5), W05527. <https://doi.org/10.1029/2011WR011264>
- Koster, R., Jouzel, J., Suozzo, R., Russell, G., Broecker, W., Rind, D., & Eagleson, P. (1986). Global sources of local precipitation as determined by the NASA/GISS GCM. *Geophysical Research Letters*, 13(2), 121–124. <https://doi.org/10.1029/GL013i002p00121>
- Kurita, N., Yoshida, N., Inoue, G., & Chayanova, E. A. (2004). Modern isotope climatology of Russia: A first assessment. *Journal of Geophysical Research*, 109, D03102. <https://doi.org/10.1029/2003JD003404>
- Läderach, A., & Sodemann, H. (2016). A revised picture of the atmospheric moisture residence time. *Geophysical Research Letters*, 43(2), 924–933. <https://doi.org/10.1002/2015GL067449>
- Lai, C.-T., & Ehleringer, J. R. (2011). Deuterium excess reveals diurnal sources of water vapor in forest air. *Oecologia*, 165(1), 213–223. <https://doi.org/10.1007/s00442-010-1721-2>
- Lawrence, D. M., Fisher, R. A., Koven, C. D., Oleson, K. W., Swenson, S. C., Bonan, G., et al. (2019). The Community Land Model Version 5: Description of new features, benchmarking, and impact of forcing uncertainty. *Journal of Advances in Modeling Earth Systems*, 11(12), 4245–4287. <https://doi.org/10.1029/2018MS001583>
- Lechler, A. R., & Galewsky, J. (2013). Refining paleoaltimetry reconstructions of the Sierra Nevada, California, using air parcel trajectories. *Geology*, 41(2), 259–262. <https://doi.org/10.1130/G33553.1>
- L'Ecuyer, T. S., Beaudoing, H. K., Rodell, M., Olson, W., Lin, B., Kato, S., et al. (2015). The observed state of the energy budget in the early twenty-first century. *Journal of Climate*, 28(21), 8319–8346. <https://doi.org/10.1175/JCLI-D-14-00556.1>
- Lee, J.-E., & Fung, I. (2008). "Amount effect" of water isotopes and quantitative analysis of post-condensation processes. *Hydrological Processes*, 22, 1–8. <https://doi.org/10.1002/hyp.6637>
- Lee, J.-E., Fung, I., DePaolo, D. J., & Henning, C. C. (2007). Analysis of the global distribution of water isotopes using the NCAR atmospheric general circulation model. *Journal of Geophysical Research*, 112(D16), D16306. <https://doi.org/10.1029/2006JD007657>
- Lee, J.-E., Fung, I., DePaolo, D. J., & Otto-Btiesner, B. (2008). Water isotopes during the Last Glacial Maximum: New general circulation model calculations. *Journal of Geophysical Research*, 113(D19), D19109. <https://doi.org/10.1029/2008JD009859>
- Lewis, S. C., LeGrande, A. N., Kelley, M., & Schmidt, G. A. (2013). Modeling insights into deuterium excess as an indicator of water vapor source conditions. *Journal of Geophysical Research: Atmospheres*, 118(2), 243–262. <https://doi.org/10.1029/2012JD017804>
- Li, S., Levin, N. E., & Chesson, L. A. (2015). Continental scale variation in ^{17}O -excess of meteoric waters in the United States. *Geochimica et Cosmochimica Acta*, 164, 110–126. <https://doi.org/10.1016/j.gca.2015.04.047>
- Libby, L. M., Pandolfi, L. J., Payton, P. H., Marshall, J., Becker, B., & Giertz-Sienbenlist, V. (1976). Isotopic tree thermometers. *Nature*, 261(5558), 284–288. <https://doi.org/10.1038/261284a0>
- Lowenthal, D., Hallar, A. G., McCubbin, I., David, R., Borys, R., Blossey, P., et al. (2016). Isotopic fractionation in wintertime orographic clouds. *Journal of Atmospheric and Oceanic Technology*, 33(12), 2663–2678. <https://doi.org/10.1175/JTECH-D-15-0233.1>
- Luz, B., & Barkan, E. (2010). Variations of $^{17}\text{O}/^{16}\text{O}$ and $^{18}\text{O}/^{16}\text{O}$ in meteoric waters. *Geochimica et Cosmochimica Acta*, 74(22), 6276–6286. <https://doi.org/10.1016/j.gca.2010.08.016>
- Luz, B., Barkan, E., Yam, R., & Shemesh, A. (2009). Fractionation of oxygen and hydrogen isotopes in evaporating water. *Geochimica et Cosmochimica Acta*, 73(22), 6697–6703. <https://doi.org/10.1016/j.gca.2009.08.008>
- Manabe, S., Smagorinsky, J., & Strickler, R. F. (1965). Simulated climatology of a general circulation model with a hydrologic cycle. *Monthly Weather Review*, 93(12), 769–798. [https://doi.org/10.1175/1520-0493\(1965\)093<0769:SCOAGC>2.3.CO;2](https://doi.org/10.1175/1520-0493(1965)093<0769:SCOAGC>2.3.CO;2)
- Martens, B., Miralles, D. G., Lievens, H., Fernández-Prieto, D., Beck, H. E., Dorigo, W. A., & Verhoest, N. E. C. (2017). GLEAM v3: Satellite-based land evaporation and root-zone soil moisture. *Geoscientific Model Development*, 10, 1903–1925. <https://doi.org/10.5194/gmd-10-1903-2017>
- Masson-Delmotte, V. (2005). GRIP deuterium excess reveals rapid and orbital-scale changes in Greenland moisture origin. *Science*, 309(5731), 118–121. <https://doi.org/10.1126/science.1108575>
- Masson-Delmotte, V., Hou, S., Ekaykin, A., Jouzel, J., Aristarain, A., Bernardo, R. T., et al. (2008). A review of Antarctic surface snow isotopic composition: Observations, atmospheric circulation, and isotopic modeling. *Journal of Climate*, 21(13), 3359–3387. <https://doi.org/10.1175/2007JCLI2139.1>
- McCarroll, D., & Loader, N. J. (2004). Stable isotopes in tree rings. *Quaternary Science Reviews*, 23(7–8), 771–801. <https://doi.org/10.1016/j.quascirev.2003.06.017>
- Merlivat, L. (1978). Molecular diffusivities of H_2^{16}O , HD^{16}O , and H_2^{18}O in gases. *The Journal of Chemical Physics*, 69(6), 2864. <https://doi.org/10.1063/1.436884>
- Merlivat, L., & Jouzel, J. (1979). Global climatic interpretation of the deuterium-oxygen 18 relationship for precipitation. *Journal of Geophysical Research*, 84(C8), 5029. <https://doi.org/10.1029/JC084iC08p05029>
- Met Office (2010). *Cartopy: A cartographic python library with a matplotlib interface*. Exeter, Devon. Retrieved from <https://scitools.org.uk/cartopy>
- Miller, M. F. (2002). Isotopic fractionation and the quantification of ^{17}O anomalies in the oxygen three-isotope system: An appraisal and geochemical significance. *Geochimica et Cosmochimica Acta*, 66(1), 1881–1889. [https://doi.org/10.1016/s0016-7037\(02\)00832-3](https://doi.org/10.1016/s0016-7037(02)00832-3)
- Moore, M., Kuang, Z., & Blossey, P. N. (2014). A moisture budget perspective of the amount effect. *Geophysical Research Letters*, 41(4), 1329–1335. <https://doi.org/10.1002/2013GL058302>
- Munksgaard, N. C., Kurita, N., Sánchez-Murillo, R., Ahmed, N., Araguas, L., Balachew, D. L., et al. (2019). Data descriptor: Daily observations of stable isotope ratios of rainfall in the tropics. *Scientific Reports*, 9(1), 14419. <https://doi.org/10.1038/s41598-019-50973-9>
- Nieto, R., Gimeno, L., & Trigo, R. M. (2006). A Lagrangian identification of major sources of Sahel moisture. *Geophysical Research Letters*, 33(18), L18707. <https://doi.org/10.1029/2006GL027232>
- Noone, D. (2008). The influence of midlatitude and tropical overturning circulation on the isotopic composition of atmospheric water vapor and Antarctic precipitation. *Journal of Geophysical Research*, 113(D4), D04102. <https://doi.org/10.1029/2007JD008892>

- Noone, D., Galewsky, J., Sharp, Z. D., Worden, J., Barnes, J., Baer, D., et al. (2011). Properties of air mass mixing and humidity in the subtropics from measurements of the D/H isotope ratio of water vapor at the Mauna Loa Observatory. *Journal of Geophysical Research*, 116(D22), D22113. <https://doi.org/10.1029/2011JD015773>
- Noone, D., & Simmonds, I. (2002). Associations between $\delta^{18}\text{O}$ of water and climate parameters in a simulation of atmospheric circulation for 1979–95. *Journal of Climate*, 15, 3150–3169. [https://doi.org/10.1175/1520-0442\(2002\)015<3150:aboowa>2.0.co;2](https://doi.org/10.1175/1520-0442(2002)015<3150:aboowa>2.0.co;2)
- Noone, D. C. (2012). Pairing measurements of the water vapor isotope ratio with humidity to deduce atmospheric moistening and dehydration in the tropical midtroposphere. *Journal of Climate*, 25(13), 4476–4494. <https://doi.org/10.1175/JCLI-D-11-0058.1>
- Nusbaumer, J., Alexander, P. M., LeGrande, A. N., & Tedesco, M. (2019). Spatial shift of Greenland moisture sources related to enhanced Arctic Warming. *Geophysical Research Letters*, 46(24), 14723–14731. <https://doi.org/10.1029/2019GL084633>
- Nusbaumer, J., & Noone, D. (2018). Numerical evaluation of the modern and future origins of atmospheric river moisture over the west coast of the United States. *Journal of Geophysical Research: Atmospheres*, 123(12), 6423–6442. <https://doi.org/10.1029/2017JD028081>
- Nusbaumer, J., Wong, T. E., Bardeen, C., & Noone, D. (2017). Evaluating hydrological processes in the Community Atmosphere Model Version 5 (CAM5) using stable isotope ratios of water. *Journal of Advances in Modeling Earth Systems*, 9(2), 949–977. <https://doi.org/10.1029/2016MS000839>
- Parkes, S. D., McCabe, M. F., Griffiths, A. D., Wang, L., Chambers, S., Ershadi, A., et al. (2017). Response of water vapour D-excess to land-atmosphere interactions in a semi-arid environment. *Hydrology and Earth System Sciences*, 21, 533–548. <https://doi.org/10.5194/hess-21-533-2017>
- Pauluis, O. (2011). Water vapor and mechanical work: A comparison of Carnot and steam cycles. *Journal of the Atmospheric Sciences*, 68(1), 91–102. <https://doi.org/10.1175/2010JAS3530.1>
- Pauluis, O., Czaja, A., & Korty, R. (2008). The global atmospheric circulation on moist isentropes. *Science*, 321(5892), 1075–1078. <https://doi.org/10.1126/science.1159649>
- Pfahl, S., & Sodenmann, H. (2014). What controls deuterium excess in global precipitation? *Climate of the Past*, 10(2), 771–781. <https://doi.org/10.5194/cp-10-771-2014>
- Pfahl, S., & Wernli, H. (2008). Air parcel trajectory analysis of stable isotopes in water vapor in the eastern Mediterranean. *Journal of Geophysical Research*, 113(D20), D20104. <https://doi.org/10.1029/2008JD009839>
- Poulsen, C. J., & Jeffery, M. L. (2011). Climate change imprinting on stable isotopic compositions of high-elevation meteoric water cloaks past surface elevations of major orogens. *Geology*, 39(6), 595–598. <https://doi.org/10.1130/G32052.1>
- Putman, A. L., & Bowen, G. J. (2019). Technical note: A global database of the stable isotopic ratios of meteoric and terrestrial waters. *Hydrology and Earth System Sciences*, 23(10), 4389–4396. <https://doi.org/10.5194/hess-23-4389-2019>
- Putman, A. L., Bowen, G. J., & Strong, C. (2021). Local and regional modes of hydroclimatic change expressed in modern multidecadal precipitation oxygen isotope trends. *Geophysical Research Letters*, 48, e2020GL092006. <https://doi.org/10.1029/2020GL092006>
- Putman, A. L., Feng, X., Sonder, L. J., & Posmentier, E. S. (2017). Annual variation in event-scale precipitation $\delta^2\text{H}$ at Barrow, AK, reflects vapor source region. *Atmospheric Chemistry and Physics*, 17(7), 4627–4639. <https://doi.org/10.5194/acp-17-4627-2017>
- Putman, A. L., Fiorella, R. P., Bowen, G. J., & Cai, Z. (2019). A global perspective on local meteoric water lines: Meta-analytic insight into fundamental controls and practical constraints. *Water Resources Research*, 55(8), 6896–6910. <https://doi.org/10.1029/2019WR025181>
- Quade, M., Brüggemann, N., Graf, A., Vanderborght, J., Vereecken, H., & Rothfuss, Y. (2018). Investigation of Kinetic isotopic fractionation of water during bare soil evaporation. *Water Resources Research*, 54, 6909–6928. <https://doi.org/10.1029/2018WR023159>
- Raval, A., & Ramanathan, V. (1989). Observational determination of the greenhouse effect. *Nature*, 342, 758–761. <https://doi.org/10.1038/342758a0>
- R Core Team (2021). *R: A language and environment for statistical computing*. Vienna, Austria: R Foundation for Statistical Computing. Retrieved from <https://www.R-project.org>
- Rindsberger, M., Magaritz, M., Carmi, I., & Gilad, D. (1983). The relation between air mass trajectories and the water isotope composition of rain in the Mediterranean Sea area. *Geophysical Research Letters*, 10(1), 43–46. <https://doi.org/10.1029/GL010i001p00043>
- Risi, C., Bony, S., & Vimeux, F. (2008). Influence of convective processes on the isotopic composition ($\delta^{18}\text{O}$ and δD) of precipitation and water vapor in the tropics: 2. Physical interpretation of the amount effect. *Journal of Geophysical Research*, 113(D19), D19306. <https://doi.org/10.1029/2008JD009943>
- Risi, C., Bony, S., Vimeux, F., & Jouzel, J. (2010). Water-stable isotopes in the LMDZ4 general circulation model: Model evaluation for present-day and past climates and applications to climatic interpretations of tropical isotopic records. *Journal of Geophysical Research*, 115(D12), D12118. <https://doi.org/10.1029/2009JD013255>
- Risi, C., Muller, C., & Blossey, P. (2021). Rain evaporation, snow melt and entrainment at the heart of water vapor isotopic variations in the tropical troposphere, according to large-eddy simulations and a two-column model. *Journal of Advances in Modeling Earth Systems*, 13, e2020MS002381. <https://doi.org/10.1029/2020MS002381>
- Risi, C., Noone, D., Frankenberg, C., & Worden, J. (2013). Role of continental recycling in intraseasonal variations of continental moisture as deduced from model simulations and water vapor isotopic measurements: Continental recycling and water isotopes. *Water Resources Research*, 49(7), 4136–4156. <https://doi.org/10.1029/wrcr.20312>
- Risi, C., Ogee, J., Bony, S., Barriac, T., Raz Yaseef, N., Wingate, L., et al. (2016). The water isotopic version of the land-surface model ORCHIDEE: Implementation, evaluation, sensitivity to hydrological parameters. *Hydrology: Current Research*, 07(4). <https://doi.org/10.4172/2157-7587.1000258>
- Rowley, D. B., & Garzione, C. N. (2007). Stable isotope-based paleoaltimetry. *Annual Review of Earth and Planetary Sciences*, 35(1), 463–508. <https://doi.org/10.1146/annurev.earth.35.031306.140155>
- Rozanski, K., Araguás-Araguás, L., & Gonfiantini, R. (1993). Isotopic patterns in modern global precipitation. In P. K. Swart, K. C. Lohmann, J. Mckenzie, & S. Savin (Eds.), *Geophysical monograph series* (pp. 1–36). Washington, D. C: American Geophysical Union. <https://doi.org/10.1029/GM078p0001>
- Salati, E., Dall'Olio, A., Matsui, E., & Gat, J. R. (1979). Recycling of water in the Amazon Basin: An isotopic study. *Water Resources Research*, 15(5), 1250–1258. <https://doi.org/10.1029/WR015i005p01250>
- Samuels-Crow, K. E., Galewsky, J., Hardy, D. R., Sharp, Z. D., Worden, J., & Braun, C. (2014). Upwind convective influences on the isotopic composition of atmospheric water vapor over the tropical Andes. *Journal of Geophysical Research: Atmospheres*, 119(12), 7051–7063. <https://doi.org/10.1002/2014JD021487>
- Schmidt, G. A., LeGrande, A. N., & Hoffmann, G. (2007). Water isotope expressions of intrinsic and forced variability in a coupled ocean-atmosphere model. *Journal of Geophysical Research*, 112(D10), D10103. <https://doi.org/10.1029/2006JD007781>
- Sellers, P. J., Dickinson, R. E., Randall, D., Betts, A. K., Hall, F. G., Berry, J. A., et al. (1997). Modeling the exchanges of energy, water, and carbon between continents and the atmosphere. *Science*, 275(5299), 502–509. <https://doi.org/10.1126/science.275.5299.502>

- Shi, X., Liu, X., & Zhang, K. (2015). Effects of pre-existing ice crystals on cirrus clouds and comparison between different ice nucleation parameterizations with the Community Atmosphere Model (CAM5). *Atmospheric Chemistry and Physics*, 15(3), 1503–1520. <https://doi.org/10.5194/acp-15-1503-2015>
- Siegenthaler, U., & Oeschger, H. (1980). Correlation of ^{18}O in precipitation with temperature and altitude. *Nature*, 285(5763), 314–317. <https://doi.org/10.1038/285314a0>
- Siler, N., Bailey, A., Roe, G. H., Buzert, C., Markle, B., & Noone, D. (2021). The large-scale, long-term coupling of temperature, hydrology, and water isotopes. *Journal of Climate*, 1–51. <https://doi.org/10.1175/JCLI-D-20-0563.1>
- Siler, N., Roe, G. H., & Armour, K. C. (2018). Insights into the Zonal-Mean Response of the Hydrologic Cycle to Global Warming from a Diffusive Energy Balance Model. *Journal of Climate*, 31(18), 7481–7493. <https://doi.org/10.1175/JCLI-D-18-0081.1>
- Siler, N., Roe, G. H., Armour, K. C., & Feldl, N. (2019). Revisiting the surface-energy-flux perspective on the sensitivity of global precipitation to climate change. *Climate Dynamics*, 52(7–8), 3983–3995. <https://doi.org/10.1007/s00382-018-4359-0>
- Singh, H. K. A., Bitz, C. M., Donohoe, A., Nusbaumer, J., & Noone, D. C. (2016). A mathematical framework for analysis of water tracers. Part II: Understanding large-scale perturbations in the hydrological cycle due to CO_2 doubling. *Journal of Climate*, 29(18), 6765–6782. <https://doi.org/10.1175/JCLI-D-16-0293.1>
- Singh, H. K. A., Bitz, C. M., Nusbaumer, J., & Noone, D. C. (2016). A mathematical framework for analysis of water tracers: Part 1: Development of theory and application to the preindustrial mean state. *Journal of Advances in Modeling Earth Systems*, 8(2), 991–1013. <https://doi.org/10.1002/2016MS000649>
- Sodemann, H., Schwierz, C., & Wernli, H. (2008). Interannual variability of Greenland winter precipitation sources: Lagrangian moisture diagnostic and North Atlantic Oscillation influence. *Journal of Geophysical Research*, 113(D3), D03107. <https://doi.org/10.1029/2007JD008503>
- Sodemann, H., & Stohl, A. (2009). Asymmetries in the moisture origin of Antarctic precipitation. *Geophysical Research Letters*, 36(22), L22803. <https://doi.org/10.1029/2009GL040242>
- Stewart, M. K. (1975). Stable isotope fractionation due to evaporation and isotopic exchange of falling waterdrops: Applications to atmospheric processes and evaporation of lakes. *Journal of Geophysical Research*, 80(9), 1133–1146. <https://doi.org/10.1029/JC080i009p01133>
- Tian, L., Masson-Delmotte, V., Stievenard, M., Yao, T., & Jouzel, J. (2001). Tibetan Plateau summer monsoon northward extent revealed by measurements of water stable isotopes. *Journal of Geophysical Research*, 106(D22), 28081–28088. <https://doi.org/10.1029/2001JD900186>
- Trenberth, K. E. (1998). Atmospheric moisture residence times and cycling: Implications for rainfall rates and climate change. *Climatic Change*, 39, 667–694. <https://doi.org/10.1023/a:1005319109110>
- Trenberth, K. E., Fasullo, J. T., & Kiehl, J. (2009). Earth's global energy budget. *Bulletin of the American Meteorological Society*, 90(3), 311–324. <https://doi.org/10.1175/2008BAMS2634.1>
- Treydte, K. S., Schleser, G. H., Helle, G., Frank, D. C., Winiger, M., Haug, G. H., & Esper, J. (2006). The twentieth century was the wettest period in northern Pakistan over the past millennium. *Nature*, 440(7088), 1179–1182. <https://doi.org/10.1038/nature04743>
- Uemura, R., Matsui, Y., Yoshimura, K., Motoyama, H., & Yoshida, N. (2008). Evidence of deuterium excess in water vapor as an indicator of ocean surface conditions. *Journal of Geophysical Research*, 113(D19), D19114. <https://doi.org/10.1029/2008JD010209>
- Vachon, R. W., Welker, J. M., White, J. W. C., & Vaughn, B. H. (2010). Monthly precipitation isoscapes ($\delta^{18}\text{O}$) of the United States: Connections with surface temperatures, moisture source conditions, and air mass trajectories. *Journal of Geophysical Research*, 115(D21), D21126. <https://doi.org/10.1029/2010JD014105>
- van der Ent, R. J., & Savenije, H. H. G. (2011). Length and time scales of atmospheric moisture recycling. *Atmospheric Chemistry and Physics*, 11(5), 1853–1863. <https://doi.org/10.5194/acp-11-1853-2011>
- van der Ent, R. J., & Tuinenburg, O. A. (2017). The residence time of water in the atmosphere revisited. *Hydrology and Earth System Sciences*, 21(2), 779–790. <https://doi.org/10.5194/hess-21-779-2017>
- Vimeux, F., Gallaire, R., Bony, S., Hoffmann, G., & Chiang, J. (2005). What are the climate controls on δD in precipitation in the Zongo Valley (Bolivia)? Implications for the Illimani ice core interpretation. *Earth and Planetary Science Letters*, 240(2), 205–220. <https://doi.org/10.1016/j.epsl.2005.09.031>
- Vimeux, F., Ginot, P., Schwikowski, M., Vuille, M., Hoffmann, G., Thompson, L. G., & Schotterer, U. (2009). Climate variability during the last 1000 years inferred from Andean ice cores: A review of methodology and recent results. *Paleogeography, Paleoclimatology, Palaeoecology*, 281(3–4), 229–241. <https://doi.org/10.1016/j.palaeo.2008.03.054>
- Vimeux, F., Masson, V., Jouzel, J., Stievenard, M., & Petit, J. R. (1999). Glacial-interglacial changes in ocean surface conditions in the Southern Hemisphere. *Nature*, 398(6726), 410–413. <https://doi.org/10.1038/18860>
- Vimeux, F., Tremoy, G., Risi, C., & Gallaire, R. (2011). A strong control of the South American SeeSaw on the intra-seasonal variability of the isotopic composition of precipitation in the Bolivian Andes. *Earth and Planetary Science Letters*, 307(1–2), 47–58. <https://doi.org/10.1016/j.epsl.2011.04.031>
- Vuille, M., Bradley, R. S., Healy, R., Werner, M., Hardy, D. R., Thompson, L. G., & Keimig, F. T. (2003). Modeling $\delta^{18}\text{O}$ in precipitation over the tropical Americas: 2. Simulation of the stable isotope signal in Andean ice cores. *Journal of Geophysical Research*, 108(D6), 4175. <https://doi.org/10.1029/2001JD002039>
- Wang, Y., Liu, X., Hoose, C., & Wang, B. (2014). Different contact angle distributions for heterogeneous ice nucleation in the Community Atmospheric Model version 5. *Atmospheric Chemistry and Physics*, 14(19), 10411–10430. <https://doi.org/10.5194/acp-14-10411-2014>
- Wang-Erlansson, L., van der Ent, R. J., Gordon, L. J., & Savenije, H. H. G. (2014). Contrasting roles of interception and transpiration in the hydrological cycle – Part 1: Temporal characteristics over land. *Earth System Dynamics*, 5(2), 441–469. <https://doi.org/10.5194/esd-5-441-2014>
- Wei, Z., Yoshimura, K., Wang, L., Miralles, D. G., Jasechko, S., & Lee, X. (2017). Revisiting the contribution of transpiration to global terrestrial evapotranspiration: Revisiting Global ET Partitioning. *Geophysical Research Letters*, 44(6), 2792–2801. <https://doi.org/10.1002/2016GL072235>
- Welp, L. R., Lee, X., Griffis, T. J., Wen, X.-F., Xiao, W., Li, S., et al. (2012). A meta-analysis of water vapor deuterium-excess in the midlatitude atmospheric surface layer. *Global Biogeochemical Cycles*, 26(3), GB3021. <https://doi.org/10.1029/2011GB004246>
- Wheeler, L. B., Galewsky, J., Herold, N., & Huber, M. (2016). Late Cenozoic surface uplift of the southern Sierra Nevada (California, USA): A paleoclimate perspective on lee-side stable isotope paleoaltimetry. *Geology*, 44(6), 451–454. <https://doi.org/10.1130/G37718.1>
- Winschall, A., Pfahl, S., Sodemann, H., & Wernli, H. (2014). Comparison of Eulerian and Lagrangian moisture source diagnostics – The flood event in eastern Europe in May 2010. *Atmospheric Chemistry and Physics*, 14(13), 6605–6619. <https://doi.org/10.5194/acp-14-6605-2014>
- Wong, T. E., Nusbaumer, J., & Noone, D. C. (2017). Evaluation of modeled land-atmosphere exchanges with a comprehensive water isotope fractionation scheme in version 4 of the Community Land Model. *Journal of Advances in Modeling Earth Systems*, 9(2), 978–1001. <https://doi.org/10.1002/2016MS000842>

- Wright, M. N., & Ziegler, A. (2017). ranger: A fast implementation of random forests for high dimensional data in C++ and R. *Journal of Statistical Software*, 77(1). <https://doi.org/10.18637/jss.v077.i01>
- Yamanaka, T., Tsujimura, M., Oyunbaatar, D., & Davaa, G. (2007). Isotopic variation of precipitation over eastern Mongolia and its implication for the atmospheric water cycle. *Journal of Hydrology*, 333(1), 21–34. <https://doi.org/10.1016/j.jhydrol.2006.07.022>
- Yao, T., Masson-Delmotte, V., Gao, J., Yu, W., Yang, X., Risi, C., et al. (2013). A review of climatic controls on $\delta^{18}\text{O}$ in precipitation over the Tibetan Plateau: Observations and simulations. *Reviews of Geophysics*, 51(4), 525–548. <https://doi.org/10.1002/rog.20023>
- Yoshimura, K., Kanamitsu, M., Noone, D., & Oki, T. (2008). Historical isotope simulation using reanalysis atmospheric data. *Journal of Geophysical Research*, 113(D19), D19108. <https://doi.org/10.1029/2008JD010074>
- Yoshimura, K., Miyazaki, S., Kanae, S., & Oki, T. (2006). Iso-MATSIRO, a land surface model that incorporates stable water isotopes. *Global and Planetary Change*, 51(1–2), 90–107. <https://doi.org/10.1016/j.gloplacha.2005.12.007>
- Zhang, G. J., & McFarlane, N. A. (1995). Sensitivity of climate simulations to the parameterization of cumulus convection in the Canadian climate centre general circulation model. *Atmosphere-Ocean*, 33(3), 407–446. <https://doi.org/10.1080/07055900.1995.9649539>
- Zimmermann, U., Ehhalt, D., & Münnich, K. O. (1967). Soil-water movement and evapotranspiration: Changes in the isotopic composition of the water. In *Symposium on isotopes in hydrology*. Vienna, Austria: International Atomic Energy Agency (IAEA).
- Zwart, C., Munksgaard, N. C., Protat, A., Kurita, N., Lambrinidis, D., & Bird, M. I. (2018). The isotopic signature of monsoon conditions, cloud modes, and rainfall type. *Hydrological Processes*, 32(15), 2296–2303. <https://doi.org/10.1002/hyp.13140>